Università degli Studi di Catania
Scuola Superiore di Catania

International PhD in

Nuclear and Particle Astrophysics

XXVI cycle

# The modifications of Mercury surface induced by solar wind ions

Ivana Sangiorgio

Coordinator of PhD
Prof. Stefano Romano

Tutor
Prof. Francesca Zuccarello
Co-Tutor
Dr. Maria Elisabetta Palumbo

*Di terra i profumi, lui, tutti inspirò,*
*posate e canzuni, in gran chiasso, accordò.*
*Dei pesci i costumi, in silenzio, spiò,*
*con ganci e buttùni ogni legge sfidò.*
*La "Banca" in volumi,*
*il greco e i Maccarrùni,*
*'u iàttu e i "pirsùni",*
*mugghieri e vasùni...*
*... Giostra allegra di fiabe lì, per te, s'inventò*
*e cullarti coi lumi e L'Amore ora può.*

*Alla mia famiglia*

Printed in Catania, December 10th 2013

# INDEX

Introduction 1

Chapter 1
What we know about the planet Mercury 5
1.1 Mercury and space weathering 5
1.2 Missions addressed to Mercury 8
1.2.1 Mariner 10 8
1.2.2 MESSENGER 10
1.2.3 BepiColombo 15
1.3 Terrestrial planets: Mercury 19
1.4 Magmatic rocks and minerals 21
1.5 Mercury and the Moon 24
1.5.1 Lunar soil modifications 24
1.5.2 Similarity with the Moon? 27
1.6 Experiments and modeling in literature 30
1.6.1 Reflectance spectra and compositional heterogeneity 30
1.6.2 Exosphere-surface relationship 32
1.7 Outline: which are, then, Mercury's surface building blocks 36

Chapter 2
Experimental techniques 39
2.1 Experimental analytical techniques:
Laboratory for Experimental Astrophysics (LASp) 39
2.2.1 The analysis chamber 42

2.2.2 The spectrophotometers 43
Section A: IR spectrophotometer and data 43
Section B: UV-Vis NIR spectrophotometer and data 48
2.2.3 The ion implanter 53
2.3 Materials and experimental procedure 56
2.3.1 Etnean samples 56
2.3.2 Other silicate materials 61

Chapter 3
Laboratory spectra of Mercury analog materials 63
3.1 UV-Vis-NIR reflectance spectra of Etnean basalts 63
3.2 IR reflectance spectra of Etnean basalts 70
3.3 Irradiated etnean samples 74
3.4 Other silicate spectra 79
3.4.1 Silicate films on silicon wafers 79
3.4.2 Silicate rocks spectra 82

Chapter 4
Observations and comparison with laboratory spectra 85
4.1 Mercury spectra 85
4.2 Sulfides 94
4.3 Comparison between observational and laboratory spectra 97
4.4 Discussion 105

Bibliography 109

Acknowledgements 113

# INTRODUCTION

The space through which Solar System bodies move is not empty. The *Interplanetary Medium* fills it with dust, photons, meteorites of different size, cosmic rays and a mixture of electrons, protons, heavier ions and magnetic fields, the *solar wind,* streaming radially outward in all the directions from the Sun at supersonic speeds of hundreds of kilometers per second.

How the Interplanetary Medium interacts with planets depends on whether they have magnetic fields or not.

Airless bodies, such as Mercury, are continuously exposed to the above mentioned bombardments that can induce on their surfaces sputtering, implantation, photo or thermal desorption, vaporization, erosion. These processes which alter physical and optical properties of the surfaces and contribute to the mass loss of the bodies, constitute the so called *space weathering*.

Mercury is the innermost Solar System planet, with the highest orbital eccentricity (e=0.205) and complete three rotations around its axis for every two revolutions around its orbit. These peculiarities give to Mercury a great thermal excursion (~700 K) between Sun-exposed and the "dark" sides and make this planet a very interesting subject for the astrophysical community because information regarding its principal constituents is not complete.

Despite its position in the Solar System, some ground observations of Mercury, in the visible, near and mid infrared spectral region (0.5-25 μm), have been made and have revealed, with a few uncertainties, a heterogeneous mineralogical surface composition and the presence of sodium, potassium and calcium.

The greatest contribution to the knowledge of the planet has been obtained thanks to space missions because they have acquired, and are still acquiring, an huge quantity of resolved images and data. The future joint European-Japanese space mission, BepiColombo, will add complementary information and new laboratory experiments are also requested for testing its instruments, prepare and validate the results.

The work in this thesis arises from a scientific collaboration between Osservatorio Astrofisico di Catania of INAF (Istituto Nazionale di Astrofisica), and IAPS-INAF (Istituto di Astrofisica e Planetologia Spaziali) in Rome, in which operate the Principal Investigators of two experiments (ISA, Italian Spring Accelerometer and SERENA, Search for Exospheric Refilling and Emitted Natural Abundances) of the BepiColombo mission. The aim of the present work is to characterize some Mercury analog materials in preparation to ELENA (Emitted Low-Energy Neutral Atoms) experiments aboard BepiColombo.

The candidate materials, here chosen on the basis of existing data in literature, are old and fresh erupted etnean basalts, together with other silicate rocks (sodalite, nepheline, jadeite) containing sodium and potassium.

The variations in the spectral reflectance of these candidate Mercury materials, before and after irradiation with energetic ions (200 keV $H^+$ and $Ar^+$) aimed at simulate cosmic ion bombardment, have been studied, with the intent to be compared with observational Mercury spectra.

Some possible analogies have been tested operating an opportune scaling of the laboratory ion energy and fluences, in order to estimate the correspondent exposure time scale at Mercury.

Our Mercury analog materials seem to be the best candidates so far found, even if a wider study on different materials is needed.

Furthermore the changes in the spectral reflectance of irradiated laboratory samples confirm that space weathering on Mercury surface produces relevant spectral variations of the surface reflectance.

This work starts from Chapter 1 with a description of the state of the art of Mercury (obtained thanks to space missions *Mariner 10* and *MESSENGER* and thanks to some experiments and modeling), a presentation of the future mission BepiColombo, and a definition of terrestrial planets and magmatic rocks.

In Chapter 2 the detailed experimental instrumentations, the working procedures concerning the sample preparation and their characteristics are presented, while the UV-Vis-NIR and IR reflectance spectra before and after irradiations of the Mercury analog laboratory samples are reported in Chapter 3.

Chapter 4, the conclusive, is dedicated to the presentation of Mercury spectra so far obtained from ground and MESSENGER satellite in the 400-1000 nm spectral region. In this chapter we present and discuss the comparison between observational and reflectance spectra of our laboratory sample.

# CHAPTER 1

# WHAT WE KNOW ABOUT THE PLANET MERCURY

Mercury was named after the Roman god Mercury (who was regarded to be the speedy messenger between the gods) because the planet seemed to move so quickly in the sky.
It slips away to a full comprehension yet, due to the extreme conditions to which Mercury's environment is exposed and some of its peculiarities and anomalies, however, make this planet a subject of special scientific interest.
In this chapter we will try to trace the main features on the basis of existing data in the literature.

## 1.1 Mercury and space weathering

The surface of the airless bodies in the Solar System is endlessly struck by several energetic processes. Cosmic ions, solar wind and coronal mass ejections, photons, micrometeorite impacts can induce sputtering, implantation, photo or thermal desorption, vaporization,

cause the erosion of the surfaces. These processes, which alter physical and optical properties of the surfaces and contribute to the mass loss of the bodies, constitute the so called *space weathering* (Baratta et al., 2011).

Spacecraft observations permit to assert that Mercury's crust was shaped by volcanism, deformation and impact cratering and the presence of albedo and color variations is related to compositional heterogeneities (Denevi et al., 2009).

The most important findings are summarized in Table 1.1 and will be described below.

Mercury's middle orbit is 0.387 AU (1 AU, Astronomical Unit = average Earth-Sun distance=$1.496\times10^{11}$ m), with an orbital period of about 88 terrestrial days, and a rotation period of 59 terrestrial days. These orbital characteristics, together with a very high eccentricity (e=0.205), gives to Mercury an extremely variable temperature, ranging from 770 K at the perihelion on the Sun exposed surface, to 90 K at the aphelion, in the "dark" side.

*Table 1.1- Mercury's parameters (Milillo et al., 2005).*

| **Mercury ☿** | |
|---|---|
| Radius | 2240 km (0.38 $R_{Earth}$) |
| Mass | $3.3022\times10^{23}$ kg (0.055 Earth mass) |
| Aphelion | 69816900 km (0.466 697 AU) |
| Perihelion | 46001200 km (0.307 499 AU) |
| Gravity acceleration | 0.377 g |
| Eccentricity | 0.205 |
| Mercurian day | ~ 59 Earth days |
| Mercurian year | ~ 88 Earth days |
| Mean density | ~ 5.43 g·cm$^{-3}$ (~ 0.98 Earth density) |
| Uncompressed density | ~ 5.3 g·cm$^{-3}$ |
| Temperature range | 770 K (perihelion day side) 90 K (aphelion night side) |

Because of its vicinity to the Sun, its relatively small dimensions and its gravity, Mercury is not able to maintain a proper atmosphere, but only a tenuous gaseous envelope in which molecules cannot collide (the *exosphere)*.

This region, together with the surface, is continuously modified by many processes, as described below.

Thanks to Mariner 10, the first space mission to Mercury, we knew about the existence of an internal magnetic field, not yet well established, but able to reject a great part of the solar wind ions. Solar wind ions are composed of 95% protons, about 5% of α-particles and traces of heavier nuclei. Nevertheless, in the regions of the magnetic reconnection between Mercury magnetic field lines and those of the interplanetary magnetic field (cusps), ions can penetrate, impact the surface and can create neutral and also ionized particle emission (sputtering). A part of the ions penetrated is diffused and circulate around the closed line of the magnetic field, or falls down in the surface, according to the mass, in the middle latitudes; another part of these ions exchange the charge with the thermal atoms emitted in the exosphere, producing Energetic Neutral Atoms (ENA).

In addition to sputtering, particles can be removed from the surface by photon stimulated desorption (PSD), the micrometeorite impact vaporization (MIV) and the thermal desorption (TD) of light atoms (H, He).

The kinetic energy of the released particles depends on the process involved and is below a few eVs for photon-stimulated desorption (PSD) and thermal evaporation, a few eVs for micrometeoroid impacts, and can reach higher values (few tens of eV) for ion sputtering (Milillo et al., 2005).

The Sputtered High Energy Atoms (SHEA), the Energetic Neutral Atoms (ENA), together with the accelerated ions can escape the planet attraction and contribute to the mass loss of the surface and to the erosion of the exosphere.

Mercury surface, its exosphere and magnetosphere, under the influence of the solar wind and the interplanetary field, are then a strongly coupled dynamic system mostly ruled by the interactions between the neutral/ionized gas particles with the surface and the magnetospheric plasma.

As previously mentioned, the major contribution to the knowledge of the planet Mercury has been given by space missions. In the next section these will be presented in detail.

# 1.2 Missions addressed to Mercury

Because of its position in the Solar System, it has been difficult to observe Mercury from Earth.
Space missions have rebuilt the knowledge of the planet Mercury because they have allowed to acquire resolved images and data in a wide range of the electromagnetic spectrum.
The missions addressed to Mercury are the past Mariner 10, the still actual MESSENGER, and the future BepiColombo.

## 1.2.1 Mariner 10

Mariner 10 was an American robotic space probe launched by NASA on November 3, 1973, to fly by the planets Mercury and Venus.
It was the first spacecraft to visit Mercury and to use the gravitational pull of one planet (Venus) to reach another (Mercury), and the first spacecraft mission to visit two planets.
Was Michael Minovitch, a university student who worked in the summer at the Jet Propulsion Laboratory of NASA, who in 1963 developed the concept of gravitational propulsion. He thought of using the slingshot effect with propulsive purposes in a systematic way, resulting in a net reduction of propellant required for missions addressed to several planets.
In 1970, Giuseppe Colombo (known also as Bepi Colombo), Professor of Applied Mechanics at the Faculty of Engineering of Padua, proposed an important modification to the Mariner 10 path. Colombo found that the orbital period of the probe after the fly-by of Mercury would have coincided with twice the period of revolution of the planet itself and suggested to use such resonance to program multiple flybys of Mercury.
Thanks to these important contributes, the spacecraft was able to fly by Mercury three times in a retrograde heliocentric orbit, using the solar radiation pressure on its solar panels and its high-gain antenna as means of attitude control during flight, and returned the first-ever close-up images of Venus and Mercury and data on the planets.
The probe was launched onboard a carrier Atlas/Centaur, at Cape Canaveral Air Force Station, Florida.

Mariner 10 instruments (shown in Fig. 1.1, on the left panel) included: twin telescope/cameras, with digital tape recorder, which took images alternately, every 42 seconds, and sent them directly to Earth; an ultraviolet occultation spectrometer, designed for the detection of a possible atmosphere of Mercury which was operating only during the flybys of the planet; an ultraviolet airglow spectrometer, for the detection of the radiation emitted by the atmosphere; an infrared radiometer, which measured the extent of the thermal radiation emitted by the upper layers of the clouds of Venus and from the surface of Mercury at the wavelengths of 11 and 45 micrometers; two magnetometers, in order to distinguish the magnetic disturbance generated by the sensor itself from the magnetic field of the interplanetary plasma; two charged particle telescopes, sensitive to charged particles (protons, α-particles, electrons) and operating at different energy intervals; a scanning electrostatic analyzer and a scanning electron spectrometer to analyze the distribution of the solar wind in interplanetary space and assess their interaction with Venus and Mercury.

The probe carried also a motor driven high-gain dish antenna and a low-gain omnidirectional antenna.

Instruments on-board the spacecraft measured the atmospheric, surface, and physical characteristics of Mercury and Venus. Experiments included television photography, magnetic field, plasma, infrared radiometry, ultraviolet spectroscopy, and radio science detectors. However, some technical problems allowed to operate only a part of these experiments.

An experimental X-band, high-frequency transmitter was flown for the first time on this spacecraft.

The spacecraft passed Venus on February 5, 1974 and crossed the orbit of Mercury on 29 March 1974, at a distance of about 704 km from the surface. A second encounter with Mercury, when more photographs were taken, occurred on 21 September 1974, at an altitude of 48069 km. A third and last Mercury encounter at an altitude of 327 km, with additional photography of about 300 frames and magnetic field measurements occurred on 16 March 1975. Engineering tests were continued until 24 March 1975, when the supply of attitude-control gas was depleted and the mission was terminated.

Owing to the geometry of its orbit – its orbital period was almost exactly twice Mercury's – the same side of Mercury was sunlit each time, so it was only able to map 40–45% of

Mercury's surface, taking over 2800 photos (a mosaic of a part is represented in Fig. 1.1, on the right panel).

It was confirmed that Mercury has a tenuous atmosphere consisting primarily of helium and a cratered, dormant Moon-like surface was shown in the images. Mercury was shown to have a small magnetic field and a relatively large iron-rich core.

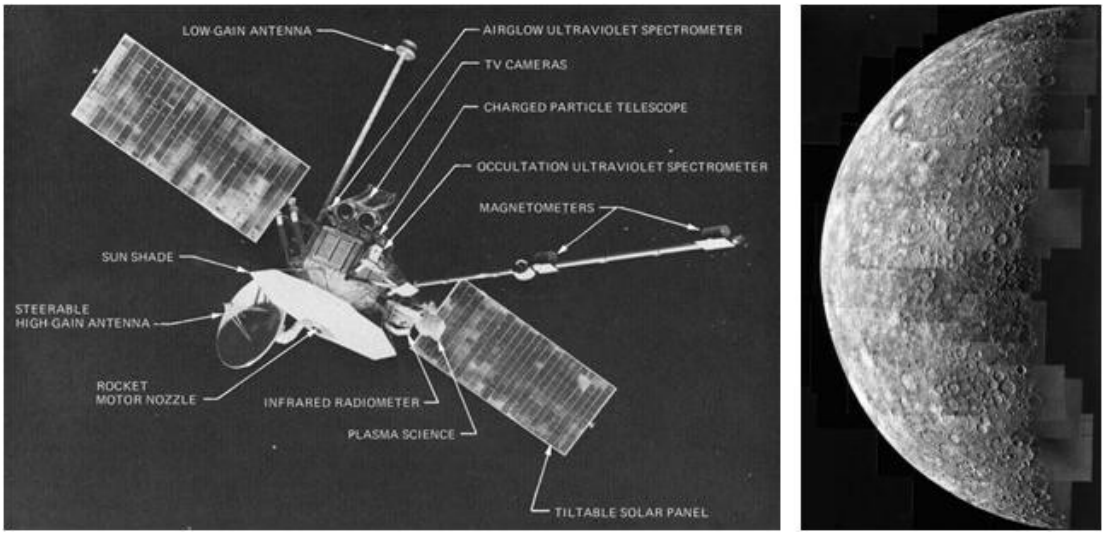


*Fig. 1.1 – Left panel: an image of the Mariner 10 spacecraft with its instrumentations. Right panel: a mosaic photo taken by the Mariner 10 spacecraft during its first approach to Mercury. The mosaic consists of 18 images taken at 42 s intervals during a 13 minute period when the spacecraft was 200000 km from the planet.*

## 1.2.2 MESSENGER

MESSENGER (MErcury Surface, Space ENvironment, GEochemistry, and Ranging) is a robotic NASA spacecraft orbiting the planet Mercury, the first spacecraft ever to do so.

It was launched aboard a Delta II rocket in August 2004 to study Mercury's chemical composition, geology, and magnetic field. It made a first flyby in January 2008, followed by a second flyby in October 2008, and a third flyby in September 2009.

The spacecraft flew by Earth once, Venus twice, and Mercury itself three times, allowing it to decelerate relative to Mercury using minimal fuel. MESSENGER successfully entered Mercury's orbit on March 18, 2011.

MESSENGER's dual-mode, liquid chemical propulsion system is integrated into the spacecraft's structure to make economical use of mass. The structure is primarily composed of a graphite epoxy (resins) material, which provides the strength necessary to survive launch while offering lower mass. Two large solar panels, supplemented with a nickel-hydrogen battery, provide MESSENGER's power.

The spacecraft was designed and built at the Johns Hopkins University Applied Physics Laboratory. Science operations, managed by Dr. Sean Solomon as principal investigator, and mission operations are also conducted at JHU/APL.

On March 17, 2012, having collected close to 100000 images, MESSENGER ended its one-year primary mission and entered an extended mission scheduled to last until March 2013. Now MESSENGER is exhausting its fuel and gradually reducing its orbit, until it will impact the planet. A picture showing the MESSENGER satellite current position is shown in Fig. 1.2.

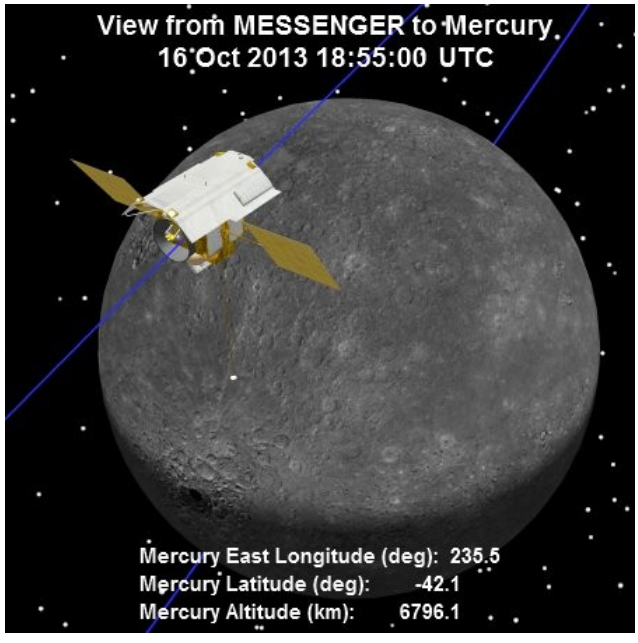


*Fig. 1.2– An image showing the surface of Mercury as seen from MESSENGER's current position as well as the MESSENGER spacecraft's current orbit and orientation. Positions of stars with magnitude 5 or brighter are shown. The depiction of Mercury's surface includes images acquired by the Mariner 10 and MESSENGER spacecraft.*

The mission's primary science objectives included: determining the surface composition of Mercury, characterizing the geological history of the planet, determining the precise strength of the magnetic field and its variation with position and altitude, investigating the presence of a liquid outer core by measuring Mercury's libration, determining the nature of the radar reflective materials at Mercury's poles, investigating the important volatile species and their sources and sinks on and near Mercury.

To reach these objectives, MESSENGER was supplied with several instruments aboard (listed in Table1.2 and indicated in Fig. 1.3, left panel): a Mercury Dual Imaging System (MDIS), a Gamma-Ray and Neutron Spectrometer (GRNS), a X-Ray Spectrometer (XRS), a Magnetometer (MAG), a Mercury Laser Altimeter (MLA), a Mercury Atmospheric and Surface Composition Spectrometer (MASCS), an Energetic Particle and Plasma Spectrometer (EPPS), Radio Science (RS).

*Table 1.2- MESSENGER instruments and the acronyms used.*

| Name | Acronym |
|---|---|
| Mercury Dual Imaging System: | MDIS: |
| -Narrow-Angle Camera | -NAC |
| -Wide-Angle Camera | -WAC |
| Gamma-Ray and Neutron Spectrometer | GRNS |
| X-Ray Spectrometer | XRS |
| Magnetometer | MAG |
| Mercury Laser Altimeter | MLA |
| Mercury Atmospheric and Surface Composition Spectrometer: | MASCS |
| Ultraviolet and Visible Spectrometer | UVVS |
| Visible and Infrared Spectrograph | VIRS |
| Energetic Particle and Plasma Spectrometer: | EPPS: |
| -Energetic Particle Spectrometer | -EPS |
| -Fast Imaging Plasma Spectrometer | -FIPS |
| Radio Science | RS |

Mercury Dual Imaging System (MDIS) includes two CCD cameras, a narrow-angle camera (NAC) and a wide-angle camera (WAC) mounted to a pivoting platform. The camera system provides a complete map of the surface of Mercury at a resolution of 250 meters/pixel, and images of regions of geologic interest at 20–50 meters/pixel. Color imaging is possible only with the narrow-band filter wheel attached to the wide-angle camera (in Fig. 1.3, right panel, is shown the global coverage of Mercury surface obtained with this instrumentation).

Gamma-Ray and Neutron Spectrometer (GRNS) is able to detect gamma rays and neutrons that are emitted by radioactive elements on Mercury's surface or by surface elements that have been stimulated by cosmic rays. It is used to map the relative abundances of different elements and help to determine if there is ice at Mercury's poles, which are never exposed to direct sunlight.

Gamma rays and high-energy X-rays from the Sun, striking Mercury's surface, can cause the surface elements to emit low-energy X-rays.

X-Ray Spectrometer (XRS) was thought to detect these emitted X-ray spectral lines and to measure the abundances of various elements in the materials of Mercury's crust, as magnesium, aluminum, sulfur, calcium, titanium, and iron, in the 1-10 keV range. It can map mineral composition within the top millimeter of the surface on Mercury.

Magnetometer (MAG) measures the magnetic field around Mercury in detail to determine the strength and average position of the field, and search for regions of magnetized rocks in the crust.

Mercury Laser Altimeter (MLA) provides detailed information regarding the height of landforms on the surface of Mercury by detecting the light of an infrared laser as the light bounces off the surface.

Mercury Atmospheric and Surface Composition Spectrometer (MASCS), combining an ultraviolet spectrometer and infrared spectrograph, is able to measure the abundance of atmospheric gases around Mercury and to detect minerals in its surface materials.

The Ultraviolet and Visible Spectrometer (UVVS) can determine the composition and structure of Mercury’s exosphere and study its neutral gas emissions. It also searches for and measures ionized atmospheric species. Together these measurements will help researchers understand the processes that generate and maintain the atmosphere, the connection between

surface and atmospheric composition, the dynamics of volatile materials on and near Mercury, and the nature of the radar-reflective materials near the planet's poles.

The Visible and Infrared Spectrograph (VIRS) measures the reflected visible and near-infrared light at wavelengths diagnostic of iron and titanium-bearing silicate materials on the surface, such as pyroxene, olivine, and ilmenite.

Energetic Particle and Plasma Spectrometer (EPPS) measures the composition, distribution, and energy of charged particles (electrons and various ions) in Mercury's magnetosphere using an Energetic Particle Spectrometer (EPS). It measures also the charged particles that come from the surface using a Fast Imaging Plasma Spectrometer (FIPS).

Radio Science (RS) use the Doppler effect to measure very slight changes in the spacecraft's velocity as it orbits Mercury. This allows to study Mercury's mass distribution and its gravity, together with variations in the thickness of its crust.

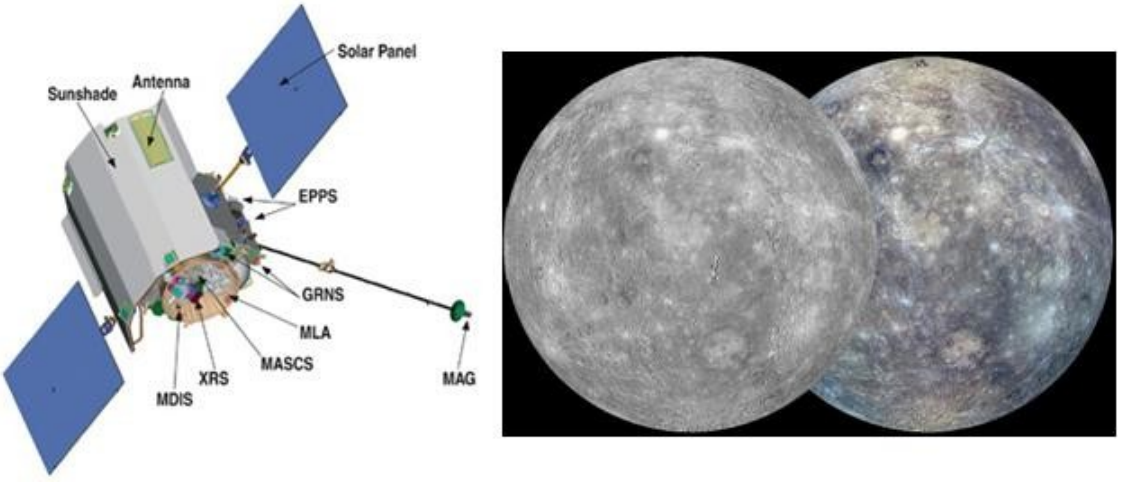


*Fig. 1.3– Left panel: a sketch of the MESSENGER satellite and its instrumentations. Right panel: global coverage obtained with MESSENGER. The globe on the left was created from the MDIS monochrome surface morphology base map campaign. The globe on the right was produced from the MDIS color base map campaign. Each map is composed of thousands of images, and the color view was created by using 3 of the 8 color filters acquired (1000, 750, and 430 nm wavelengths are displayed in red, green, and blue, respectively). Date acquired: February 22, 2013- NASA/Johns Hopkins University Applied Physics Laboratory/Carnegie Institution of Washington*.

During its stay in Mercury orbit, MESSENGER's instruments have yielded significant data and have achieved many of the goals that had been set, including a characterization of

Mercury's magnetic field and the discovery of the presence of O-H bonds possibly due to water ice at the planet's north pole.
In the following pages several of these achievements will be treated and described and they will be a constant reference point in this thesis work.

### 1.2.3 BepiColombo

BepiColombo is named after the mathematician, astronomer and engineer Giuseppe (Bepi) Colombo (Padua, 1920-1984) who discovered the coupling between rotation and revolution of Mercury and carried out a campaign to promote the Italian space research, as previously outlined.
This is the first European mission addressed to Mercury, and arises from the need to understand the mysteries of the planet, not yet completely resolved.
BepiColombo is a joint mission between ESA (European Space Agency) and the Japan Aerospace Exploration Agency (JAXA), executed under ESA leadership, was previously targeted for launch in July 2014, and is now planned for launch in a window opening in August 2015, because of a risk mitigation strategy and budgetary constraints.
The science mission will consist of two separate spacecraft that will orbit the planet (whose orbits are represented in Fig. 1.4, right panel, and compared with that of the MESSENGER satellite). ESA is building one of the main spacecraft, the Mercury Planetary Orbiter (MPO), and the Institute of Space and Astronautical Science (ISAS) at the JAXA will contribute the other, the Mercury Magnetospheric Orbiter (MMO). The MPO will study the surface and internal composition of the planet, and the MMO will study Mercury's magnetosphere.
The instruments aboard the two units are reported in Tables 1.3 and 1.4.

*Table 1.3- MPO instruments and the acronyms used.*

| | |
|---|---|
| BepiColombo Laser Altimeter | BELA |
| Italian Spring Accelerometer | ISA |
| Mercury Magnetometer | MERMAG |
| Mercury Thermal Infrared Spectrometer | MERTIS |
| Mercury Gamma ray and Neutron Spectrometer | MGNS |
| Mercury Imaging X-ray Spectrometer | MIXS |
| Mercury Orbiter Radio science Experiment | MORE |
| Probing of Hermean Exosphere by Ultraviolet Spectroscopy | PHEBUS |
| Search for Exosphere Refilling and Emitted Neutral Abundances (Neutral and ionised particle analyser): | SERENA: |
| - Emitted Low-Energy Neutral Atoms | -ELENA |
| - STart from a Rotating FIeld mass spectrOmeter | -STROFIO |
| - Miniature Ion Precipitation Analyser | -MIPA |
| - Planetary Ion Camera | -PICAM |
| Spectrometers and Imagers for MPO BepiColombo Integrated Observatory System (High resolution and stereo cameras, Visual and NIR spectrometer) | SIMBIO-SYS |
| Solar Intensity X-ray Spectrometer | SIXS |

*Table 1.4- MMO instruments and the acronyms used.*

| | |
|---|---|
| Mercury Magnetometer | MERMAG-M/MGF |
| Mercury Plasma Particle Experiment | MPPE |
| Plasma Wave Instrument | PWI |
| Mercury Sodium Atmospheric Spectral Imager | MSASI |
| Mercury Dust Monitor | MDM |

For launch and the journey to Mercury, the MPO and the MMO will be carried as part of the Mercury Composite Spacecraft (MCS). The MCS comprises, in addition to the two orbiters, the Mercury Transfer Module (MTM), which provides solar-electric propulsion and all services not required in Mercury orbit, and the MMO Sunshield and Interface Structure

(MOSIF), which provides thermal protection and the mechanical and electrical interfaces for the MMO (an example of the structure is shown in Fig. 1.4, left panel). ESA is building the MTM and the MOSIF. Shortly before Mercury orbit insertion, the MTM is jettisoned from the spacecraft stack. The MPO provides the MMO with the necessary resources and services until it is delivered into its mission orbit, when control is assumed by JAXA.

The three components MTM, MPO, MMO are planned to be launched together on an Ariane 5 launch vehicle in 2015. The spacecraft will have a six year interplanetary cruise to Mercury using solar-electric propulsion and gravity assists from the Moon, Earth, Venus and eventual gravity capture at Mercury.

Arriving in Mercury orbit in January 2022, the spacecraft will have a 1-year nominal scientific life.

The main objectives of the mission are: to study the origin and evolution of a planet close to its parent star; to learn about Mercury's form, interior, structure, geology, composition and craters; to investigate Mercury's vestigial atmosphere (exosphere), its composition and dynamics; to study Mercury's magnetised envelope (magnetosphere), structure and dynamics; to investigate the origin of Mercury's magnetic field.

The complex particle environment that surrounds Mercury is composed of thermal and directional neutral atoms (exosphere) originating via surface release and charge-exchange processes, and of ionized particles originated through photo-ionization and again by surface release processes. In order to accomplish the scientific goals, in-situ analysis of the environmental elements is necessary, and for such a purpose it was thought to build SERENA.

SERENA, Search for Exospheric Refilling and Emitted Natural Abundances (Orsini et al. 2010), is the most important instrument package for our study.

As shown in Table1.3, its instrument will include four units: two Neutral Particle Analyzers (ELENA, Emitted Low-Energy Neutral Atoms, and STROFIO, STart from a Rotating FIeld mass spectrOmeter), and two Ion Spectrometers (MIPA, Miniature Ion Precipitation Analyser and PICAM, Planetary Ion CAMera).

In particular, ELENA will investigate the neutral gas escaping from the surface of Mercury, and the related processes; STROFIO will investigate the exospheric gas composition; PICAM will measure the exo-ionosphere extension and composition, and the close-to-planet

magnetospheric dynamics; MIPA will study the plasma precipitation toward the surface and ions energized and transported throughout the environment of Mercury.

Finally, SERENA is an experiment able to provide information on the whole surface-exosphere-magnetosphere system, as well as on the processes involved in this system, subjected to strong interaction with the solar wind and the interplanetary medium (Milillo et al., 2005).

As will be shown in the following chapter, this work aims to provide a contribution to BepiColombo mission, in the framework of a scientific collaboration between Osservatorio Astrofisico di Catania of INAF (Istituto Nazionale di Astrofisica), and IAPS-INAF (Istituto di Astrofisica e Planetologia Spaziali) in Rome, in which operate the Principal Investigators of the experiments ISA (Italian Spring Accelerometer) and SERENA (Orsini et al., 2010) of the space mission.

In Fig. 1.4 are presented all the BepiColombo assembly and a comparison between the trajectories of its two main components and the MESSENGER satellite.

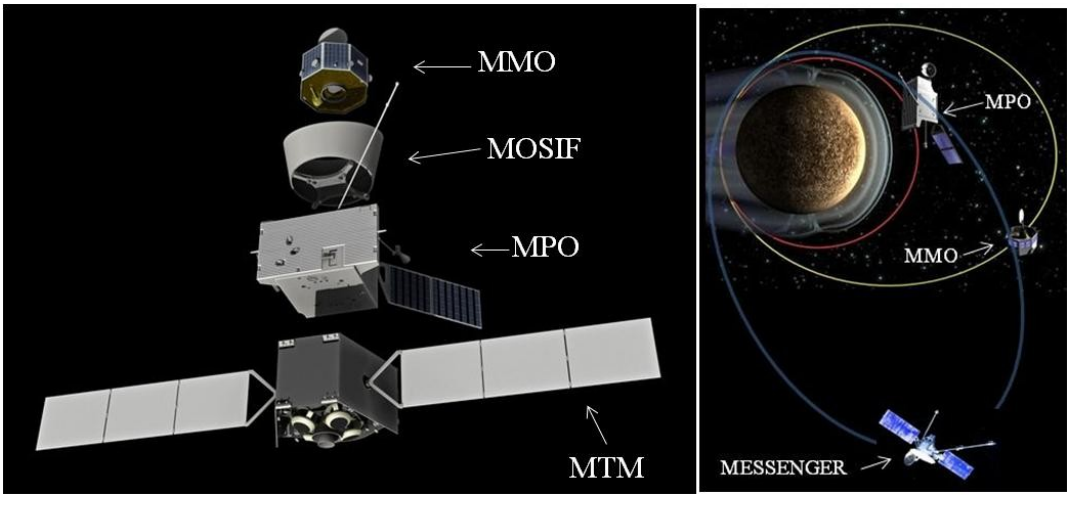


*Fig. 1.4–Left panel shows BepiColombo spacecraft in its cruise configuration. On the right panel are sketched the trajectories of the MPO and the MMO that are compared to the orbit of the NASA MESSENGER spacecraft.*

MESSENGER and BepiColombo scientists are making a variety of cooperative efforts involving data exchange, targeting of observations during the missions, and potentially the sharing of ground resources and collaborative scientific analysis of joint data sets.

As previously mentioned, space missions have given (and will give in future) an essential contribution to the knowledge of this not well known terrestrial planet.
To better understand the characteristics of terrestrial planets, in the next section the main features will be outlined.

## 1.3 Terrestrial planets: Mercury

Terrestrial, or telluric, or rocky planets are made up mainly of silicate rocks or metals. Silicates are a broad class of minerals containing Si. An important species of silicates are orthosilicates having the basic chemical formula $SiO_4^-$, where the oxygen atoms are arranged at the vertices of a tetrahedron, in the center of which there is the silicon atom.
Being the number of oxidation of silicon equal to +4 and that of oxygen to -2, each tetrahedron present an excess of negative charge (-4) that tends to be distributed on the four oxygen atoms: from this the presence of metal cations (Fe, Mg, K, Na, Ca), attracted by the tetrahedral anion, in the composition of these minerals. These metals have a fundamental function in binding together the various structures formed by complex silicate tetrahedrons. Aluminum is the only element that can take the place of the silicon in the center of the tetrahedron (this is called aluminosilicates).
Within the Solar System, terrestrial planets are the inner Earth-like planets closest to the Sun: Mercury, Venus, Earth, and Mars.
These planets have a solid surface and all have approximately the same type of structure: a central metallic core, mostly iron, with a surrounding silicate mantle (in molten and/or solid state) and a rocky crust. The surface is the part of the crust that is immediately in contact with the atmosphere, if this exists; it is rocky and presents a variety of topological features like canyons, craters, mountains, and volcanoes. The Moon is similar to the terrestrial planets, but it is not sure it has an iron core.
On the other hand, the much larger gas giants (or jovian planets) are composed mostly of some combination of hydrogen, helium, and water existing in various physical states. The molecules are in liquid form immediately above the rocky nucleus and in gaseous form in the outermost parts.

Terrestrial planets possess secondary atmospheres, generated through internal volcanism or comet impacts, unlike the gas giants, whose atmospheres are primary, captured directly from the original solar nebula.

During the formation of the Solar System, there were probably many more terrestrial planetesimals, but they likely merged or were ejected.

The uncompressed density of a terrestrial planet is the average density its materials would have at zero pressure and differs from the true average density because compression within planet cores increases their density; the average density depends on planet size as well as composition. A greater uncompressed density indicates greater metal content. A comparison between Mercury and the Earth shows that the first has an uncompressed density of 5.3 g $cm^{-3}$ and the last of 4.4 g $cm^{-3}$, while the mean densities are respectively of 5.4 g $cm^{-3}$ and 5.5 g $cm^{-3}$. Densities generally trend towards lower values as the distance from the Sun increases. The main exception to this rule is the density of the Moon, which probably owes its lesser density to its unusual origin.

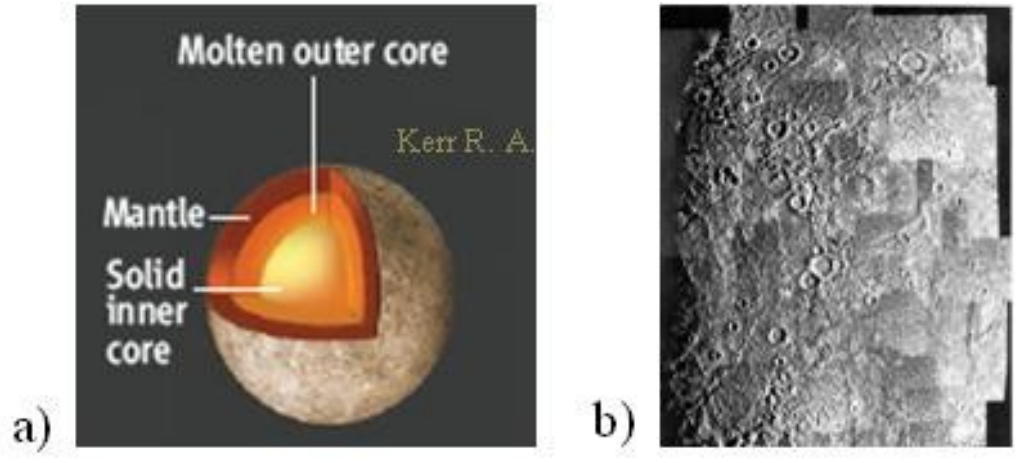


*Fig. 1.5 – A schematic representation of the Mercury's inner structure (a), and a mosaic photo of the Caloris Basin on Mercury's surface taken from Mariner 10 satellite (b) (located half-way in shadow on the terminator).*

Mercury has a metallic, mostly iron, core equal to 60–70% of its planetary mass and could be defined as an iron planet because of its composition, the greater density and smaller

radius with respect to the other terrestrial planets of comparable mass. Iron planets are believed to form in the high-temperature regions close to a star, like Mercury, and if the protoplanetary disk is rich in iron.
In Fig. 1.5 Mercury's inner structure has been reported (a), and a picture of the surface marked by canyons, craters, mountains, and volcanoes (b).
Since Mercury surface is mainly composed of magmatic rocks a brief description about their origin and differentiation will be given in the following section.

# 1.4 Magmatic rocks and minerals

Magmatic rocks (also called eruptive or igneous) are formed after the solidification of magmas, i.e. masses of molten silicates containing various components (FeO, MgO, CaO, etc...) and volatile substances (water, carbon dioxide, hydrogen, methane, etc...).
These rocks form the majority in the Earth's crust, the other two categories being the sedimentary and the metamorphic ones.
Igneous rocks may form with or without crystallization, either below the surface as intrusive (plutonic) rocks or on the surface as extrusive (volcanic) rocks.
Magma can be derived from partial melts of pre-existing rocks, in either a planet's mantle or crust, and cooling. Typically, the melting is caused by one or more of three processes: an increase in temperature, a decrease in pressure, or a change in composition.
Pressure, temperature and partial pressure of the volatile magma components are important on the final process in rock formation as crystallization (slow solidification, as for granite) or amorphization (rapid solidification, as for glasses like obsidian). In Fig. 1.6 are presented a scheme of the rocks formation and two pictures of the results of the solidification process.

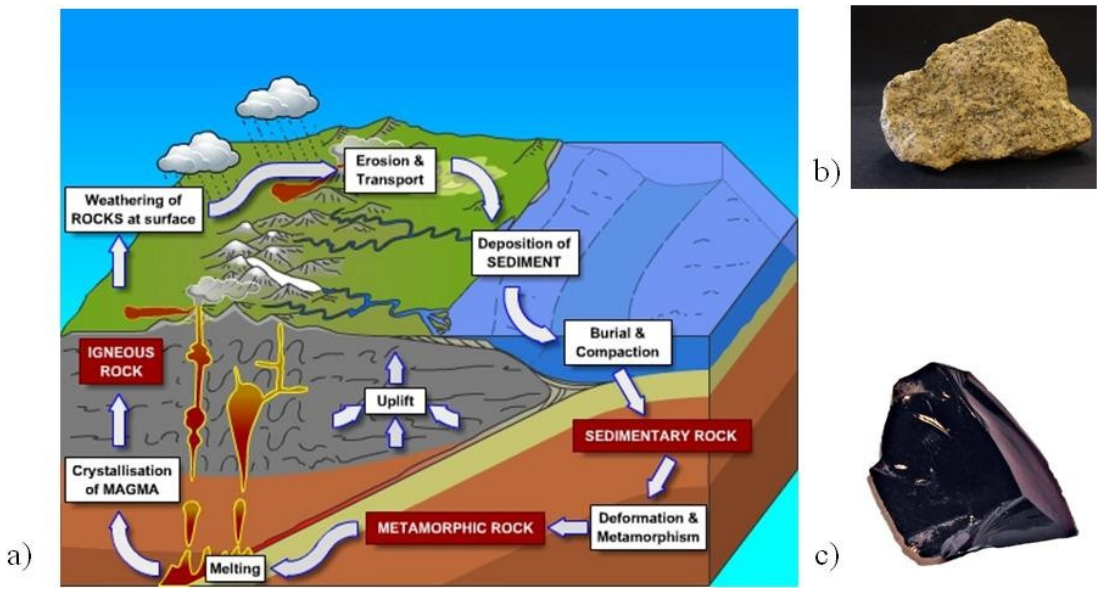


*Fig. 1.6- A pictorial illustration of the rock formation process (a) and the final products due to crystallization (granite, (b)) and amorphization (obsidian, (c)).*

A mineral is a naturally occurring solid chemical substance formed through biogeochemical processes, having characteristic chemical composition, highly ordered atomic structure, and specific physical properties. By comparison, a rock is an aggregate of minerals and/or mineraloids and does not have a specific chemical composition.

The nomenclature and a brief description of the most common minerals, interesting for this study, is given in Tab. 1.5.

*Table 1.5- A selection of the silicates classification of interest for Mercury's surface.*

| SILICATE MINERALS | | |
|---|---|---|
| Characteristics | **Group** | *Examples* |
| NESOSILICATES OR ORTHOSILICATES | | |
| Isolated $[SiO_4]^{4-}$ tetrahedrons connected only by interstitial cations | **Olivine** | *Forsterite - $Mg_2SiO_4$*<br>*Fayalite - $Fe_2SiO_4$* |
| INOSILICATES, OR CHAIN SILICATES | | |
| SINGLE CHAIN | | |
| Chains of silicate tetrahedrons with $SiO_3$, 1:3 ratio | **Pyroxene** | *Enstatite - $MgSiO_3$*<br>*Ferrosilite - $FeSiO_3$*<br>*Diopside - $CaMgSi_2O_6$*<br>*Hedenbergite - $CaFeSi_2O_6$*<br>*Augite - $(Ca,Na)(Mg,Fe,Al)(Si,Al)_2O_6$*<br>*Jadeite - $NaAlSi_2O_6$*<br>*Wollastonite - $CaSiO_3$* |
| DOUBLE CHAIN | | |
| Chains of silicate tetrahedrons with $Si_4O_{11}$, 4:11 ratio | **Amphibole** | *Tremolite*<br>*$Ca_2Mg_5Si_8O_{22}(OH)_2$*<br>*Actinolite*<br>*$Ca_2(Mg,Fe)_5Si_8O_{22}(OH)_2$*<br>*Hornblende*<br>*$(Ca,Na)_{2-3}(Mg,Fe,Al)_5Si_6(Al,Si)_2O_{22}(OH)$* |
| TECTOSILICATES, OR "FRAMEWORK SILICATES," | | |
| Three-dimensional framework of silicate tetrahedrons with $SiO_2$ or a 1:2 ratio. They are aluminosilicates, all but the quartz group | **Quartz** | *$SiO_2$* |
| | **Alkali-feldspars (potassium-feldspars)** | *Orthoclase - $KAlSi_3O_8$*<br>*Anorthoclase - $(Na,K)AlSi_3O_8$*<br>*Albite - $NaAlSi_3O_8$* |
| | **Plagioclase feldspars** | *Oligoclase*<br>*$(Na,Ca)(Si,Al)_4O_8$ (Na:Ca 4:1)*<br>*Anorthite - $CaAl_2Si_2O_8$* |
| | **Feldspathoids** | *Nepheline - $(Na,K)AlSiO_4$*<br>*Sodalite - $Na_8(AlSiO_4)_6Cl_2$* |

In particular, feldspars are minerals found in intrusive and extrusive rocks and also in many types of metamorphic and sedimentary rock. They are a group of rock-forming tectosilicate minerals which make up nearly 75% of the Earth's crust. Feldspars derive from the

crystallization of magma containing K (Potassium-Feldspar (K-spar), $KAlSi_3O_8$), Na (albite, $NaAlSi_3O_8$), Ca (anorthite, $CaAl_2Si_2O_8$) and Ba (celsian, $BaAl_2Si_2O_8$). Solid solutions between K-feldspar and albite are called alkali feldspars. Solid solutions between albite and anorthite are called plagioclase, or plagioclase feldspar. Rocks formed almost entirely of calcic plagioclase feldspar are known as *anorthosite*.

A solid solution is a solid-state solution of one or more solutes in a solvent where the crystal structure of the solvent remains unchanged by addition of the solutes, and the mixture remains in a single homogeneous phase. This often happens when the two elements (generally metals) involved are close together on the periodic table.

Olivines occur in igneous rocks and as a primary mineral in certain metamorphic rocks, while pyroxenes are rock-forming silicate-chain minerals found in many igneous and metamorphic rocks.

As shown in Chapter 4, different combinations of silicates seem to make up the majority of Mercury's surface.

Furthermore, Mercury's location near the Sun renders it a candidate for extensive surface modifications similar to what is observed in lunar soil samples, simulated in laboratory experiments, and proposed to affect lunar soils (Vilas et al., 2008). For this reason, in the following section, the main modifications of lunar soil will be reviewed.

# 1.5 Mercury and the Moon

## 1.5.1 Lunar soil modifications

The layer of loose, heterogeneous material covering the solid rock on a celestial body is named *regolith* or *soil*. Lunar regolith is composed in part of rock and mineral fragments that were broken apart from underlying bedrock by the impact of meteorites.

When micrometeorites (< 1 mm in diameter) strike the lunar regolith, some of the regolith melts and some does not, so the final product is a glass with entrained mineral and rock fragments. These small glassy rocks composed of bits and pieces of older rocks (breccias) so formed are called agglutinates.

Alteration of lunar soil involve several aspects, which will be listed below (Vilas et al., 2008).

Thin nanometer-scale metallic iron (nanophase metallic Fe, $npFe^0$) spheres in amorphous rims and lunar agglutinates are caused by meteoritic impacts, solar wind sputtering or energetic solar and cosmic rays.

In the visible and near infrared spectral region (VNIR) the result of create $npFe^0$ in mafic (Mg, Fe) silicates is to darken the material, decrease the depth of the absorption features and to redden the overall spectrum at wavelengths >600 nm. An example of some weathered rock samples is shown in Fig. 1.7.

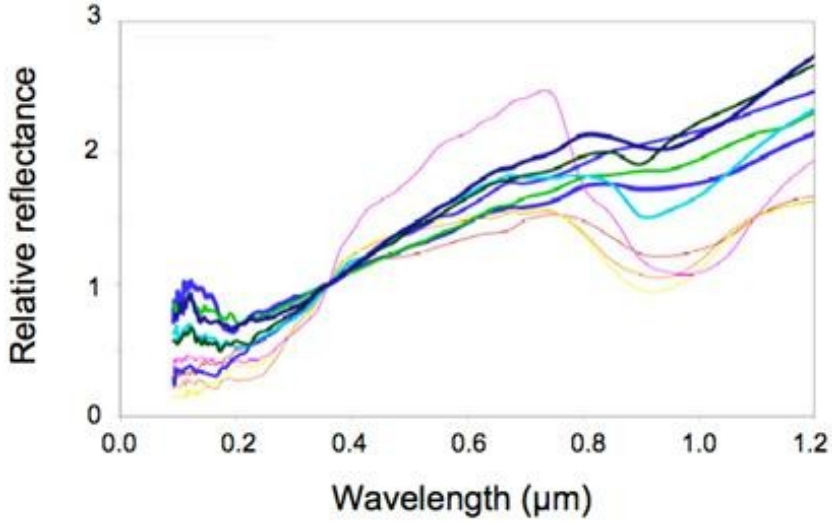


*Fig. 1.7- (from Vilas et al., 2008)- Laboratory spectra of lunar soils (thick lines) and powdered lunar rocks (thin lines). Spectra are scaled to 1.0 at 0.35 μm. The more weathered lunar soils are redder in the visible-NIR, but bluer in the UV region, than the less weathered powdered lunar rock samples.*

Weathering is observed at UV/blue wavelengths, where surface scattering dominates in non opaque minerals, (volume scattering dominates in the VNIR spectral region) and a drop in reflectance marks the transition between volume and surface scattering (150-450 nm).

Furthermore, opaque materials spectra are dominated by surface scattering and are spectrally flat over the UV/blue region.

The Christiansen feature (CF) is the primary mid-infrared (MIR) spectral feature in lunar soils. It occurs near the Christiansen frequency, which is the location in frequency space where the refractive index of the material approaches the refractive index of its surrounding

medium. It appears as a reflectance minimum or a transmission maximum and is a good compositional indicator because its location is correlated to the location of the fundamental vibrational bands and both shifts to longer wavelengths with increasing the complexity of the silicate structure (e.g. feldspars have significantly shorter wavelength CFs than olivines). Petrologically CFs are at shorter wavelengths for felsic rocks (rich in silicate minerals, magma, and lighter elements such as silicon, oxygen, aluminum, sodium, and potassium) and shift to longer wavelengths for more mafic (Fe, Mg) rocks (as shown in Fig. 1.8); also shifts to shorter wavelengths when measured in vacuum, but are not affected by particle size, agglutinates, vitrification. The overall CF intensity is affected by temperature, but not its location (Greenhagen and Paige, 2006).

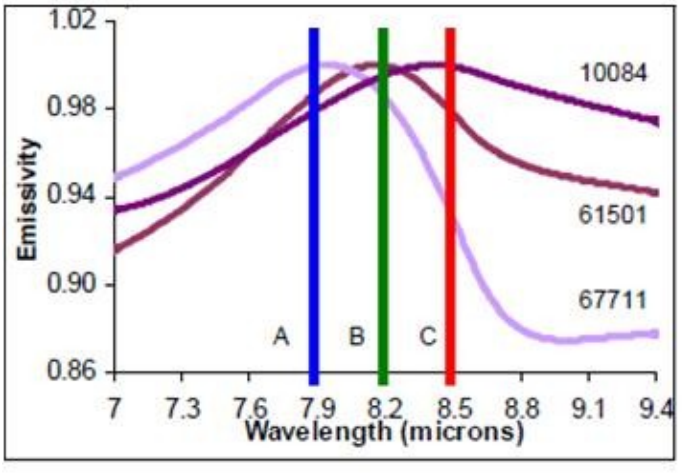


*Fig. 1.8 (from Greenhagen and Paige, 2006)- Spectral emissivity of three samples of lunar soils representing the range of expected CFs. 67711 is an extremely felsic highland soil (light colored areas at higher altitudes); 61501 is a typical highland soil, and 10084 is a mafic mare soil (dark basaltic plain). The blue (A), green (B) and red (C) lines represent the location of the narrow-band filters on the lunar infrared radiometer Diviner.*

In addition, lunar soil behave as terrestrial orthopyroxenes (pyroxenes which crystallize in the orthorhombic systems) with a slight deviation due to the higher Ca content in the lunar pyroxene (CF ≈8 μm) (Carli et al., 2008).

With the aim to look for any hypothetic similarity between Mercury and the Moon, in the next section will be presented a comparison of the existing data.

## 1.5.2 Similarity with the Moon?

Thermal emission measurements at microwave wavelengths (0.3-20.5 cm) indicate that Mercury's surface is 40% more transparent than lunar highlands (light colored areas on the Moon at higher altitudes).

This observation, together with the absence of the 1μm absorption band, have led to the inference that Mercury's crust contains lower abundances of iron plus titanium than the lunar highlands (Denevi et al., 2009).

Vernazza et al. (2010) in addition, comparing Mercury's spectra with lunar ground based spectra and lunar soil spectra collected in laboratory, found that Mercury's surface composition is likely to be quite different from the Moon's.

While low-Ca iron-rich pyroxenes are the main surface components of the Moon, a Ca-rich clinopyroxene (in the hedenbergite-diopside series, $CaMgSi_2O_6$-$CaFe^{2+}Si_2O_6$) is likely to be a main component in Mercury's surface. They also found that Mercury's slope is less red than that of the Moon (in agreement with MESSENGER's results), and composition rather than space weathering is the main cause for this difference.

An answer to the differences in the reflectance between Mercury and the Moon could be given by Lucey et al. (2011) who, using Mie theory and modifying the Hapke radiative transfer model of the effects of space weathering, found that submicroscopic iron particles (>50 nm) are much more abundant on Mercury (3.5% wt) than on Moon (0.5 % wt). Such particles darken their host material but do not redden their spectra.

These results are confirmed also in other comparisons between Mercury's and Moon's spectra, obtained by the MESSENGER spacecraft and spanning the wavelength range 220–1450 nm (Holsclaw et al., 2010, Fig.1.9).

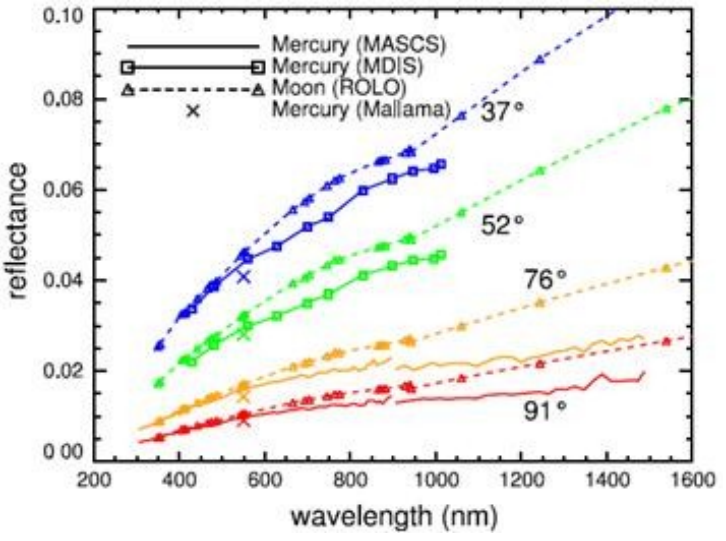


*Fig. 1.9 (from Holsclaw et al., 2010)- Absolute reflectance of Mercury from MASCS and MDIS compared with the reflectance of the Moon at equivalent waxing phase angles acquired by the ground-based telescope Robotic Lunar Observatory (ROLO).*

The brightness of an object is a function of the phase angle (the angle Sun-object-observer), which is generally smooth, except for the so-called opposition spike near 0° and when the object becomes fainter as the angle approaches 180°.

It is shared indeed that the absolute reflectance of Mercury is lower than that of the nearside waxing Moon at the same phase angle, with a spectral slope that is less steep at visible and near-infrared wavelengths, and the ratio of Mercury reflectance to that of the Moon highlights the differences between the spectral properties of the two bodies (McClintock et al., 2008).

In Fig. 1.10 the disk-averaged reflectance (observed spectral radiance of the surface divided by the radiance from a hypothetical normally illuminated Lambertian disk) of Mercury and the Moon is presented (A). In Fig. 1.10 (B) Mercury's MUV reflectance (blue curve) exhibits a distinct departure from a linear trend (blue dashed line) at wavelengths < 300 nm, that is not observed for the Moon (red curved and dashed line), and that could be due to the presence of oxygen-transition metal charge transfer bands (OMCT, that is a transfer of a fraction of electronic charge between the molecular entities) caused by $Fe^{2+}$ and/or $Ti^{4+}$.

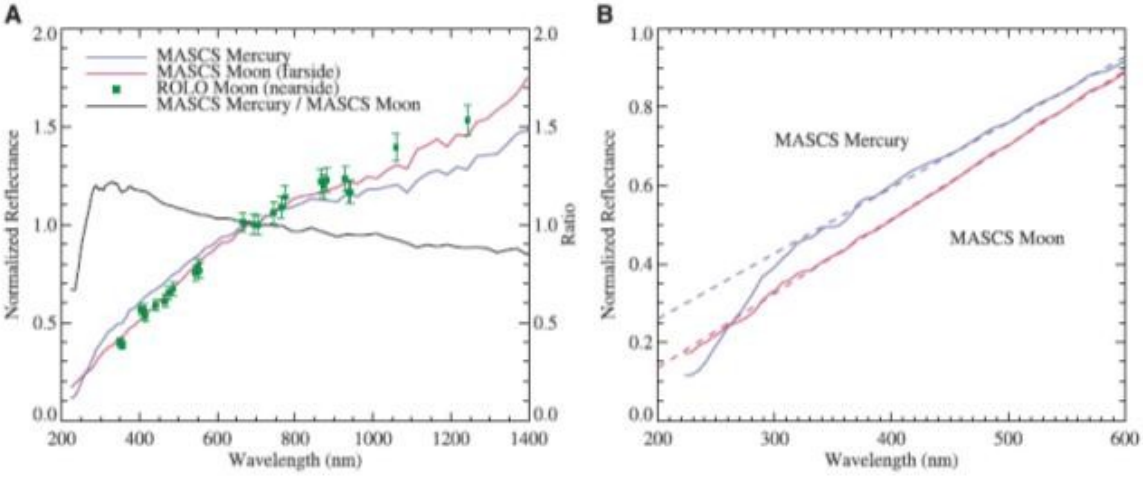


*Fig. 1.10 (from McClintock et al., 2008)-**A**: MASCS disk-averaged reflectance of Mercury and the Moon, along with a ROLO- derived full-disk spectrum of the waxing phase (87°) of the lunar nearside, composed predominantly of highland terrain. The spectra are scaled to a value of 1.0 at 700 nm. **B**: Mercury's MUV reflectance (blue curve).*

The presented outcomes and the lack of an absorption feature at a wavelength near 1000 nm are interpreted as evidence for a Mercury surface composition that is low in ferrous iron within silicates but is higher in the globally averaged abundance of spectrally neutral opaque minerals than the Moon (Holsclaw et al., 2010).

Denevi et al. (2009) then concluded that, because immature materials (i.e. little exposed to space weathering) on Mercury are as much as 30% lower in reflectance than comparable materials on the Moon, Mercury's crust seems not to be anorthositic but possibly rich in low-Fe pyroxenes, or olivine, and a spatially variable low-reflectance component.

To better study Mercury's surface composition, in the next section some existent experiments on Mercury's analogue materials will be treated.

# 1.6 Experiments and modeling in literature

## 1.6.1 Reflectance spectra and compositional heterogeneity

To support MERTIS (Mercury Thermal Infrared Imaging Spectrometer, 7-14 μm) and for cross-calibration with other instruments aboard BepiColombo and MESSENGER MASCS, Moroz et al. (2007) have done several spectral reflectance measurements (0.5-18 μm) of Mercury analogue materials together with a comparison of the thermal infrared biconical reflectance spectra ($1-R_b$) of the samples (slabs or particulate of various particle sizes) to their emissivity (E) to evaluate deviations from the Kirchhoff's law ($E=1-R_b$). Kirchhoff's law is in fact valid within certain limit for directional-hemispherical geometry, while most reflectance data on minerals and rocks are acquired at biconical geometry. A space weathering simulation experiment was also made on two FeO-poor samples of plagioclases (andesine-labradorite $(Ca, Na)(Al, Si)_4O_8$)) irradiated with nanosecond pulsed laser.
The authors found significant variations in reflectance values and absorption band contrasts with grain size in the 0.5-18 μm spectral region (Fig.1.11, left panel) and, in high-resolution NIR reflectance spectra, were recognized weak absorption features imputable to OH and/or $H_2O$ bearing weathering products (Fig. 1.11, right panel).

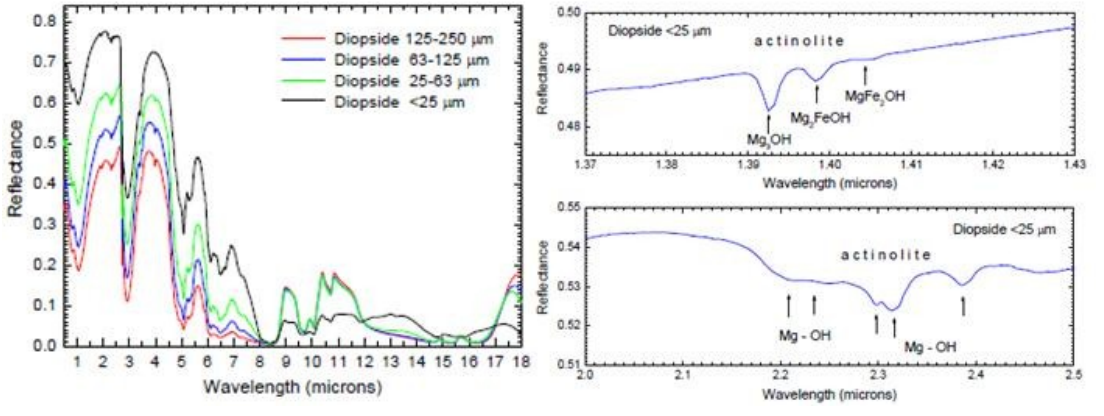


*Fig. 1.11 (from Moroz et al., 2008)- Left panel: Biconical reflectance spectra of diopside separates. Right panel: Identification of weak actinolite ($Ca_2(Mg, Fe)_5Si_8O_{22}(OH)_2$) absorption bands (Metal-OH overtones) in NIR reflectance spectra of a diopside ($CaMgSi_2O_6$) powder.*

Furthermore, deviations of $1\text{-}R_b$ from E are ≤ 3% for loose powders at ambient pressure, but are very significant in the cases of slabs and compact fine powder (see Fig.1.12).

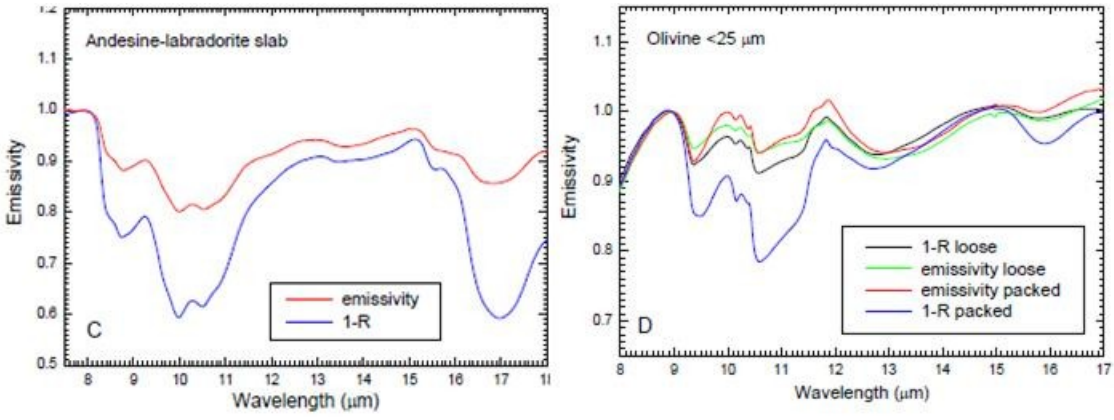


*Fig. 1.12 (from Moroz et al., 2008)- TIR E vs. 1-Rb for andesine-labradorite unpolished slab (left panel), and loose and packed fine (<25 μm) olivine powders (right panel).*

Packing effects are much less pronounced in emission than in biconical reflectance.

These effects have to be taken into account when comparing remote sensing emission spectra of planetary surface areas covered with bare rocks or compact crust with laboratory spectra at biconical geometry on slabs or simulated crust.

Finally, it is important to underline that these results were performed at ambient pressures and may not be applicable in low pressure environments.

The simulation experiment of a micrometeorite bombardment onto an andesine-labradorite sample highlight no darkening, but mild NIR (Near-InfraRed) reddening, as can be seen in Fig. 1.13 (left panel). This could indicate that the presence of FeO in the target minerals could be crucial to produce space darkening and reddening of planetary regoliths induced by micrometeorite bombardment.

Nevertheless Yamada et al. (1999) results seem to contradict these hypotheses.

Irradiating with a pulse laser beam hypersthenes ($(Mg,Fe)SiO_3$) and enstatite ($MgSiO_3$-$(Mg,Fe)SiO_3$) (with hypersthenes containing 70% more FeO than enstatite), with total irradiated energy in unit area 240 $mJmm^{-2}$, for 30 mJ pulse energy, was noticed that whereas the spectra show reddening in the infrared region, absorption band features around 1μm (ferrous iron in both olivines and pyroxenes- Strazzulla et al., 2005 and reference therein) and 2μm (pyroxenes) are not largely changed (Fig. 1.13, right panel).

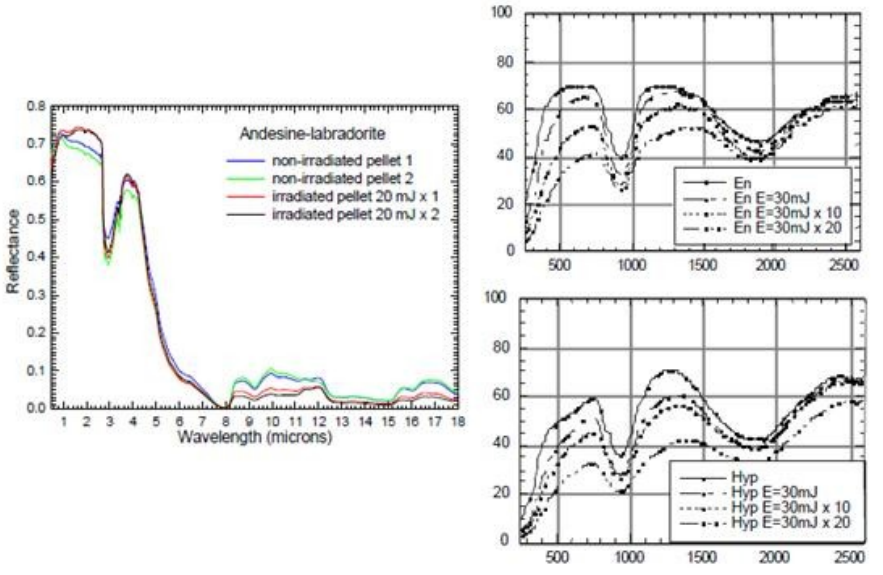


*Fig. 1.13 (Left panel: from Moroz et al., 2008)- Biconical reflectance spectra (0.5-18 μm) of non-irradiated and laser-irradiated plagioclase pellets. (Right panel: from Yamada et al., 1999)- Reflectance spectra of (top) enstatite, and (bottom) hypersthene pellet samples before and after the irradiation of pulse laser. As for enstatite and hypersthene, laser irradiation was performed repeatedly at 30mJ pulse energy. Vertical axis is reflectance (%) and horizontal axis is wavelength (nm).*

So their results show that darkening and reddening are not dependent on FeO abundance.

Another important step is to understand the exosphere of Mercury, because it provides information on the planet's atomic surface composition. This study will be presented in the next section.

## 1.6.2 Exosphere-surface relationship

According to three MESSENGER flybys, Mercury's exosphere is known to contain H, He, Na, K, Ca, Mg and, possibly, O (Burger et al., 2010). By extrapolating from these spacecraft atmospheric measurements, with the help of experimental results and theoretical modeling, it could be possible to deduce the major surface sources and sinks for each atmospheric component, in particular sodium, as well as to constrain the mechanisms involving thermal desorption and interactions between the surface and its space environment. These

interactions include bombardment of the surface by photons, solar wind ions and electrons, as well as meteorites (Dukes et al., 2011 and references therein), and will be described below.

A different exospheric distribution of neutral Na, Ca and Mg in intensity and morphology, obtained analyzing UVVS-MASCS measurements, implies differences in the regions of the surface from which the material was derived and in the mechanism responsible for supplying each species to the exosphere.

Burger et al. (2010), developing a Monte Carlo model of the exosphere, propose Photon Stimulated Desorption (PSD) as a primary source of Na atoms from the top few nanolayers of the regolith, in the tail region (anti-sunward of the planet, between about 2 and 8 Mercury radii, formed by radiation pressure on atoms ejected from the surface). On the dayside, Na is rapidly depleted due to the high UV photon flux, while ion precipitation in regions of the surface open to the solar wind increases the diffusion rate of Na, which produces an increased flux of Na at high latitudes, detected by MASCS during the fantail observations (occurred as MESSENGER passed through Mercury's shadow, near the closest approach to the planet) (see Fig. 1.14).

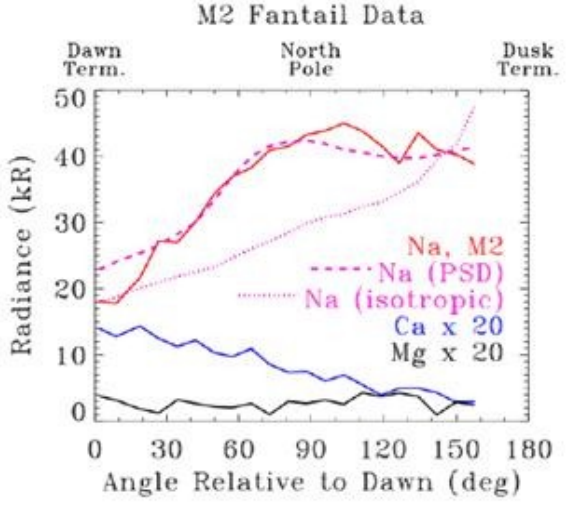


*Fig. 1.14 (from Burger et al., 2010)- Comparison of Na (red), Ca (blue), and Mg (black) observations during the second MESSENGER flyby (M2). The magenta lines show model simulations of the Na exosphere. The dotted line indicates an isotropic sodium source. The dashed line shows a PSD source with the flux enhanced at high latitudes by ion precipitation.*

However, a PSD or thermal source presume a spatial distribution that is not obtained by the exospheric Na around Mercury: as has been seen, it is at time concentrated at northern or southern high latitudes and its distribution changes significantly over short time intervals.

To elucidate the contribution of sputtering by solar wind ions to the atmosphere of Mercury, Dukes et al. (2011) performed laboratory simulations of solar wind interaction with planetary surfaces irradiating with 4 keV $He^+$ ions the Na-bearing tectosilicates as well as adsorbed Na layers deposited on albite and on olivine (a neosilicate that does not contain Na). Sodium released from the surface of Mercury can, indeed, re-deposit as a coating on different mineral surfaces by the action of gravity. The terrestrial plagioclase feldspars were chosen for their relatively high Na content and mineralogical similarity to anorthosite (lunar highland basalt): albite ($NaAlSi_3O_8$), labradorite [$(Na, Ca)Si_3O_8$], anorthoclase [$(K, Na)AlSi_3O_8$], and olivine [$(Mg, Fe)_2SiO_4$] which contains no intrinsic Na was used as a control.

Measurements of the sputtering of Na from these minerals were made using X-ray photoelectron spectroscopy (XPS), while secondary ion mass spectroscopy (SIMS) analyses of the sputtered flux showed that a large fraction of the Na is sputtered as ions rather than as neutral atoms. The other ions ejected from the mineral surface are $Al^+$, $Si^+$ (all isotopes in proportion), $Ca^+$ (and $Ca^{++}$), $O^+$, $C^+$, as well as one Na-bearing molecular ion: $NaO^+$ (Fig. 1.15, left panel). The authors found that the release of Na from a mineral surface strongly depends on the abundance of Na in the soil and the irradiation history. Samples of terrestrial albite, anorthoclase and labradorite (Fig. 1.15, right panel) were studied to measure the surface depletion of intrinsic sodium (bound within the mineral structure) under ion irradiation. In all cases, the Na concentration follows a similar exponential decay, with a depletion cross section (decay constant) of $1.4 \times 10^{-17}$ $cm^2$ for albite, $1.2 \times 10^{-17}$ $cm^2$ in anorthoclase, and $0.8 \times 10^{-17}$ $cm^2$ for labradorite.

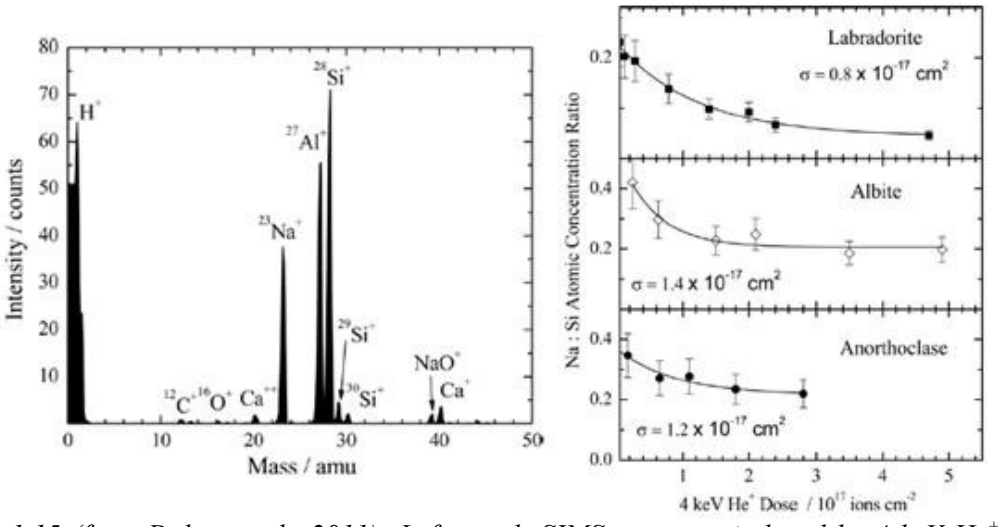


*Fig. 1.15 (from Dukes et al., 2011)- Left panel: SIMS spectrum induced by 4 keV $He^+$ on albite that has been partially depleted of Na by high fluence irradiation. Right panel: Decrease in the surface concentration of Na relative to Si in cleaved minerals vs. fluence of 4 keV $He^+$.*

Furthermore, few measurements of the flux and energy distribution of electrons impacting Mercury's surface were made by Mariner 10 and MESSENGER XRS, which indicated high energy electrons impacts on the night side.

Orlando et al. (2010) performed a laboratory *Electron Stimulated Desorption* (*ESD*) experiment in an Ultra High Vacuum system (with base pressure of about 5 x $10^{-10}$ Torr) using pulsed (100 ns; 20-100 Hz) low energy (5-500 eV) electron beams, with fluxes of about $10^{10}$-$10^{14}$ electrons/cm$^2$s, to cryogenically cooled glasses, minerals or molecular solid targets, like Na bearing silicates. To characterize the quality and chemical composition, a FTIR (Fourier Transform Infrared Spectroscopy), temperature-programmed desorption (TPD) and optical reflection were used, while the ions produced and released were measured using a quadrupole mass spectrometer (QMS) and a ToF (time of flight) mass spectrometer. They used a 3-D hybrid model to simulate conditions of the first two flybys, to compute electron impact flux and the energy distribution. A magnetosphere of Mercury qualitatively similar to that of Earth was found, and computations for magnetic field conditions during the first flyby indicated an electron precipitation highly focused in the northern hemisphere at ~60° N latitude near noon with flux of ~$10^{10}$ per cm$^2$s and typical energy of 0.5 keV. For conditions during the second flyby, precipitation occurs

predominantly at the equator, with energies of 1-5 keV and flux about the same of the first flyby, $10^{10}$ per $cm^2$s. From electron irradiated silicates direct yields of $Na^+$, $O^+$, $H^+$ and trace amount of water and $Si^+$ have been determined. The relative ion abundances observed, using 100 eV electrons, was: $H^+ > O^+ > Na^+ > Si^+$ and the ion yield showed a linear dependence on electron flux.

To conclude, the exospheric distribution of neutral Na, Ca and Mg could be due to photon stimulated desorption (Burger et al., 2010) or ion sputtering (Dukes et al., 2011), while electron stimulated desorption gives part of the ionized exosphere (Sprague et al., 2010; Orlando et al., 2010). Observations, experiments and modeling, regarding the exosphere, are then an indispensable tool for adding new pieces to the knowledge of the constituents of the Mercury's surface.

However, the information available so far in this regard are not entirely complete and the literature is divided on the interpretation of some data, as for the case of *sulfides*, which will be introduced in Chapter 4.

Trying to summarize the literature relative to MESSENGER, ground-based and experimental data, in the next paragraph the main characteristics of Mercury's surface and exosphere so far found will be traced.

## 1.7 Outline: which are, then, Mercury's surface building blocks

Ground observations in the visible, near and medium infrared spectral region (0.4-25 μm) of Mercury have shown a heterogeneous mineralogical composition of the surface (i.e. silicates, feldspars, olivines, pyroxenes, iron oxides, which have been described in §1.4) and the presence of sodium, potassium and calcium, confirmed by the new data collected from the MESSENGER satellite.

Mercury has a generally volcanic surface with high abundances of magnesium and calcium (Nittler et al., 2011) and should consist largely of agglutinates (Vilas et al., 2008), basaltic material (Denevi et al., 2009), a small part of sulfides (0.58% mol): ZnS, CaS (oldhamite), MgS (komatiite), FeS (troilite), elemental S (Wurz, 2010; Helbert, 2007, 2012), up to 4 wt. % (Nittler et al., 2011), plagioclase feldspars (D'Amore et al., 2011; Vilas et al., 2008), (or Mg/Ca rich garnets ($X_3Y_2SiO_4$), Sprague et al., 2009), thermally shocked glassy phase and shocked olivine (D'Amore et al., 2011).

Earth and Mercury could have formed, at least partly, from enstatite chondrites (EC)[1] materials (the most reduced naturally occurring materials of the Solar System). The cubic monosulfide series (Mg,Mn,Ca,Fe)S are common phases in these meteorite groups (Malavergne, et al., 2012), and in *aubrites* (*enstatite achondrites*, Fogel et al., 2005).

Ground based reflectance spectra showed strong reddening and no 1 μm silicate absorption feature, which means low (< 6% weight) FeO silicates (Denevi et al., 2009).

Furthermore, in the VIRS spectral region Fe-free feldspars are featureless, while the crust should be rich of low-Fe-pyroxenes or olivine and Low Reflectance Material (LRM; Denevi et al., 2009).

As happens for lunar soil, in the VNIR $npFe^0$ in mafic silicates darkens the material, decreases the depth of the absorption features and reddens the overall spectrum at wavelengths >600 nm (Vilas et al., 2008) and an opaque phase, like ilmenite ($FeTiO_3$) (Denevi et al., 2009, Blewett et al., 2013) or Rutile ($TiO_2$) (Sprague, 2009), match the LRM.

Identification of OH and/or $H_2O$ are observed in the spectral reflectance measurements (0.5-18 μm) of Mercury analogue materials, imputable to weathering products (Moroz et al., 2008).

Apatite, ($Ca_5(PO_4)_3$[F, OH, Cl]) (Wurz, 2010) could be a possible source of halogens and hydroxyl species ($Ca_5(PO_4)_3OH$), together with amphiboles ($SiO_4$ chains with Fe, Mg and OH group) (Sprague, 2009), while neutron absorption observed in exosphere is consistent with Fe, Ti, Sm, Gd and Mn-bearing pyroxene on the surface, for example Mn-bearing *clinopyroxene* (Sprague. et al. 2010).

Furthermore, different distribution of neutral Na, Ca and Mg observed in the exosphere implies differences in the regions of the surface from which the material was derived and the mechanism responsible for supplying each species to the exosphere (Burger, et al., 2010).

Spectral reflectance measurements (0.5-18 μm) of Mercury analogue materials also highlighted significant variations in reflectance values and absorption band with grain sizes, slabs or fine powder and solar phase angles (Moroz, et al., 2007; Domingue, et al., 2010).

[1] *Chondrites* are stony meteorites constituted by *chondrules*, millimeter-sized spherical objects originated as freely floating, molten or partially molten droplets in space, rich in the silicate minerals olivine and pyroxene. *Enstatite chondrites* (also E-type chondrites) are a rare form of meteorite dominantly composed of enstatite-rich chondrules plus abundant grains of metal and sulfide minerals.

The detection of neutral Mg and ionized $Ca^+$ in the exosphere, obtained during M2 and M3 MESSENGER flybys respectively, means that a substantial source of Mg at Mercury's surface, such as Mg-pyroxene (Denevi et al., 2009; Sprague et al., 2010) is required.

As already mentioned, the exospheric distribution of neutral Na, Ca and Mg could be due to *Photon Stimulated Desorption* (*PSD*) (Burger et al., 2010) or ion *sputtering* (Dukes et al., 2011), with *Eletcron Stimulated Desorption* (ESD) contributing to part of the ionized exosphere (Sprague et al., 2010; Orlando et al., 2010).

On the other hand, Dukes et al (2011) reporting some MESSENGER results, highlight that in the mercurian exosphere $Na^+$ is the dominant ionic species and a significant amount of exospheric Na is suprathermal (with average kinetic energies equivalent to temperatures of several thousand degrees). The energies are consistent with sputtering, photo desorption by solar UV and meteoritic impact vaporization processes that eject alkalis present in the soil within silicate minerals or oxides in the exosphere.

While photo desorption is solely a surface process, sputtering and meteoritic impact can remove Na even from beneath the surface. The ejected neutral Na supplied to the exosphere can be eventually photo-ionized and picked-up by magnetic fields, contributing to Mercury's ion population.

In conclusion it can be observed how space missions have opened new horizons to the knowledge of Mercury but much remains to be known. An essential contribution can be given by terrestrial experiments on Mercury analogue materials and comparison with observations.

This work is part of a larger project aimed at the study and characterization of materials to be used to test the Development Model of ELENA (Emitted Low-Energy Neutral Atoms), one of the instruments which will fly on board the joint ESA-JAXA mission BepiColombo.

The samples studied in this work are etnean volcanic soils and silicates.

Specimen of etnean soils are considered as a template of magma on the surface of Mercury because they present featureless spectra in the ultraviolet spectral region. Silicates (namely nepheline, jadeite and sodalite) which contains Na and K are considered as template to investigate the origin of Na and K in the exosphere of Mercury. Mercury is exposed to solar wind ions. The effects of ion bombardment on these samples are also investigated.

# CHAPTER 2

# EXPERIMENTAL TECHNIQUES

## 2.1 Experimental analytical techniques:

## Laboratory for Experimental Astrophysics (LASp)

The instruments on board BepiColombo, in particular ELENA (Emitted Low Energy Neutral Atoms), will be able to perform measurements on the spatial distribution of neutral atoms and will enable to make estimates of the overall rate of loss of particles from the planet and get crucial information about processes of emission, dissociation, acceleration of particles to trace the evolution of Mercury.

Waiting for the ELENA measurements, some contribution to the understanding of the above mentioned processes have been given at the Laboratory for Experimental Astrophysics (LASp) at the Osservatorio Astrofisico di Catania (http://web.ct.astro.it/weblab), whose instrumentations and working procedures will be described below.

In Fig. 2.1 is presented a scheme of the mechanisms which cause the regolith formation and contribute to the exosphere's construction.

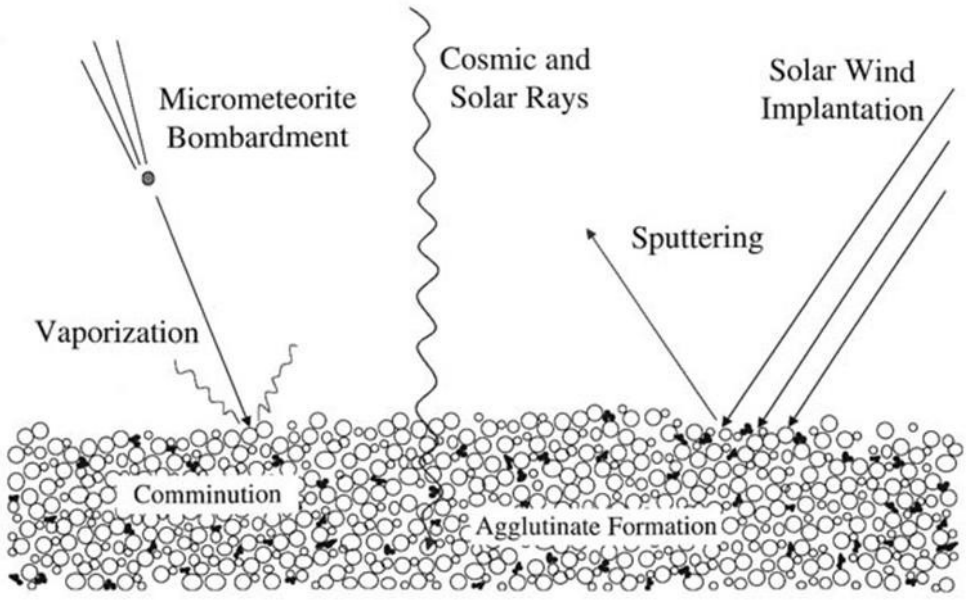


*Fig. 2.1 – The space weathering which affect the surfaces of airless bodies as Mercury, and contributes to the formation of the regolith and the exosphere.*

The physical-chemical environment of Mercury surface can be reconstructed and the space weathering phenomena can be simulated, up to a certain degree, if proper instruments are jointly set up.

The Laboratory for Experimental Astrophysics (LASp) offers the ability to characterize materials, bombarding them with ions at different energies (30-400 keV), acquire 'in situ' transmittance and 'ex situ' reflectance spectra in the visible, ultraviolet and infrared spectral regions and Raman spectra, before and after irradiation.

In this respect LASp can give an important contribution to analyze Mercury-like materials under the effect of ion bombardment.

The analysis of the spectra obtained after ion irradiation, at different fluences, will help to study the physical-chemical modification of the mineral processed.

In particular, the experimental apparatus is composed of:

- an ultra high vacuum analysis chamber (P≈ $10^{-9}$ mbar),
- a spectrophotometer (Bruker Vertex 70 Fourier transform, FTIR), operating in the Visible and Infrared spectral region (0.6-25 μm), to acquire spectra of samples placed inside the chamber (*in situ*),
- two other spectrophotometers (Perkin-Elmer Lambda 19 and Bruker Equinox 55) operating in the UV-Vis-NIR, (0.19-2.5 μm, 4000-50000 $cm^{-1}$) and IR (7500-400 $cm^{-1}$) spectral regions respectively, for hemispherical and biconical *ex situ* spectra (the optical set up utilized for the biconical reflectance is reported in Fig. 2.5),
- an ion implanter.

A picture of the LASp instrumentation is shown in Fig. 2.2.

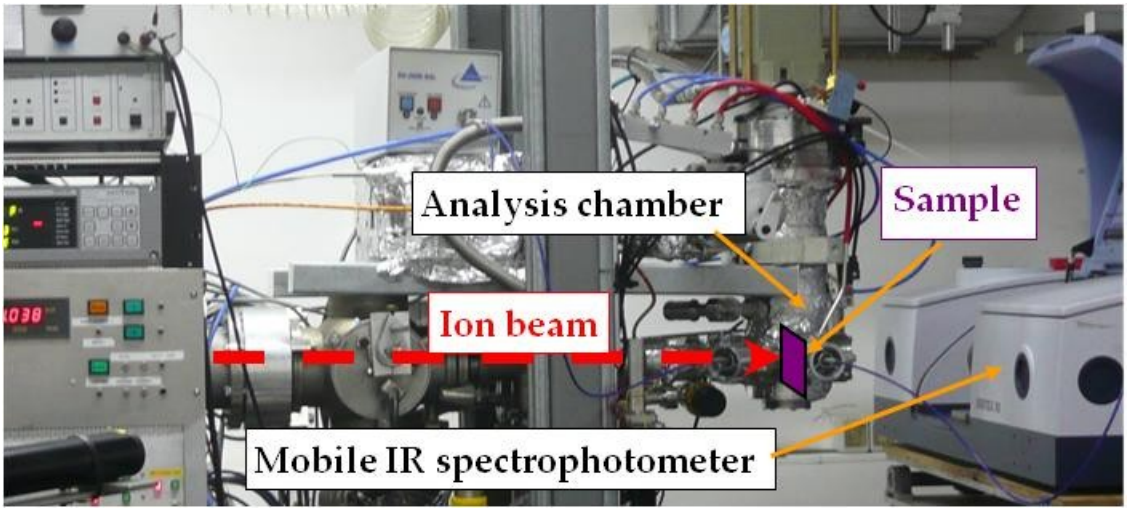


*Fig. 2.2 – The experimental apparatus of the Laboratory for Experimental Astrophysics (LASp) in Catania.*

More details on the instruments and on the joint assembly are presented below.

A crucial aspect to get the more realistic possible simulation of Mercury surface processes, is the choice of material to be used as target-samples. Typically they are minerals (mostly silicates), which approximate the best models of Mercury's surface based on reprocessing of data existing in the literature (Wurz et al, 2010).

Some samples have also been irradiated with ions ($H^+$, $Ar^+$), at energies in the range of 200-400 keV, at room temperature, in the stainless steel vacuum chamber in an attempt to reproduce, in this way, the processing operated by solar ions on the surface of Mercury.

## 2.2.1 The analysis chamber

The analysis chamber (Brunetto & Strazzulla, 2005) (Fig. 2.3), has a cylindrical shape with a diameter of 7.5 cm, is made of stainless steel and is provided with windows which allow the passage of the radiation from the analysis instruments (spectrophotometers).
It is connected with the ion implanter, so that samples mounted in the chamber can be irradiated with ions and analyzed by the spectrometers.

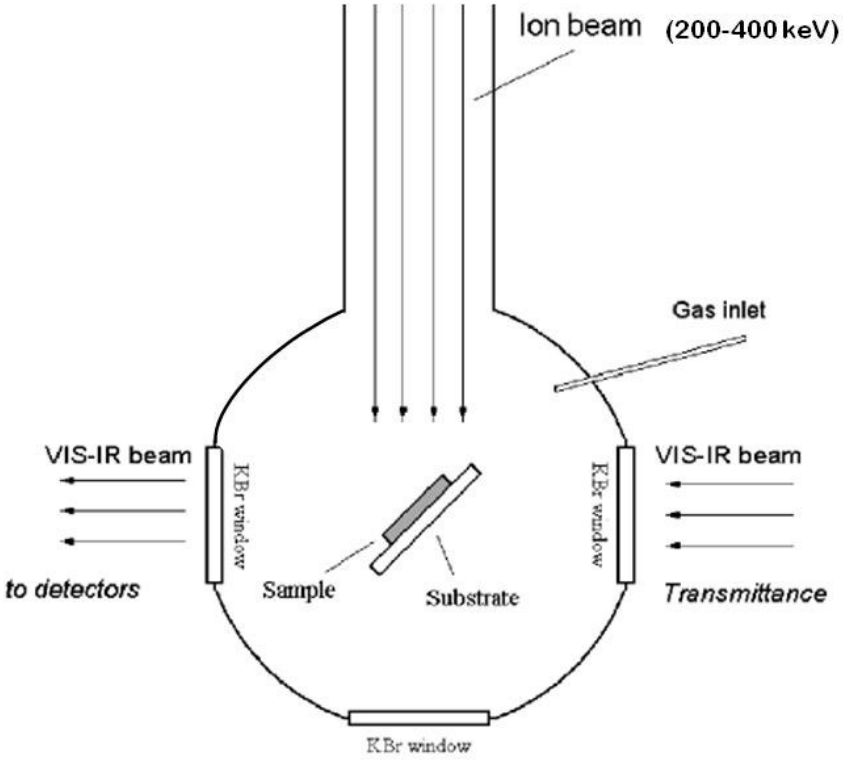


*Fig. 2.3 – A detailed sketch of the analysis chamber (pressure around $10^{-9}$ mbar).*

A system of vacuum pumps (rotary, turbo molecular and ionic) allows to obtain pressures down to $10^{-9}$ mbar. The sample holder is inclined by 45° with respect to the direction of the

ion beam, in order to acquire transmission spectra, even during irradiation, without tilting or moving the sample.
The chamber can be housed in the sample holder of the mobile spectrophotometer, as shown in Fig. 2.2.

### 2.2.2 The spectrophotometers

The mentioned spectrophotometers acquire transmittance and reflectance spectra in the UV, visible, NIR and IR spectral regions. Those acquired in this work are reflectance spectra, i.e. they measure the intensity of the radiation reflected by the samples.
In the next sections (A and B) a detailed description of these instruments and the acquisition procedure will be given.

## Section A: IR spectrophotometer and data

The IR spectrophotometer is constituted by:

- an infrared source,
- an optical system for the collimation and collection of the IR radiation,
- a *Michelson interferometer*,
- a detector.

According to the scheme shown in Fig 2.4, a reflectance accessory (in which the sample is housed) is used for biconical reflectance:

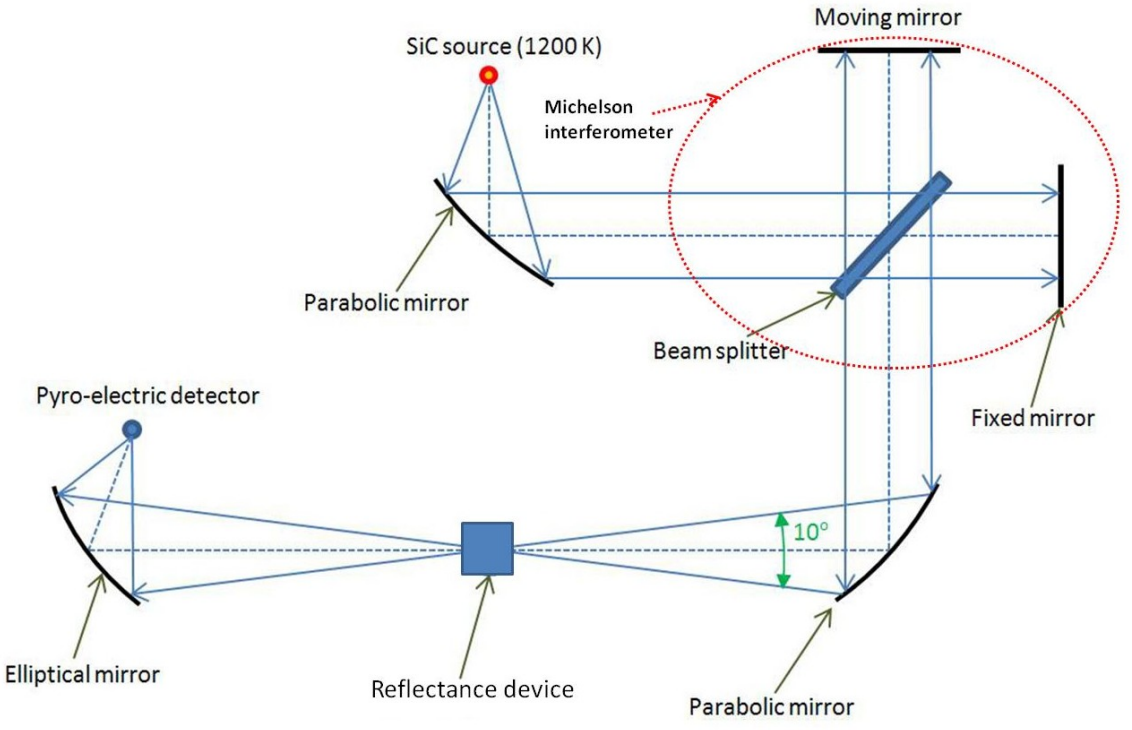


*Fig. 2.4 – Schematic of the Fourier transform IR spectrophotometer.*

The infrared spectrophotometer is an Equinox 55, operating in the spectral region of 7500-400 $cm^{-1}$ (MIR), with a resolution of 1 $cm^{-1}$. The infrared source is constituted by a cylinder of silicon carbide (SiC) heated at about 1200 K, with the emission maximum around 3 μm; its radiation is collimated by a parabolic mirror toward the *Michelson interferometer*. Schematically, the interferometer comprise two plane mirrors, a fixed and a moving one, and a semi-reflecting mirror (the *beam-splitter)* able to split the beam into two components. The so separate radiation is reflected back, independently, by the two plane mirrors, and reaching the beam splitter, is recombined into a single beam. Since the optical paths are different, when the two components recompose create an interference pattern; this is achieved by varying in a continuous manner the position of the movable mirror so that the path difference (*optical path difference, OPD*) also varies. This obtains an interferogram, which shows the intensity of the radiation as a function of the OPD. The optical path difference is measured by the monochromatic radiation (λ= 632.8 nm) emitted by a He-Ne laser, which follows the same path of the infrared beam. The recombined beam reaches

another parabolic mirror, which focuses it on the sample's location. In the case of biconical reflectance measurements, an optical accessory is placed in the sample position. This accessory, sketched in Fig 2.5, is composed of two ellipsoidal (M3 and M4) and four plane mirrors (M1, M2, M5, M6).

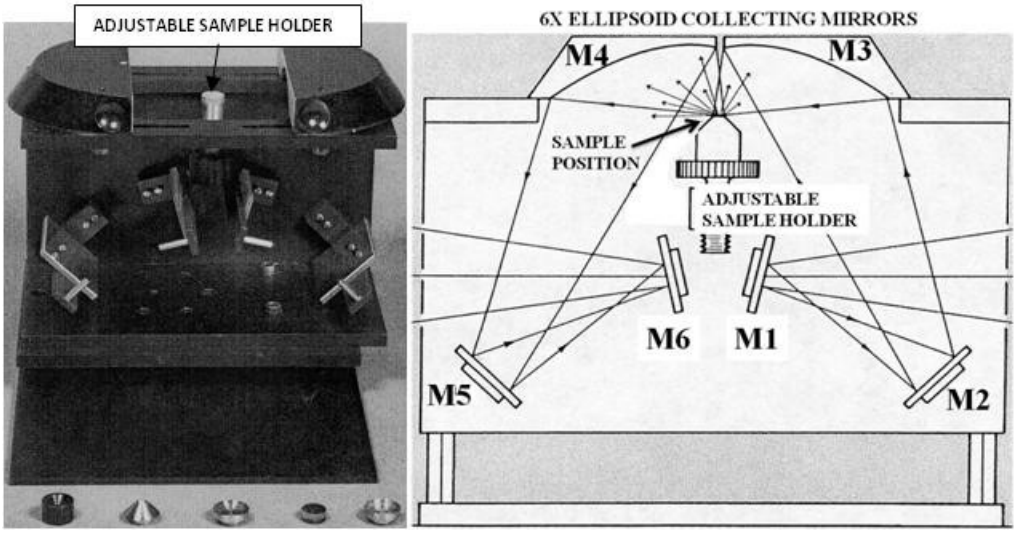


*Fig. 2.5 – The reflectance device. On the left the position of the sample is indicated and in the bottom, from right, the sample holder, the aluminum mirror, and other equipments for the powder's spectra are presented. On the right a schematic view of this device is reported.*

The radiation, coming from the parabolic mirror of the spectrometer, is reflected by M1 and M2 mirrors towards the ellipsoid mirror M3 that focus the radiation on the sample. The radiation is then diffused by the sample and collected again by the M4 mirror and sent to the detector, thanks to the M5 and M6 mirrors.

The detector is a *deuterated triglycine sulphate* (DTGS) element, it is a thermal detector based on the pyroelectric effect operating at room temperature. The radiation absorbed by the pyroelectric crystal, internal to the detector, increases its temperature and causes a change in the electrical polarization of its crystal lattice, proportional to the temperature difference obtained. Electrodes sensitive to the variation of the polarization allow to produce an electrical signal, which is the interferogram of the radiation. The electric signal obtained passes through a pre-amplifier to an amplifier, then to an analog-digital converter and, finally, to a processor which performs the *Fourier transform*, to transform the Intensity

versus OPD (interferogram) into intensity versus wavenumbers and thus obtains the spectrum.

The spectral resolution that is, in a spectrum, the smallest distance at which two different peaks are still distinguishable, is:

$$0.5/OPD_{max} \qquad \text{(Eq. 2.1)}$$

and depends inversely on the optical path difference given by the interferometer.

All the spectra reported in this work have a resolution of 1 $cm^{-1}$, then the maximum optical path difference of the two beams in the interferometer is 0.5 cm.

In order to disentangle the absorption bands due to the substrate, to the optics of the spectrometer and to the air interposed to them, and to take into account the wavelength dependent response of the spectrometer plus detector system, each spectrum is divided by the blank background spectrum, that is the one revealed by the instrument by using a reflectance standard as sample. Dividing the spectrum of the radiation reflected by the sample to that of the background taken with the reflectivity standard, it is possible to obtain the reflectivity of the sample. The quality of the spectra is improved by sending to the spectrometer, via a dryer compressor always turned on, a flux of dry and $CO_2$ purified air reducing, in this way, the amount of moisture and carbon dioxide that the IR beam cross along its optical path.

An analytical description of the spectra's acquisition technique will be presented below.

The background is acquired with an aluminum mirror whose position is regulated, upward or downward, with a screw until the infrared signal is maximum i.e. its surface is in the focus position of the elliptical mirror. The instrument is so aligned.

Before acquiring the background spectrum it is important to maintain the surrounding conditions as uniform as possible, in terms of presence of gaseous carbon dioxide and water vapor. To obtain this, as will be shown below, several tries have been repeated.

After opening the door of the sample's housing for the alignment, we maintained it closed for a fixed time interval. Before acquiring the background we always waited for 10 minutes, while for the samples (after the alignment) we chose to maintain the door closed for 5, 10, 15 minutes, during which we acquired three different spectra. We repeated this procedure for each sample, and we acquired a new background every two samples analyzed.

The spectra obtained in the three time intervals, using the described procedure, are presented in Fig. 2.6 for the AF4 sample.

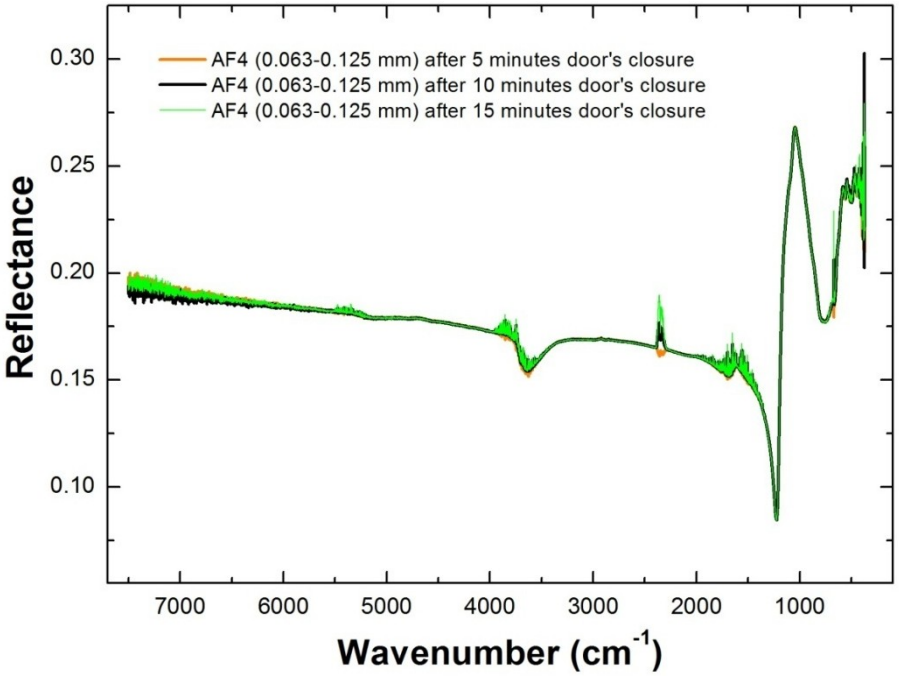


*Fig. 2.6– The test spectra obtained, for the AF4 sample, during the indicated three ranges of time.*

Looking at Fig. 2.6, we noticed the presence of some peaks around 3300 $cm^{-1}$, 1660 $cm^{-1}$, 2343 $cm^{-1}$ attributable to the OH stretching and bending of $H_2O$ and to the C=O stretching of $CO_2$, respectively.

The intensity of these peaks increased with the increasing closing time. This means that, over time, the $H_2O$ and $CO_2$ content inside the spectrometer were decreasing as expected due to the dry air purging action. With the aim to correct the spectra from the $H_2O$ and $CO_2$ features, a member of our team created a routine with the IDL program. In particular by taking the ratios of the spectra acquired at different time on the same sample, the absorption spectra of atmospheric water vapor and $CO_2$ is obtained. The $CO_2$ and water vapor features are then subtracted separately from the spectrum by a suitable amount determined by an iterative procedure. One result of this correction is shown in Fig. 2.7.

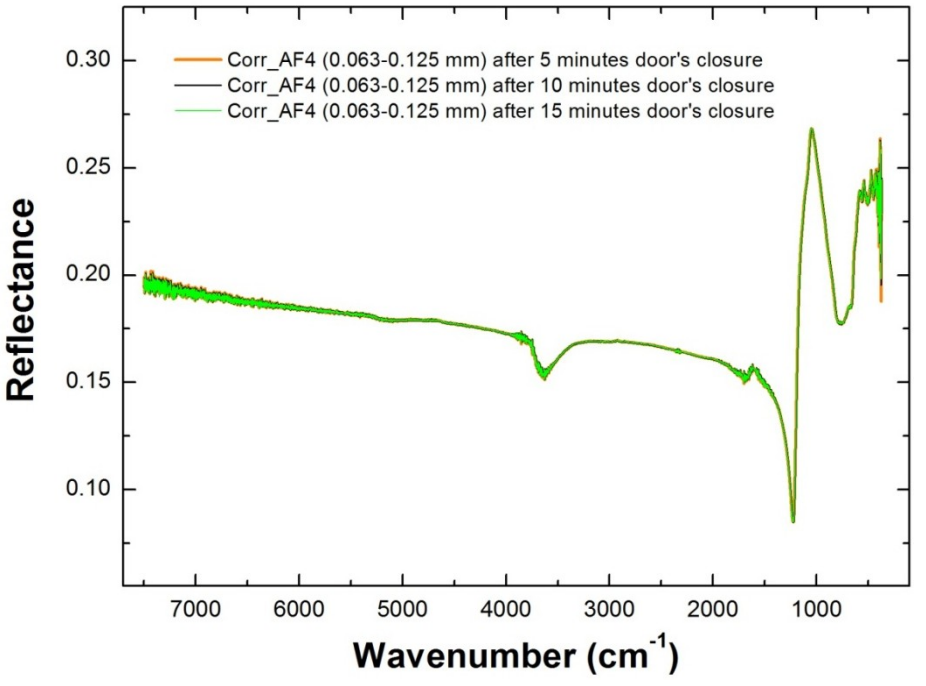


*Fig. 2.7 – Spectra corrections from $H_2O$ and $CO_2$ absorption features.*

## Section B: UV-Vis NIR spectrophotometer and data

The UV-Vis-NIR spectra of the LASp's samples are acquired with the Perkin Elmer Lambda 19, the spectrophotometer operating in the 200-2500 nm spectral region, with a speed of 120 nm/min, a scan of 1 nm and a slit of 2 nm (that is also the resolution).

After the instrument initialization, the spectrum of the background is acquired positioning a diffuse reflectance standard (barium sulfate), in the integrating sphere aperture. The diffuse radiation (that is about 90% for the barium sulfate) collected by the integrating sphere is detected by two different detectors for the UV-Vis and for the NIR. For reflectance measurements, every other spectrum of the materials is acquired substituting the barium sulfate with the sample in the same aperture (with a brass ring sample holder, to better sustain the pellet) and using the background as a reference. It is also possible to obtain the specular radiation reflected from the sample, positioning in front of it a *light trap*, that is a

sort of black box which avoid that the specular radiation is detected within the integrating sphere and permit to make comparative measurements between diffused and reflected radiation. In particular the specular component can be obtained by subtracting the diffuse component (acquired with the trap) from the total diffuse plus specular reflectance (acquired without the trap). When the surface is perfectly reflecting, the reflectance of the spectrum acquired with the light trap is, in fact, near zero. An example of this case is reported in Fig. 2.8, where the sample utilized is a silicate film on a silicon wafer, as will be described in § 2.3.

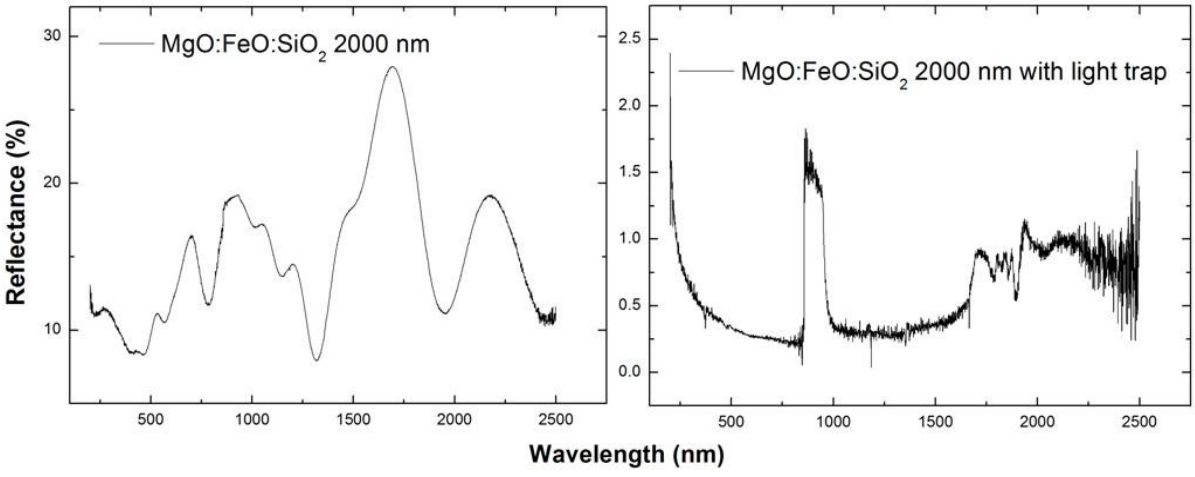


*Fig. 2.8.– A comparison between the spectra acquired without or with light trap for the silicate sample deposited on a polished silicon wafer. It is clear that the diffuse reflectance of the spectrum acquired with the light trap is near zero.*

The samples mostly used (the etnean palagonites, see also § 2.3) present a scattering rough surface, so the reflectance of their spectra with and without light trap are almost the same (as it is shown, for one example, in Fig. 2.9), then for these samples always the spectra without light trap will be presented.

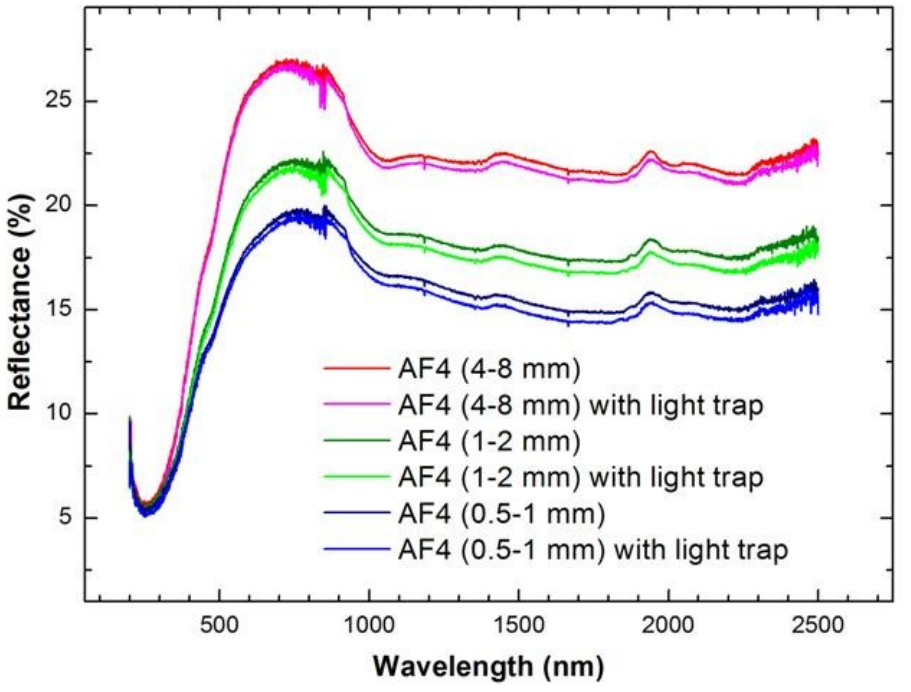


*Fig. 2.9 – A comparison between the spectra acquired without or with light trap, for the AF4 etnean sample. The spectra are almost the same.*

Leaving to the next chapter the detailed description of the spectral characteristics, we note that the spectra in Fig. 2.9 evidence the presence of the well known two peaks around 1450 and 1950 nm, which are due to the OH-absorption features. To verify that these peaks are due to the presence of water adsorbed on the integrating sphere walls and on the barium sulfate standard, and with the aim to subtract them, we use also a gold sample as reference.

We, then, acquired a new spectrum for the barium sulfate and another one for a gold optically thick layer deposited on quartz.

In Fig. 2.10 (top) these spectra are presented and it can be noted soon how, with respect to the barium sulfate, the gold is highly reflecting (about 96%) from 800 to about 2500 nm, while the reflectance decreases abruptly to about 37% at 500 nm and till 29% at 200 nm.

In the spectrum with the barium sulfate the peaks at 1450 and 1950 nm are not evident, because the barium sulfate is the reference for the spectrometer; these absorption features are evident in the barium sulfate-gold ratio (see Fig. 2.10, top).

This result proofs how the OH absorption features are due to water trapped in the barium sulfate standard.

Because every spectrum (including the gold one) is acquired by the spectrometer with respect to the barium sulfate, to correct the spectra is enough to divide, point per point, the reflectance values of the sample's spectrum to those of the gold.

However, because the gold's reflectivity decreases at shorter wavelengths, the samples spectra will be divided by those of the gold only from 857 to 2500 nm, and will be maintained unaltered (i.e. divided by the barium sulfate), from 200 to 856 nm. Finally, spectra have been scaled dividing by an opportune factor, as shown in Fig. 2.10 (bottom) for the AF1 (1-2 mm) sample, to correct for the different reflectance of gold and barium sulfate at 857 nm.

In Fig. 2.10 (bottom) the sample spectrum not corrected shows the peaks around 1450 and 1950 nm. In the spectrum corrected with respect to the gold sample only these peaks disappear and it is evident the rapid change of the reflectance around 857 nm, due to the gold's reflectivity that significantly decreases below this wavelength. Finally, in the last correction (violet line), the two spectral regions (857-2500 nm and 200-856 nm) are rescaled.

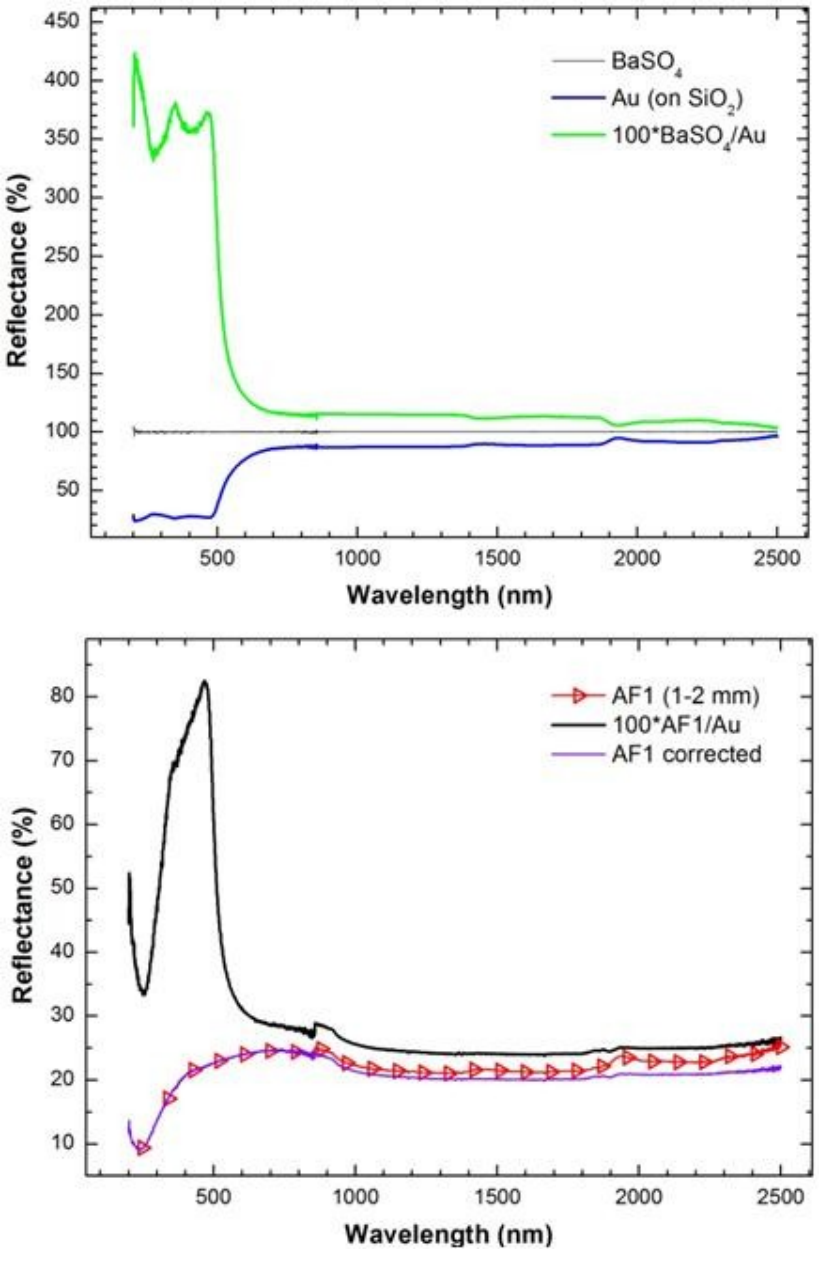


*Fig. 2.10 – The spectra corrections. (Top): the comparison between the barium sulphate spectrum and the gold one, used for the spectra corrections. (Bottom): the correction of the AF1 (1-2 mm) sample. The red line with triangles is the sample's spectrum not corrected; the black line is the correction with respect to the gold sample only; the violet line is the final corrected spectrum.*

This procedure has been applied to all the spectra of the 36 AF etnean samples prepared (see § 2.3) and also to the new erupted (09-02-2012) etnean sample in the crater of South-East (CSE sample) (see § 2.3).
As an example, the AF4 corrected spectrum is shown in Fig. 2.11.

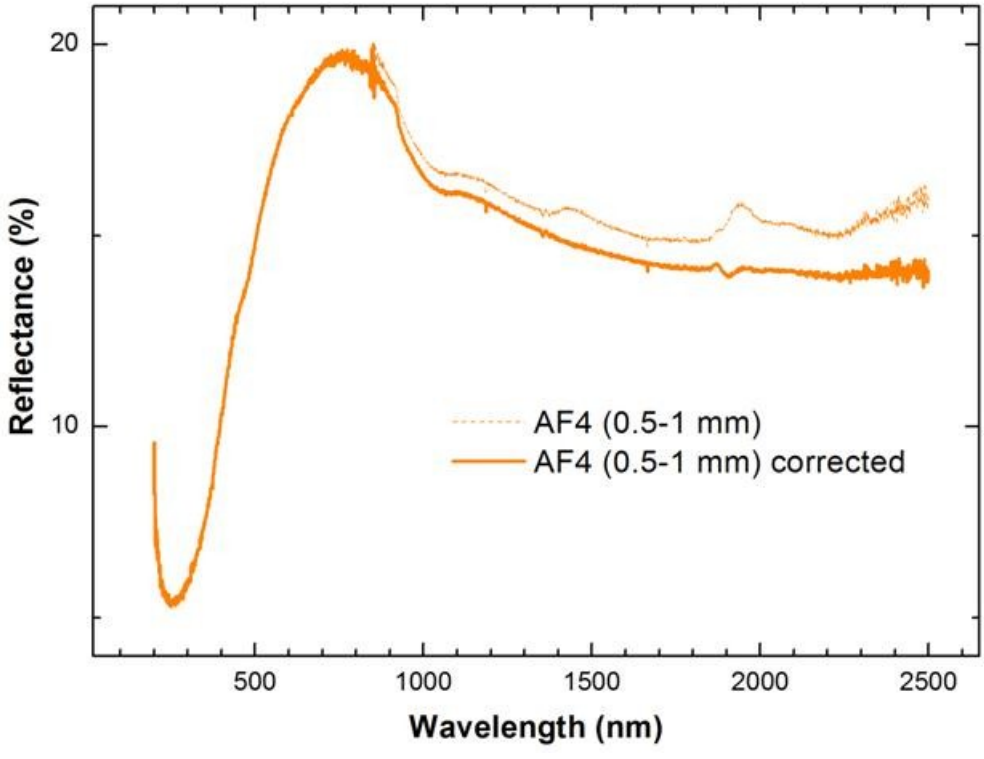


*Fig. 2.11 – A comparison of the spectra, corrected and not, for an AF4 specimen.*

## 2.2.3 The ion implanter

The ion implanter (*Danfysik*), connected to the analysis chamber, is capable of producing, selecting, and accelerating ions in a range of energies between 30 and 200 keV for singly ionized, up to 400 keV for doubly ionized, and send them, once collimated, to the target. The diagram, shown in Figure 2.12, presents the basic features.

Two main parts can be distinguished: a high-voltage area, placed in a shielded room, where ions are produced, selected and accelerated, and a region, with ground potential, where ions are collimated before striking the sample. The mechanism of operation is, in brief, the following: a heated tungsten filament generates, for thermionic effect, electrons; these are accelerated by a potential difference of 300 V between the filament and the anode and colliding with the atoms of a gaseous mixture (hydrogen and argon) placed inside a vacuum tube, ionize them. The ions produced are focused and accelerated by a potential difference adjustable up to 30 kV and subsequently selected, according to their charge/mass ratio, thanks to a static tunable magnetic field placed along their trajectory that deflect the ions by 90 degree. A further potential difference, variable up to 170 kV, determines a post-acceleration of the ions in the acceleration tube, up to an energy of 200 keV (or 400 keV in the case of double ionization). Reached the ground potential, the ion beam goes in a metal tube where they are focused by means of small plates at constant tunable voltages.

It is possible to obtain an uniform irradiation with the aid of periodic variables voltages applied to a second system of horizontal and vertical plates that allows scanning of the entire sample. At the end of the path a brass ring, whose area is equal to that of its hollow part, is connected to a micro-ammeter that measure the ion current, while an integrator of the current evaluates the overall charge and, therefore, the number of ions per $cm^2$ reaching the sample. The used currents are below 1 μA to avoid a macroscopic heating of the sample.

Each ion of the beam interacts elastically with the nuclei of the atoms in the sample, and inelastically with the electron clouds, giving to the sample energy and causing phenomena such as *sputtering* (surface erosion), the amorphization of the crystal structure, and physic-chemical changes that can induce the formation of new molecular species (Strazzulla et al., 2001).

The penetration depth (or range) of the ion beam within the target depends on the mass of the ion and its energy.

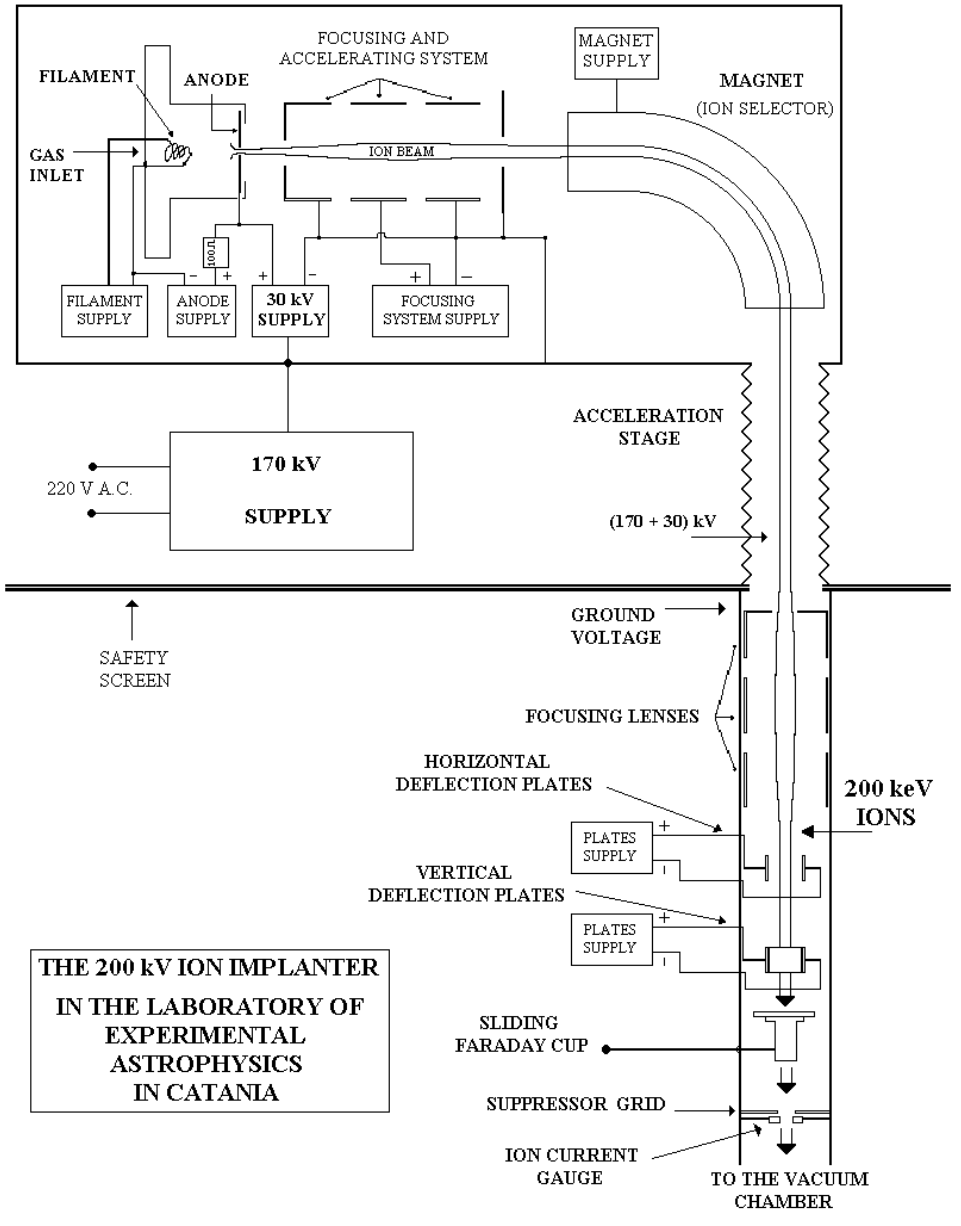


*Fig. 2.12– Schematic of the ion implanter.*

# 2.3 Materials and experimental procedure

Laboratory spectra allow us to observe the changes in the spectral reflectance of materials, mimic the surfaces of airless solar system bodies bombarded by different ions: very often the spectral reflectance relatively increases with wavelength (*reddening*), while degrading the absorption features and decreasing the overall reflectivity (*darkening*) (Baratta et al., 2011). Several materials have been investigated in our laboratory; here the results relative to silicates of interest for the study of the space weathering on Mercury surface are presented.
As already shown, reflectance spectra of Mercury's surface indicate the presence of highly weathered silicates (Na, K, Ca rich pyroxenes and tectosilicates).
In this work the spectral behavior of several Mercury analogue materials will be treated, before and after irradiation with 200 keV ions, and compared with recent observations, as will be presented in the next section and in Chapter 4.

## 2.3.1 Etnean samples

Five specimens (four pyroclasts and an ancient paleosoil, 5420-2370 years B.P.) of volcanic soil from Mount Etna have been studied. They are named AF1, AF2, AF3, AF5 and AF4 respectively, (described in Buemi et al., 1998) and are collected at different altitudes (as shown in the sketch of Fig. 2.13).
Reporting the analyses made in Buemi et al. (1998), the soil consists of black and red-orange particles and free crystals (30-35%, as plagioclase, clinopyroxene, olivine, Ti-magnetite and rare amphibole, in order of abundance). Black particles contain dark glass (65-70%, usually surrounding the free crystals) and microphenocrystals of the above mentioned minerals, whereas red-orange particles include mostly altered (palagonitic) glass. The oxides occur as *spinels* ($A^{2+}B_2^{3+}O_4^{2-}$) and there are also some oxides whose composition is near the limit of pure magnetite (FeO). In the oxides typical structures are observed and associated with oxidative weathering classified as either *trellis*, *composite*, or *sandwich* types. The trellis type structure is characterized by ilmenite lamellae (whose abundance increases with increasing oxidation) located along privileged planes (cracks, silicate inclusions, etc.), while composite and sandwich types can be the result of either oxidation or primary crystallization from the melt. Ilmenite intergrowths in the oxides of these samples

usually show trellis and sometimes sandwich type structure. The etnean soils examined are presumed to fall under the classification of *palagonite*, that is a class of amorphous to poorly crystalline weathering products resulting from basalt-$H_2O$ interaction (Buemi et al.1998, and references therein).

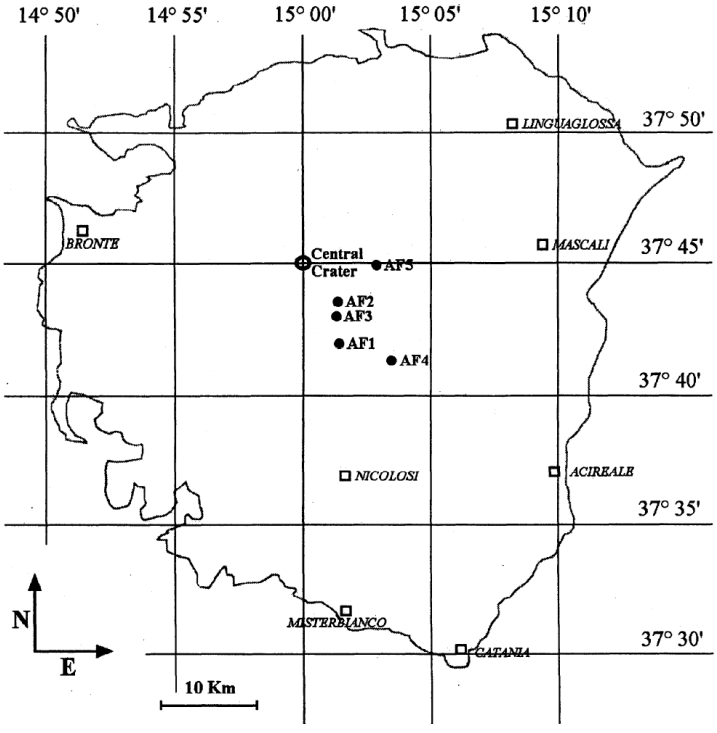


*Fig. 2.13 – Mount Etna map, showing AF sample locations.*

The results of a mean chemical analysis of AF sample glasses are presented in Table 2.1 (also taken from Buemi et al., 1998). This analysis was obtained by energy dispersive X-ray microanalysis (EDX).

*Table. 2.1– Glass analyses for AF samples made with EDX (from Buemi et al., 1998).*

| | AF1 | AF2 | AF3 | AF4 | AF5 |
|---|---|---|---|---|---|
| $SiO_2$ | 48.12 | 48.01 | 47.42 | 54.43 | 48.14 |
| $TiO_2$ | 2.27 | 2.13 | 2.12 | 1.64 | 2.20 |
| $Al_2O_3$ | 15.25 | 15.60 | 16.10 | 16.22 | 15.77 |
| FeO | 10.84 | 10.80 | 10.12 | 6.62 | 10.78 |
| MnO | 0.19 | 0.24 | 0.14 | 0.05 | 0.15 |
| MgO | 3.26 | 3.68 | 3.34 | 2.37 | 3.50 |
| CaO | 6.62 | 7.32 | 7.10 | 4.61 | 7.10 |
| $Na_2O$ | 3.72 | 4.95 | 3.45 | 3.96 | 3.84 |
| $K_2O$ | 2.45 | 2.87 | 2.57 | 2.66 | 2.63 |
| $P_2O_5$ | 0.85 | 0.79 | 0.78 | 0.44 | 0.95 |
| Cl | 0.27 | 0.23 | 0.21 | 0.34 | 0.19 |
| Total | 93.84 | 96.62 | 93.35 | 93.34 | 95.25 |

In weight percent.

Buemi et al. (1998) used these palagonite samples in order to obtain granulometric separates ranging from 8 to 0.032 mm). The rock sizes here considered are in intervals of: > 8 mm, 8-4 mm, 4-2 mm, together with the sieved ones, in intervals of: 2-1 mm, 1-0.5 mm, 0.5-0.25 mm, 0.25-0.125 mm, 0.125-0.063 mm, 0.063-0.032 mm and < 0.032 mm.
These ranges of particle sizes, for the different samples utilized, are sketched in Tab. 2.2.

*Table. 2.2– A scheme of the particle sizes for the different etnean samples utilized.*

| | ≥8 | 8-4 | 4-2 | 2-1 | 1-0.5 | 0.5-0.25 | 0.25-0.125 | 0.125-0.063 | 0.063-0.032 | <0.032 |
|---|---|---|---|---|---|---|---|---|---|---|
| AF1 | ● | ● | ● | ● | ● | ● | ● | | ● | |
| AF2 | ● | ● | ● | ● | ● | ● | ● | | | ● |
| AF3 | | ● | ● | ● | ● | ● | ● | ● | | |
| AF4 | ● | ● | ● | ● | ● | | | ● | | |
| AF5 | ● | ● | ● | ● | ● | ● | | ● | | |

To perform samples suitable to our instrumentations, has been prepared two layers-*pellets* made of powdered rocks on a KBr substrate.
About 500 mg of KBr are used for the substrate, positioned in a 13 mm in diameter cylindrical sample holder, and exposed to a pressure of approximately 8-10 tons for 1 $cm^2$ in

a time range lasting from 2 to 5 minutes. An image of the press and the sample holder is represented in Fig. 2.15.

The five multisized specimens were, at first, grinded with an agate mortar and then powdered with a vibrator "*Specamill*" (as shown in Fig. 2.14). The vibrator comprise a stainless steel hollow cylinder and two small (about 3 mm in diameter) spheres of the same material.

Inside the cylinder the grinded rock is inserted; this will be shacked, together with the balls, with a vibration frequency of 50 Hz for about 5-15 minutes, in order to obtain fine powder (see also Fig. 2.14).

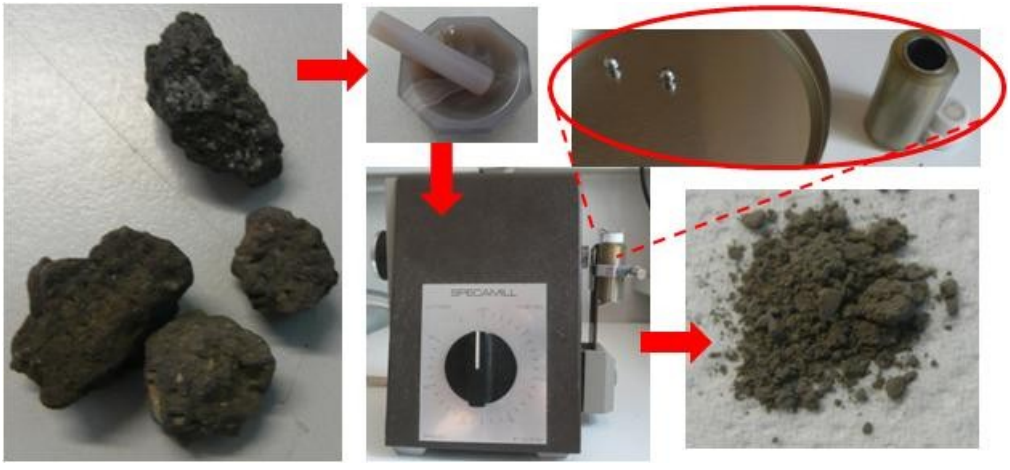

*Fig. 2.14 – The two-step path of powdering the rocks, with the agate mortar and the vibrator.*

About 30-50 mg of this powdered rock is then layered in the cylindrical sample holder, upon the KBr pellet, and exposed to the same pressure of its substrate. A scheme of the used method is shown in Fig. 2.15.


*Fig. 2.15 – The cylindrical sample holder and the press used to prepare sample's pellets.*

With this same procedure 36 pellets of the five etnean specimens, with the different original grain sizes above specified (Table 2.2) have been prepared, and the same number of reflectance spectra in the Ultraviolet-Visible and Near Infrared (UV-Vis-NIR) and infrared (IR) spectral regions have been acquired, as will be shown in the next chapter.

Despite the fact that every pellet is prepared with very fine powdered rock, several spectra are acquired from the same sample which was sieved at different grain sizes.

The reason for this repetition is because the roughest rock separates seem to show, at a first look, materials of different colors (for example, more or less red) and, according to the size, could then contain different materials, or give information about the inner part of the rock.

Finally, because the AF samples were all old enough to be altered by atmospheric events, we looked for a new rock, as young as possible, to make comparative measurements with the others.

The new rock was studied in our laboratory, thanks to the courtesy of the *Istituto Nazionale di Geofisica e Vulcanologia* (*INGV*).

It was collected at the Etna volcano, on February 9$^{th}$ 2012 soon after an eruption, and named CSE, as for Crater of South-East. It was prepared with crushed and sieved rocks < 1 mm in size.

All the spectra acquired from our samples will be analyzed and discussed in the next chapter.

## 2.3.2 Other silicate materials

We had the opportunity to analyze another group of silicates elsewhere prepared with silicon wafers coated with silicate films of different thickness. These films have been deposited, in an $O_2$ atmosphere, with a deposition pressure ranging from $10^{-6}$ to$10^{-4}$ mbar.
In particular, they were:

- $SiO_2$, having a film thickness of 1000 and 2000 nm
- Nepheline (1000 nm)
- MgO:FeO:$SiO_2$ (500 and 2000 nm)
- Forsterite mineral (1000 nm)
- Fayalite mineral (1000 nm).

Reflectance (and also transmittance) UV-Vis-NIR and IR spectra of these materials have been acquired and will be shown in Chapter 3.
An additional set of silicates studied is listed in Table 2.3:

*Table. 2.3 – A list of some Mercury analogue minerals.*

| MINERAL | FORMULA |
|---|---|
| Forsterite (olivine) | $Mg_2SiO_4$ |
| Jadeite (pyroxene) | $NaAlSi_2O_6$ |
| Sodalite (tectosilicate) | $Na_8Al_6Si_6O_{24}Cl_2$ |
| Nepheline (tectosilicate) | $(Na, K)AlSiO_4$ |

UV-Vis-IR reflectance and Raman spectra of these Mercury's candidate silicates, before and after ion irradiation with 200 keV $Ar^+$, and a fluence of $1 \cdot 10^{17}$ $cm^{-2}$ are acquired.
Diffuse reflectance spectra for three of these samples will be shown and analyzed in the next chapter.

# CHAPTER 3

# LABORATORY SPECTRA OF MERCURY ANALOG MATERIALS

In an attempt to verify if the selected rocks (described in Chapter 2) can be suitable for Mercury surface, several spectra in the UV-Vis-NIR and IR spectral regions have been acquired. Some samples have also been irradiated with 200 keV $H^+$ or $Ar^+$, and the resulting spectra have been here analyzed.

## 3.1 UV-Vis-NIR reflectance spectra of Etnean basalts

The spectra of the 36 samples prepared from powdered rocks having different original particle sizes (as described in Table 2.2), after being corrected by the OH-features (§2.2.2, sect. B), are here analyzed in detail. In the following Figures (3.1, 3.2, 3.3, 3.4 and 3.5) the

UV-Vis-NIR reflectance spectra for the five AF specimens of different original particle sizes are presented.

After preparation the grain size in all the samples is similar. Hence the difference in reflectance spectra may reflect different composition and/or alteration. Hereafter we'll talk about *size* meaning the original sieved size, i.e. that before powdering.

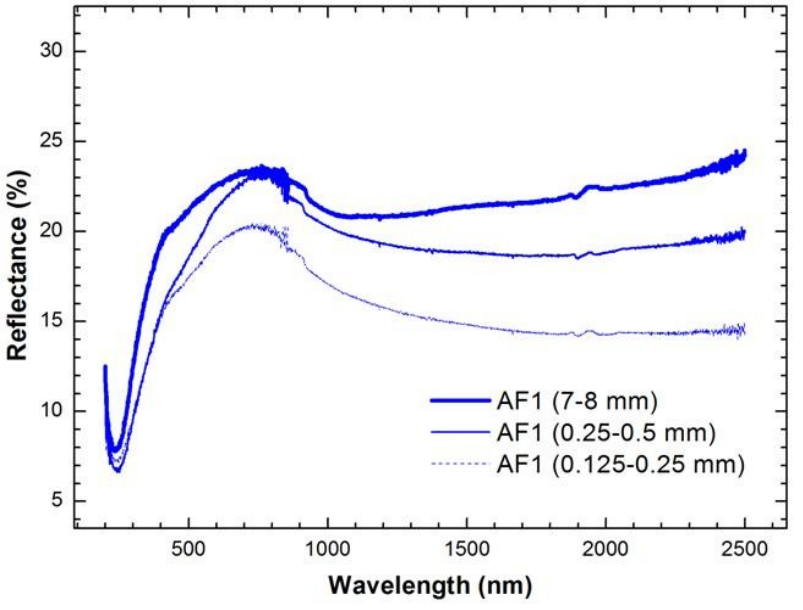


*Fig. 3.1 – A comparison among the reflectance spectra of AF1 samples of different original particle size.*

As also described in Buemi et al. (1998), in Fig. 3.1 it is seen that spectra exhibit the portion of the Fe absorption feature at 300-600 nm, but lack the features at 600 and 900 nm, which commonly occur in well-crystallized iron-bearing phases.

The spectra also show that the slope sign changes several times varying the wavelength.

Furthermore, despite the accurate procedure used to avoid OH contamination in the spectrophotometer, it can be noticed in Fig. 3.1 that the AF1 sample presents some features around 1950 nm, which can be attributed to OH absorption. This evidences that the water feature, due to the trapped water molecules into the wall of the integrating sphere and in the $BaSO_4$ standard, is not completely removed by the correction procedure.

In addition, by comparing the spectra of the AF1 sample with different particle size it seems evident that, with decreasing the original particle size, the reflectance is reduced and it is possible to note an absorption around 550 nm, and a bump around 750 nm. At wavelengths greater than 1000 nm the reflectivity increases with the wavelength for samples of greater size, while decreases at the beginning and then remains approximately constant, for those of smaller sizes.

A similar analysis is presented in Fig. 3.2 for AF2 samples, with different original particle size.

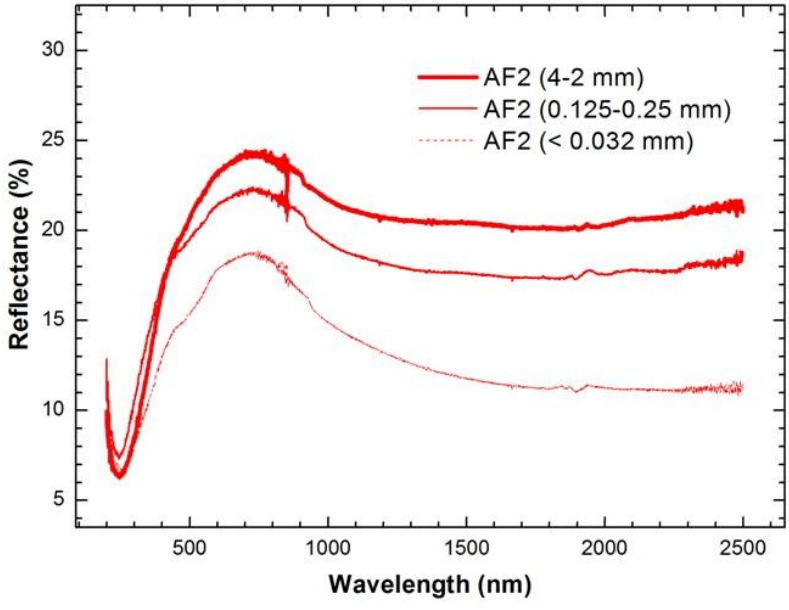


*Fig. 3.2 – A comparison among the reflectance spectra of AF2 samples of different original particle size.*

Looking at Fig. 3.2 it can be seen, also in this case, the presence of the Fe-absorption feature (300-600 nm) and the reflectivity that decreases with decreasing original particle size; the depression around 500 nm and the bump around 750 nm become more evident. At wavelengths greater than 1000 nm the reflectivity is nearly constant for the samples with the largest and intermediate sizes, while decreases for the smaller one. Some small features around 1950 nm are noticed too.

The spectra of AF3 samples are shown in Fig. 3.3.

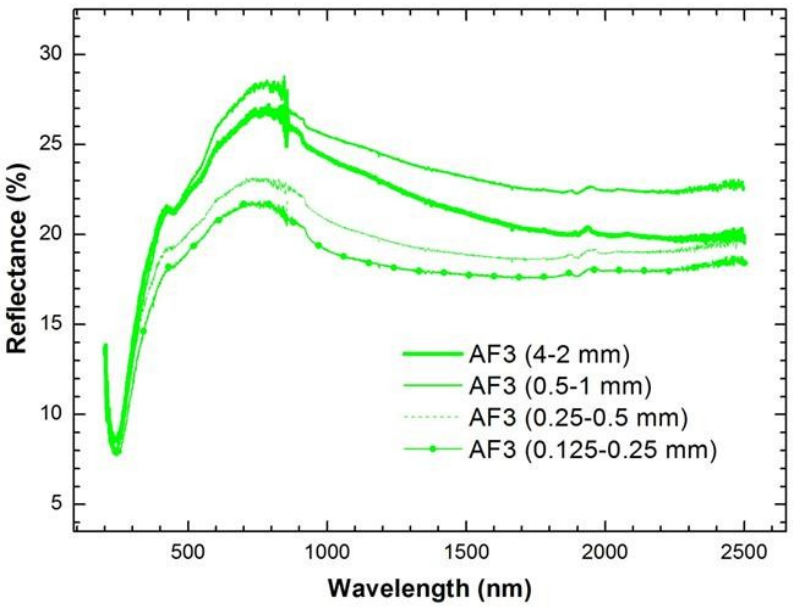


*Fig. 3.3– A comparison among the reflectance spectra of AF3 samples of different original particle size.*

In this case the large-sized sample presents a lower reflectivity with respect to that with the nearest lower size, and the reflectivity of the first one seems to decrease abruptly from 900 to 1900 nm. Apart from these differences, similar considerations made for the AF1 and AF2 spectra can be applied to the AF3 spectra.

The AF4 sample deserves special mention being the oldest of all the others and therefore the more exposed to the weathering agents. As it has been shown in Table 2.1, the mean chemical composition of glasses evidence a greater abundance of $SiO_2$ and a lower FeO and CaO content, with respect to the other AF samples. It seems likely that the spectra present differences with those of the other samples.

In Fig. 3.4 the spectra of AF4 samples with different original particle size are presented.

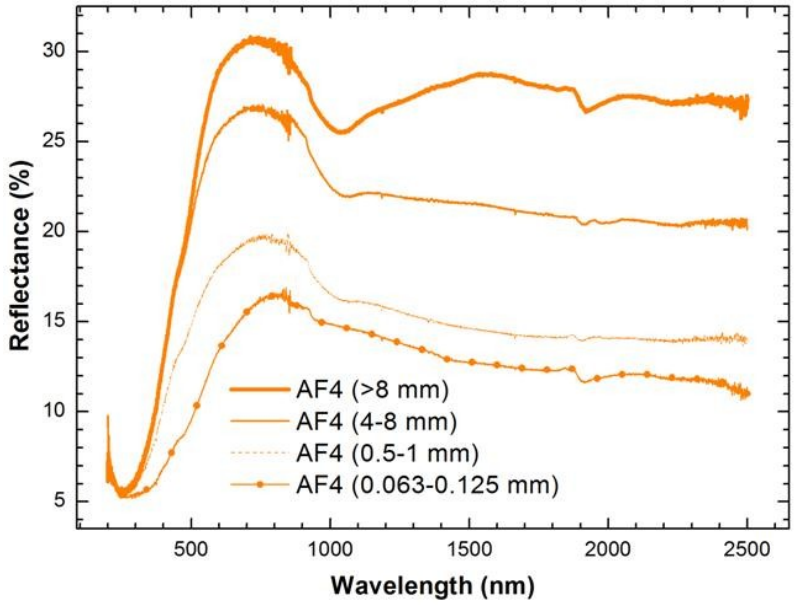


*Fig. 3.4 – A comparison among the reflectance spectra of AF4 samples of different original particle size.*

The spectra evidence a significant change in the reflectance values from the greatest size sample to the smallest one. The reflectance spectra in fact present a peak around 750 nm that is about 31% for the spectrum of the AF4 (> 8 mm) sample, and is reduced to about 17% for the smallest size sample spectrum. In comparison with the other three samples analyzed so far, it seems more evident the presence of a broad absorption feature near 1 μm, especially for the larger sizes. This feature is due to the presence of ferrous iron $Fe^{2+}$ in both olivine and pyroxene (Brunetto and Strazzulla, 2005).

Finally, the AF4 spectra present, more evident than the others, a noticeable absorption feature at 1950 nm, that was also found in Buemi et al. (1998). This is due to a significant presence of water in this more weathered sample.

For the AF5 spectra, presented in Fig. 3.5, it is evident a modest absorption at about 500 nm, for the sample with the smallest particle size. In the NIR region the reflectivity lightly increases for the sample with intermediate size, while decreases for the sample with the smallest size. The spectrum of this last sample evidences the presence of a feature around 2μm, which is attributed to pyroxene (Brunetto and Strazzulla, 2005), while for the other

two sizes, despite corrections, the spectra show a small band at 1950 nm, as for the previous samples.

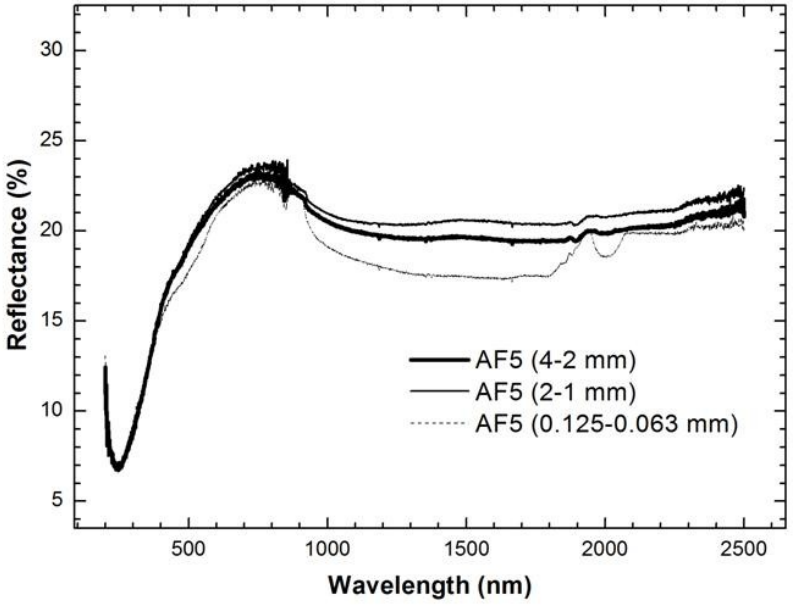


*Fig. 3.5 – A comparison among the reflectance spectra of the AF5 samples of different original particle size.*

In summary it appears clear that, in this spectral region, the reflectivity of all our samples decreases with decreasing the original particle size.

Almost all the samples present a small band at 1950 nm that, except for AF4 where it is strongest, is probably due to a not perfectly removed OH feature coming from the integrating sphere walls. The AF4 and AF5 samples seem to evidence some specific features around 1 μm (band I) and 2 μm (band II), attributable to $Fe^{2+}$ and pyroxene presences respectively. Nevertheless, the peak position of both band I and band II is known to shift to longer wavelengths with increasing $Fe^{2+}$ and $Ca^{2+}$ contents (Brunetto and Strazzulla, 2005 and references therein). The reflectivity variations in the 800-900 nm range are an experimental artifact due to the transition between the PbS and the photomultiplier detectors used for the NIR, and UV-Vis range respectively.

Because, as known from the literature and as will be shown in the next chapter, Mercury's reflectivity is quite low we decided to select and compare our spectra with the lowest reflectivity, which correspond to those with the smallest size.

In this comparison we have included a recently erupted etnean sample, named CSE, whose particle size is <1 mm.

The comparison is shown in Fig. 3.6.

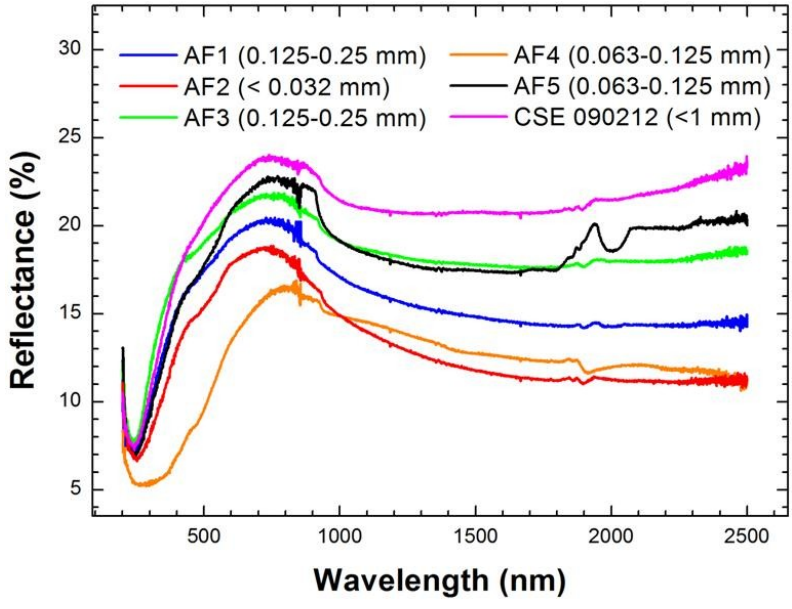


*Fig. 3.6 – A comparison among the reflectance spectra of the smallest-sized samples.*

Looking at Fig. 3.6, we see that all the samples with the smallest size present the Fe absorption feature at 300-600 nm (like the larger ones), a more marked depression of the reflectivity around 500 nm (not significant for the CSE sample) and a bump around 750 nm, that is shifted at about 800 nm for the AF4 sample.

In the UV-Vis region, the CSE, AF3 and AF5 spectra have a bit higher reflectivity, while the AF4 has a significant lower reflectivity. In the NIR spectral region, the CSE reflectivity is importantly higher than that of the others and increases with wavelength, while the AF2 one is the lowest after 1000 nm and decreases with increasing wavelength.

Finally, it has been verified that the CSE sample reflectivity roughly correspond to that of the large-sized AF samples. The unique difference is with respect to AF3 sample. In this case, in fact, the CSE reflectivity results almost coincident with that of the AF3 (0.25-0.5 mm) sample from the UV till 1000 nm, and increases a bit with wavelength after 1000 nm.

## 3.2 IR reflectance spectra of Etnean basalts

Laboratory IR reflectance spectra cannot be directly compared with those of Mercury that are, in the IR range, mostly due to thermal emission (Clark, 1979). We have however studied this spectral region with the aim to better know the characteristics of our samples.

A first check was to verify whether our samples were homogeneous, so different spectra have been acquired for each sample by varying the position of the pellet in the spectrophotometer.

Some spectra, acquired at different positions, are presented in Figs. 3.7 and 3.8.

In all the spectra it is evident at 1250 $cm^{-1}$ (8 μm) the Christiansen feature (CF), a reflectance minimum, that is a good compositional indicator. Recently Scollo et al. (2013) have studied the Christiansen feature in laboratory infrared spectra of volcanic ash particles erupted by Mount Etna in 2001 and have shown that the Christiansen feature at 1250 $cm^{-1}$ is consistent with the presence of basaltic glass.

We have also found that the spectra of the same sample acquired in different positions were not identical, sign of the non homogeneity of our samples.

In Fig. 3.7 there is evidence that only the spectra of the AF1 and AF3 samples with the smallest sizes (together with AF3, 4-8 mm) are almost the same: these samples are likely the most homogeneous.

In Fig. 3.8 we see that the AF4 and AF5 (small sized) and the CSE samples are quite homogeneous.

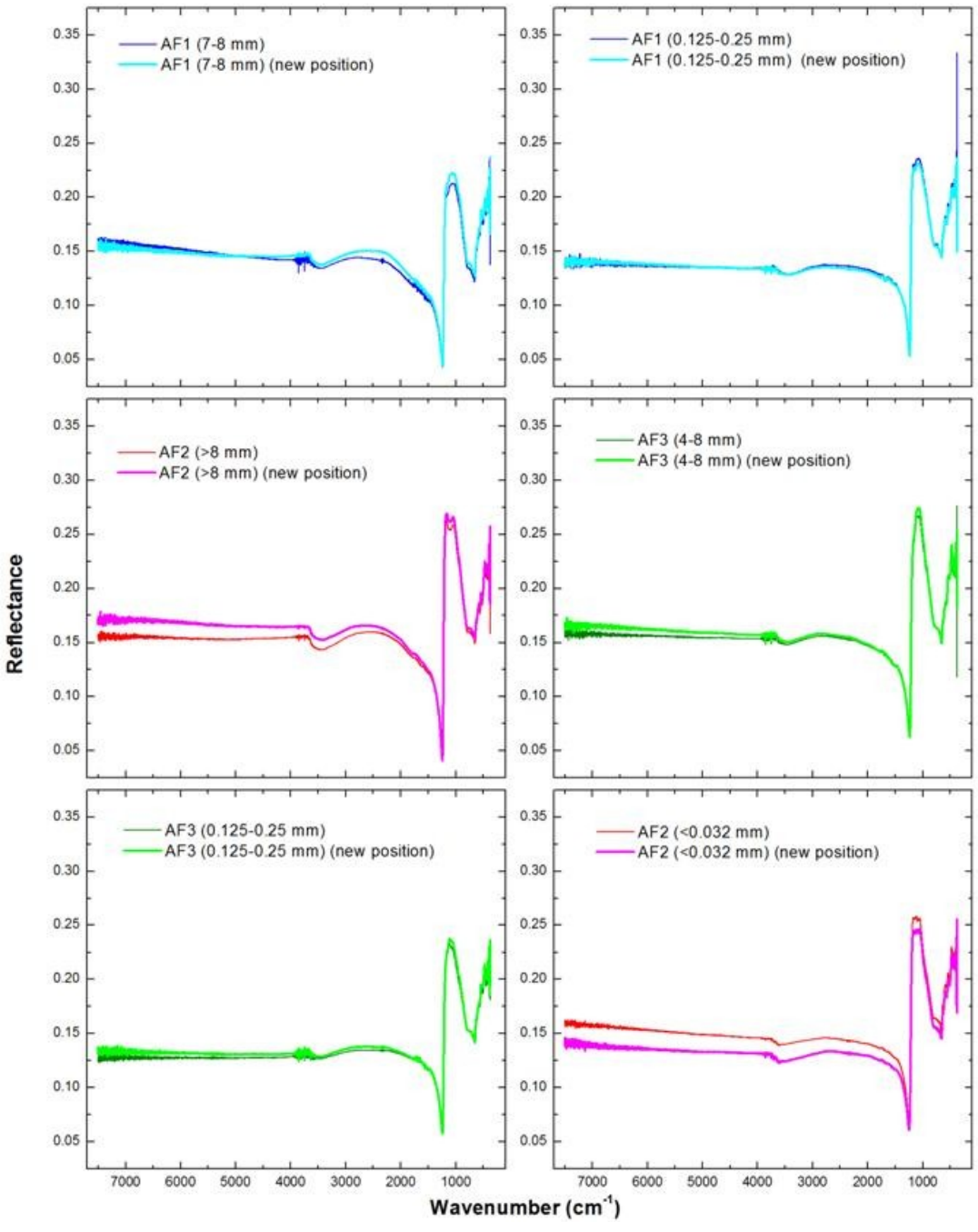


*Fig. 3.7 – A comparison between the spectra of the same sample acquired in different positions.*

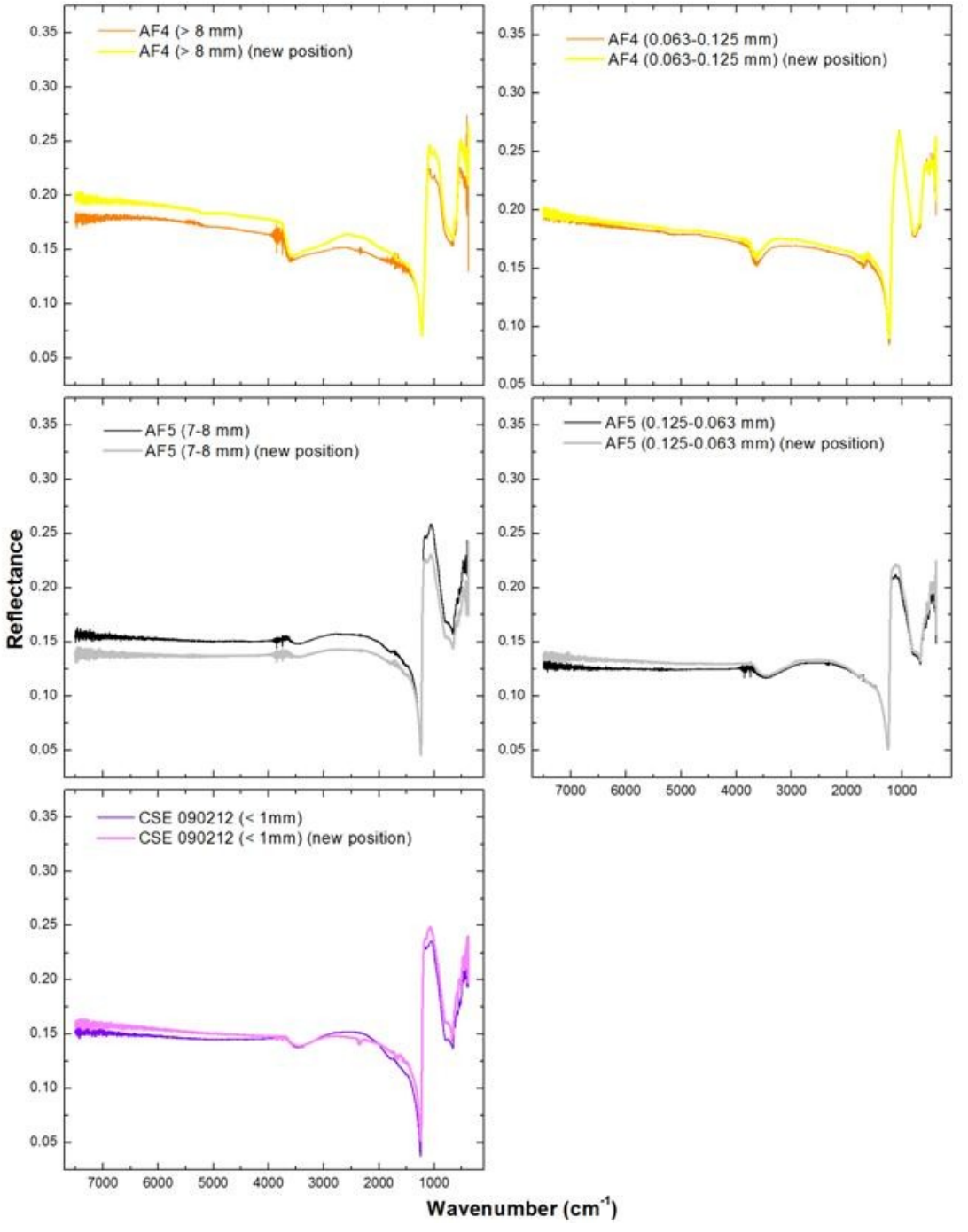


*Fig. 3.8 – A comparison between the spectra of the same sample acquired in different positions.*

Because the small variations in the reflectance values due to the non homogeneity of the samples could be confused with those produced by ion irradiation, we decided to irradiate only the most homogeneous samples, for which further spectra were acquired.

The results for two samples are shown in Fig. 3.9, where it can be noted how, changing the positions, there are not significant changes in the reflectance values.

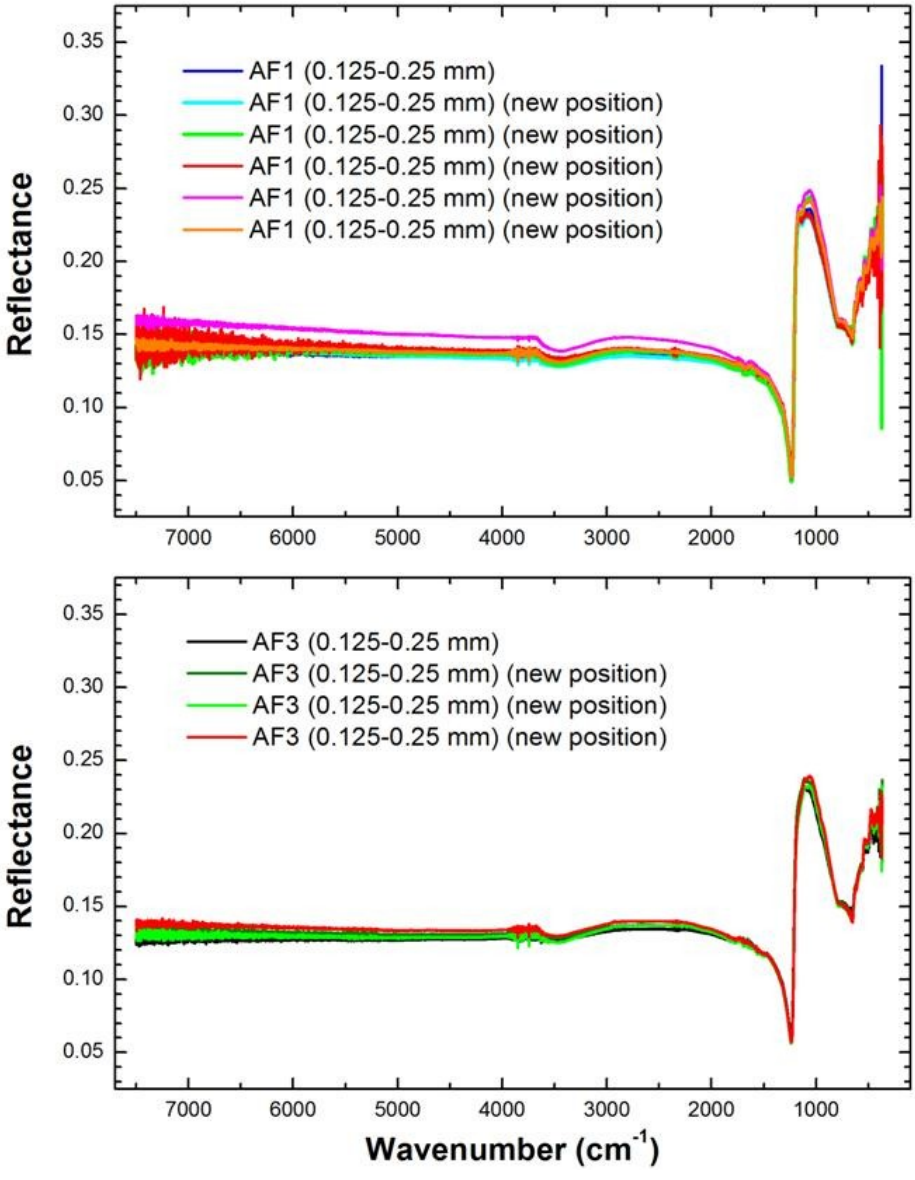


*Fig. 3.9 – Reflectance spectra acquired for two samples in different positions, in order to verify their homogeneity.*

# 3.3 Irradiated etnean samples

The chosen samples, i.e. AF1 (0.125-0.25 mm) and AF3 (0.125-0.25 mm), have been irradiated with 200 keV protons and argon ions.

The spectra of the unirradiated pellet compared with the irradiated one, for the considered samples, are presented in Figs. 3.10, 3.11, 3.12 and 3.13.

For each irradiation we recorded the integrated current (charge) that impinged on the sample (Coulomb) and then the fluence of the singly ionized ions (ions/cm$^2$).

In Fig. 3.10 the spectra before and after irradiation of the AF1 sample in the UV-Vis-NIR spectral region are shown. The AF1 sample was firstly irradiated with 200 keV $H^+$ and then with 200 keV $Ar^+$ ions to increase the effect of irradiation. In fact, fast ions penetrating a solid lose energy by elastic collision with target nuclei and by anelastic ionizations and excitations.

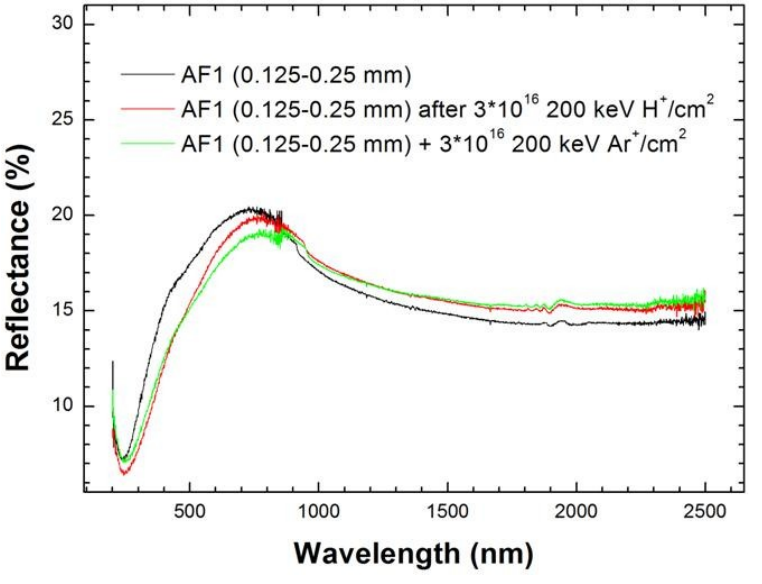


*Fig. 3.10– UV-Vis-NIR reflectance spectra of the AF1 small sized sample irradiated with $3\times10^{16}$ 200 keV $H^+/cm^2$ and then with $3\times10^{16}$ 200 keV $Ar^+/cm^2$. These irradiated spectra are compared with that of the unirradiated sample.*

In Fig.3.10 a modest reduction of the reflectivity can be observed after irradiation, that is a bit more marked after 200 keV $Ar^+$ in the 550-850 nm spectral region. In the NIR region the

reflectivity lightly increases after irradiation with $H^+$ and does not change after $Ar^+$ irradiation.

The effect of irradiation of the same AF1 sample, in the IR spectral region is reported in Fig. 3.11.

As seen in the NIR spectra, also in the MIR spectral region the reflectivity increases with irradiation.

Furthermore from Fig. 3.11, it can also be observed that the spectrum of the irradiated sample AF1, in the spectral region 3700-2800 $cm^{-1}$, evidences a decrease of the OH band, and the presence of CH bonds (2900-2800 $cm^{-1}$), that were absent in the spectrum of the unirradiated sample and that, was found, were due to organic contamination present on the reference standard.

The results obtained after AF3 irradiation with 200 keV protons, in the IR spectral region, are presented in Fig. 3.12.

Looking at the AF3 spectra in Fig. 3.12, it is evident that the reflectivity lightly decreases after irradiation, especially from about 4000 to about 500 $cm^{-1}$.

The comparison between the irradiated and unirradiated CSE sample is shown in Fig. 3.13.

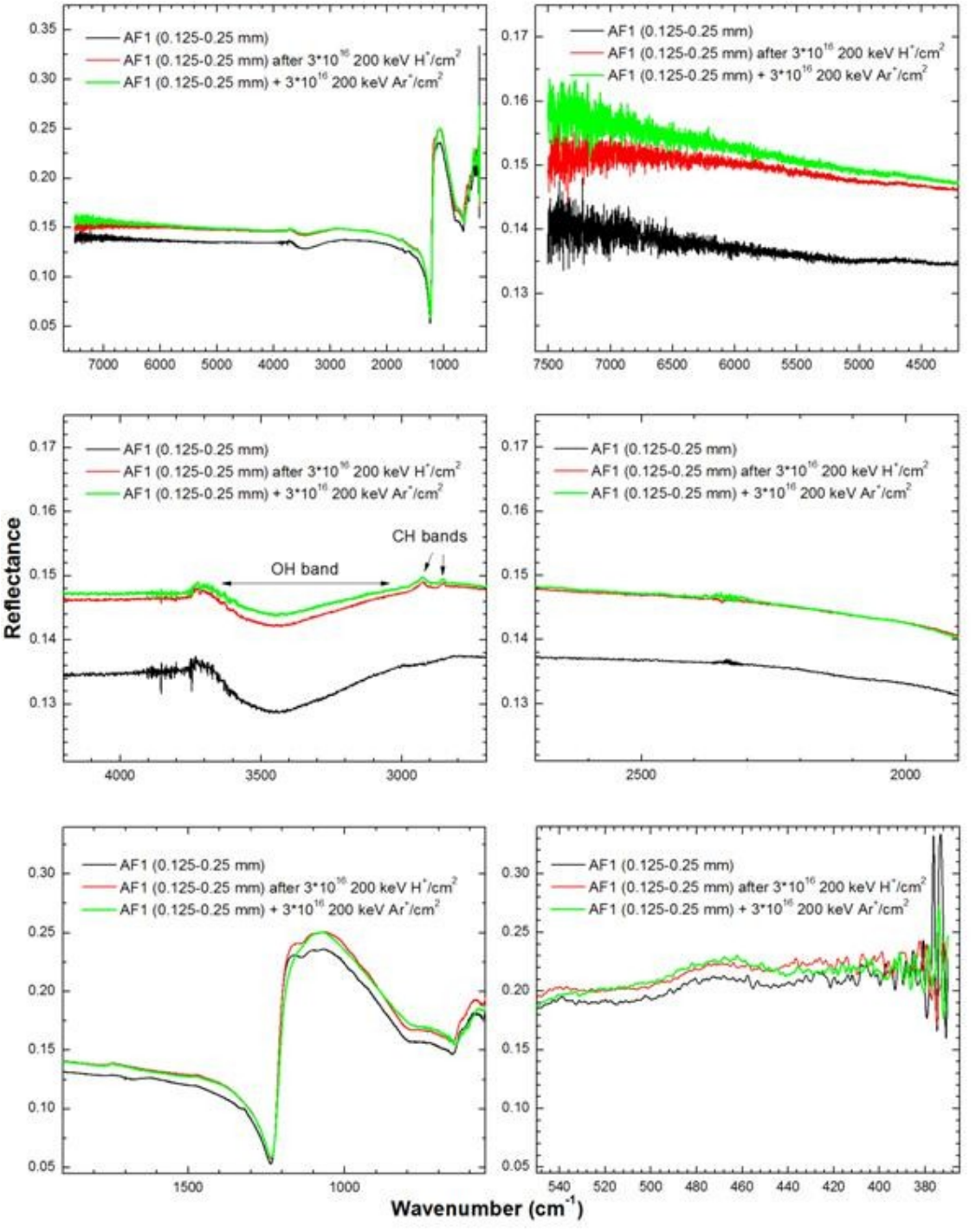


*Fig. 3.11–IR reflectance spectra of the AF1 sample irradiated with $3\times10^{16}$ 200 keV $H^+/cm^2$ and then with $3\times10^{16}$ 200 keV $Ar^+/cm^2$. These irradiated spectra are compared with that of the virgin sample.*

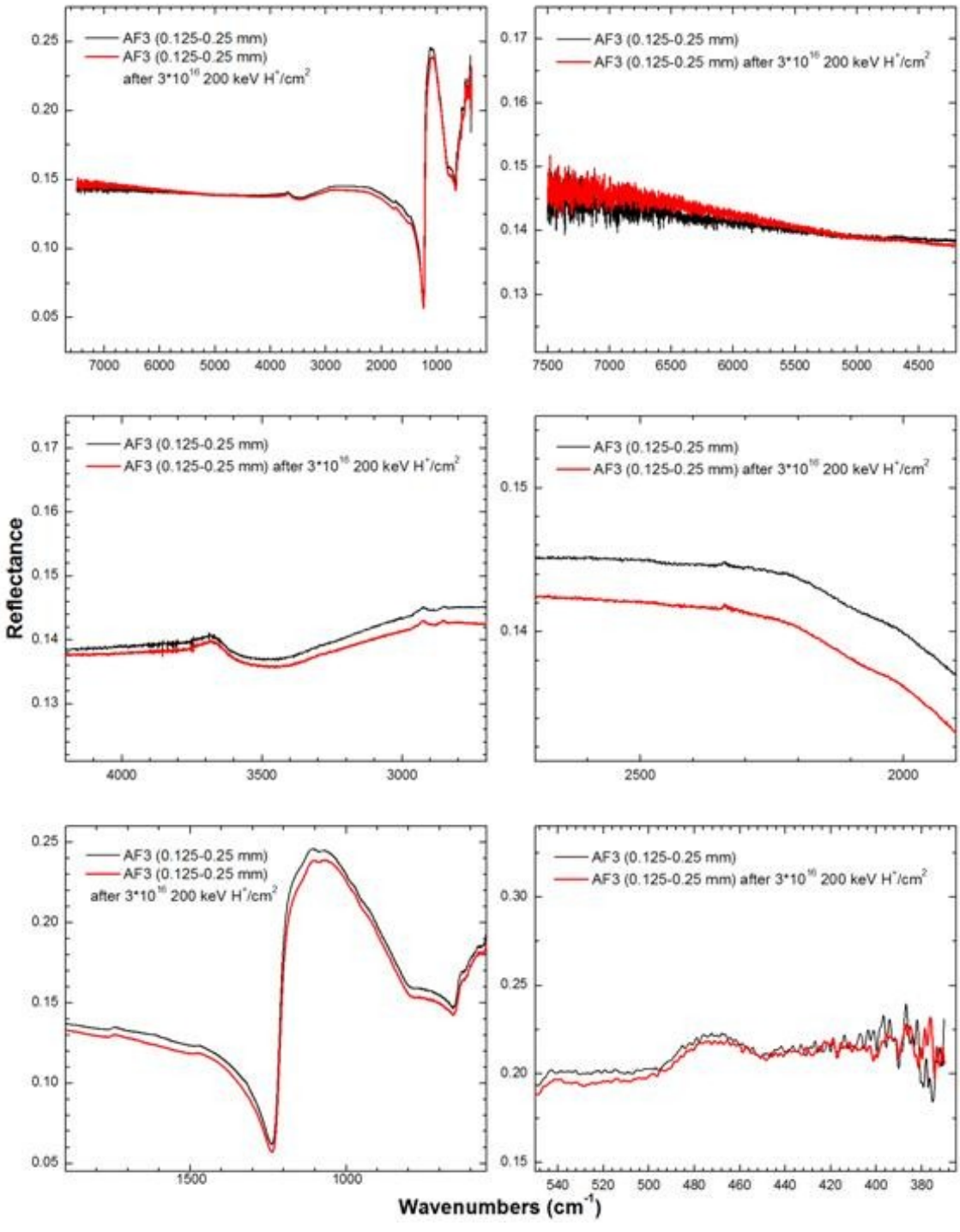


*Fig. 3.12– Reflectance spectrum of the AF3 sample irradiated with $3\times10^{16}$ 200 keV $H^+/cm^2$. This irradiated spectrum is compared with that of the unirradiated sample.*

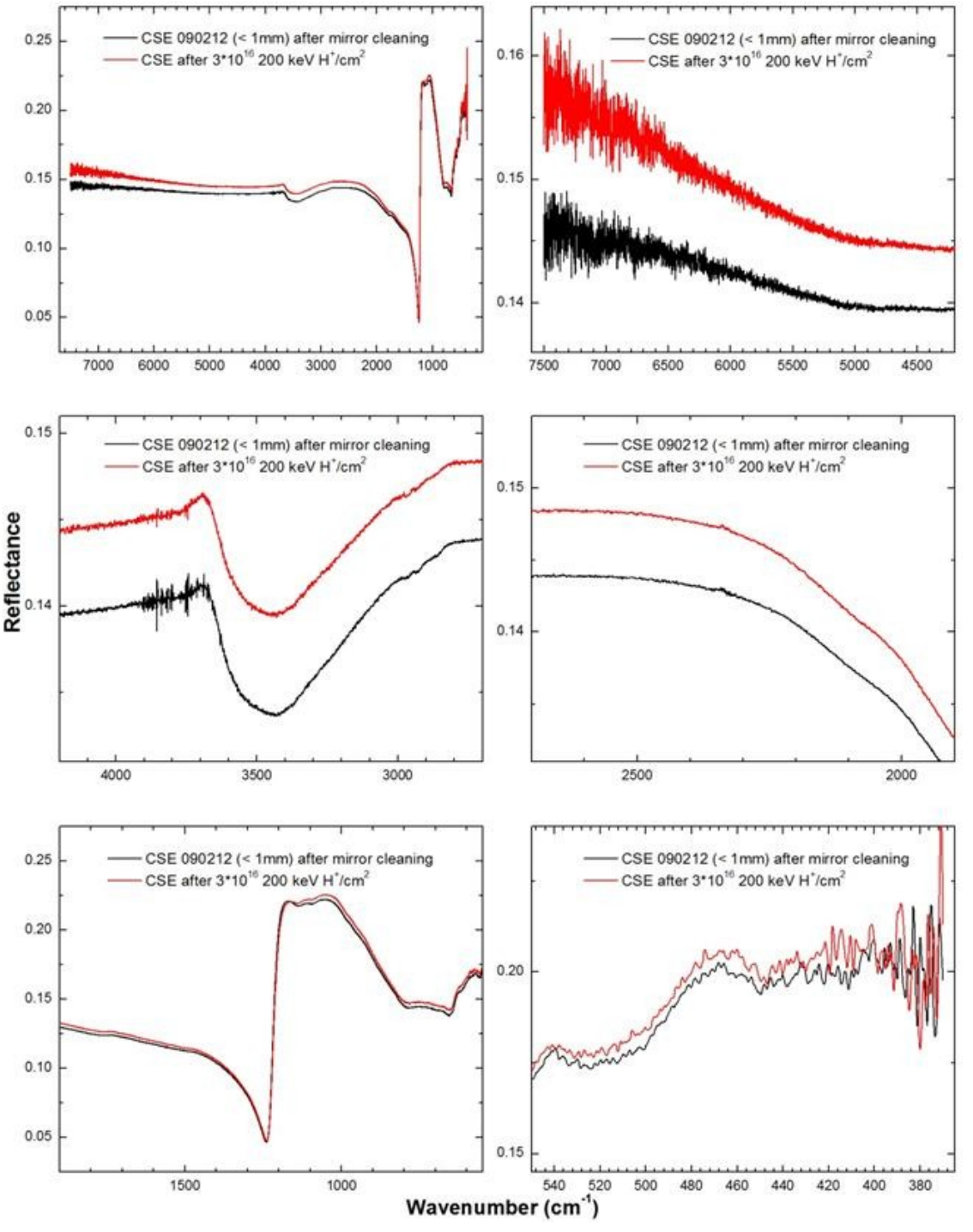


*Fig. 3.13– Reflectance spectrum of the CSE sample irradiated with $3\times10^{16}$ 200 keV $H^+/cm^2$. This irradiated spectrum is compared with that of the unirradiated sample.*

# 3.4 Other silicate spectra

## 3.4.1 Silicate films on silicon wafers

With the aim to extend this thesis work to a wider sample of Mercury analog materials another group of silicates has been studied, as outlined in Chapter 2 (§2.3.2), thanks to the courtesy of John Brucato, researcher at INAF-Osservatorio Astrofisico di Arcetri (Firenze), who prepared them.

The UV-Vis-NIR reflectance spectra of these silicon wafers coated with silicate films of different thickness, are presented in Fig. 3.14.

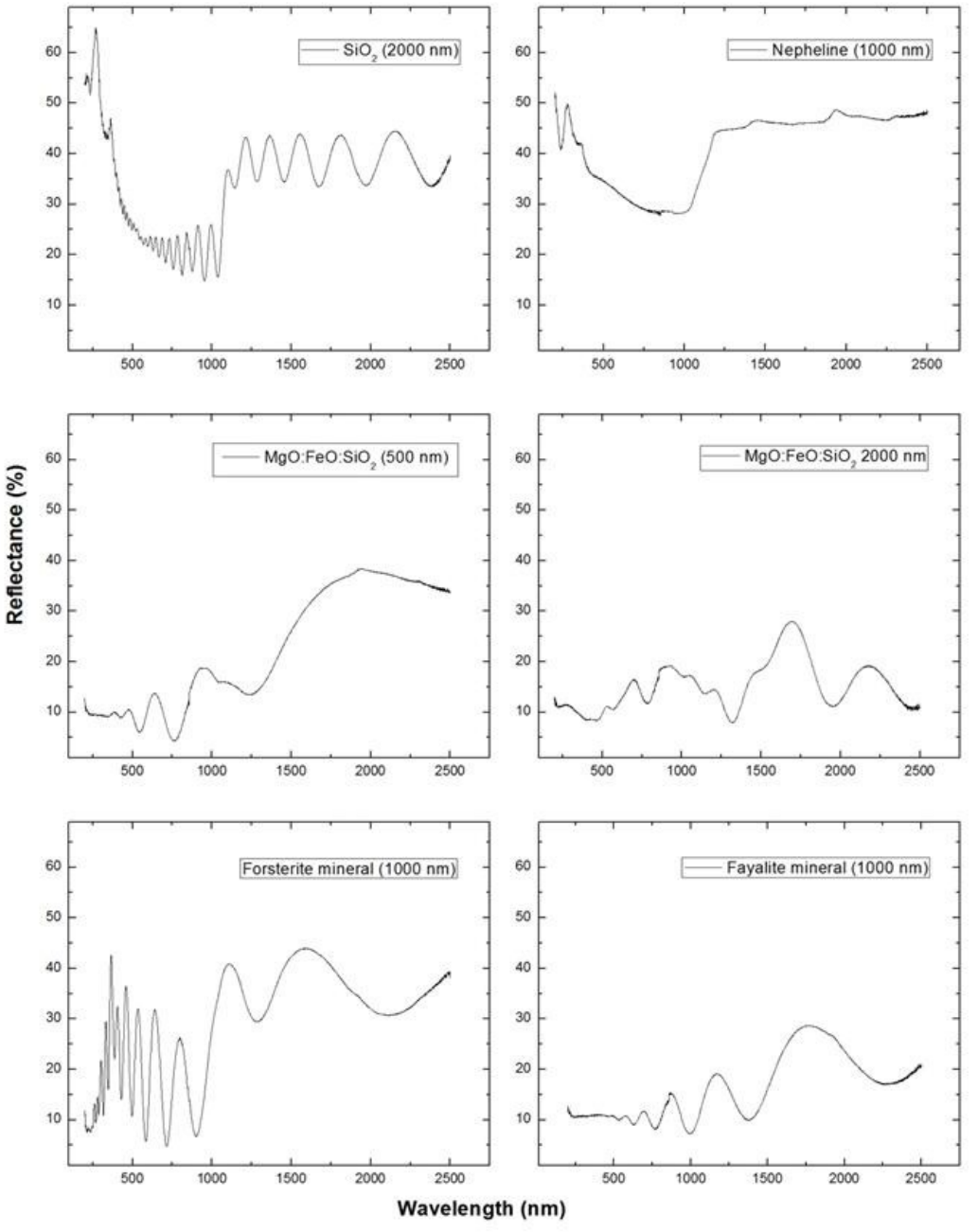


*Fig. 3.14– UV-Vis-NIR reflectance spectra of the silicon wafers coated with silicate films of different thickness.*

The IR reflectance spectra of these samples are presented in Fig. 3.15.

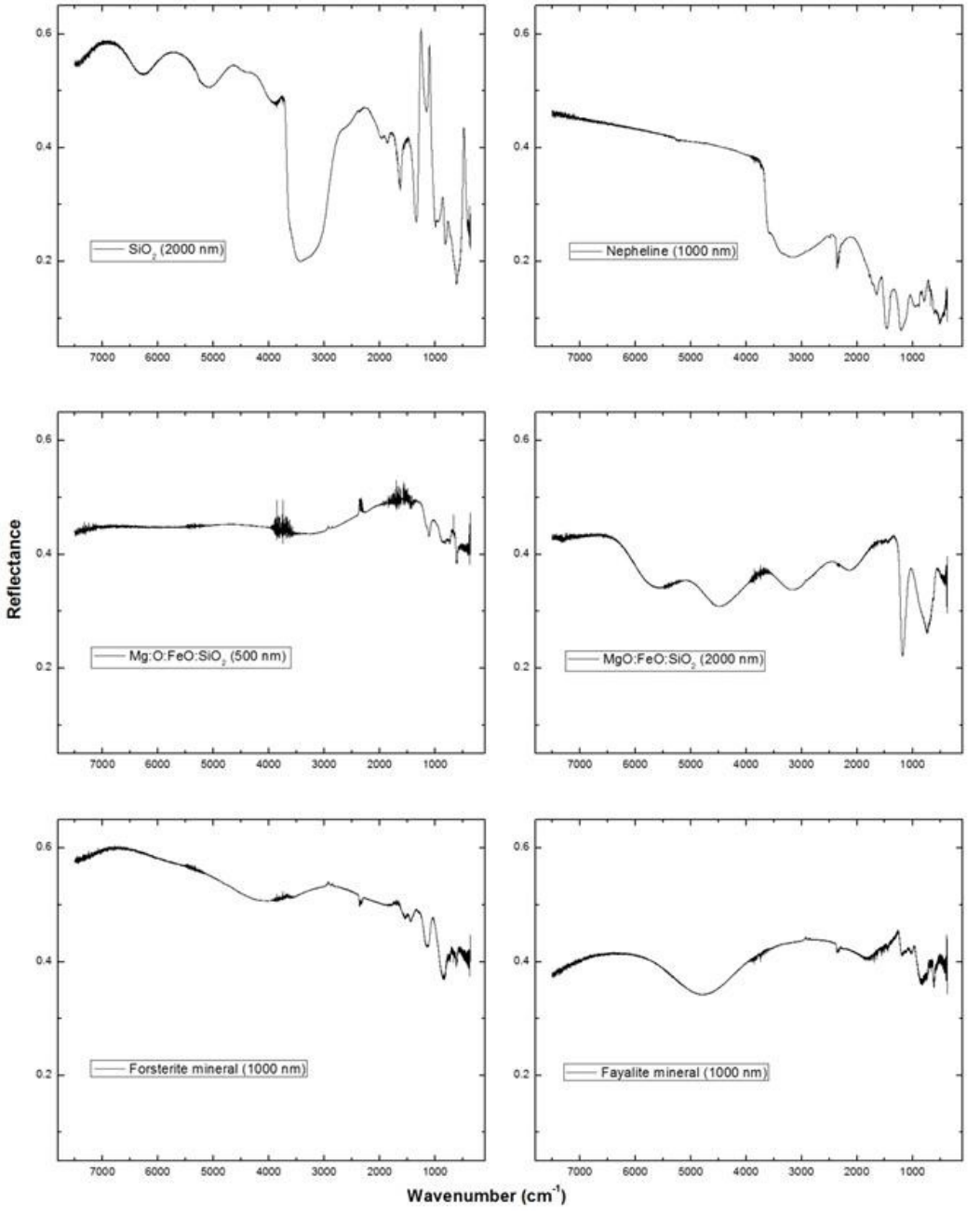


*Fig. 3.15–IR reflectance spectra of the silicon wafers coated with silicate films of different thickness.*

It can be noticed in Fig. 3.14 that almost all the UV-Vis-NIR spectra show interference fringes due to the different optical path of the radiation reflected from the interfaces air-sample and sample-substrate.
The spectra of Nepheline sample and that of the mixture MgO:FeO:$SiO_2$ (2000 nm) don't present these fringes.
Because of their spectral characteristics, unfortunately, these samples were rejected from our studies and another group of silicates has been considered and compared with the others. This analysis is presented in the next section.

## 3.4.2 Silicate rocks spectra

The spectra of silicate rocks listed in Table 2.3 are here reported in Fig. 3.16.
Some differences can be highlighted in Fig. 3.16 between the spectra of the unirradiated and irradiated samples.
In particular, for all the three samples the reflectivity decreases after irradiation in the UV-Vis spectral region, lightly increases in the 800-1600 nm range for the Sodalite sample only (and, probably, for the Jadeite sample up to 1300-1400 nm), and from 1600-2500 nm is approximately constant after irradiation or a bit lower for Nepheline and Jadeite samples.
Figure 3.17 shows the spectra, normalized at 300 nm before and after irradiation, in the spectral region < 300 nm.

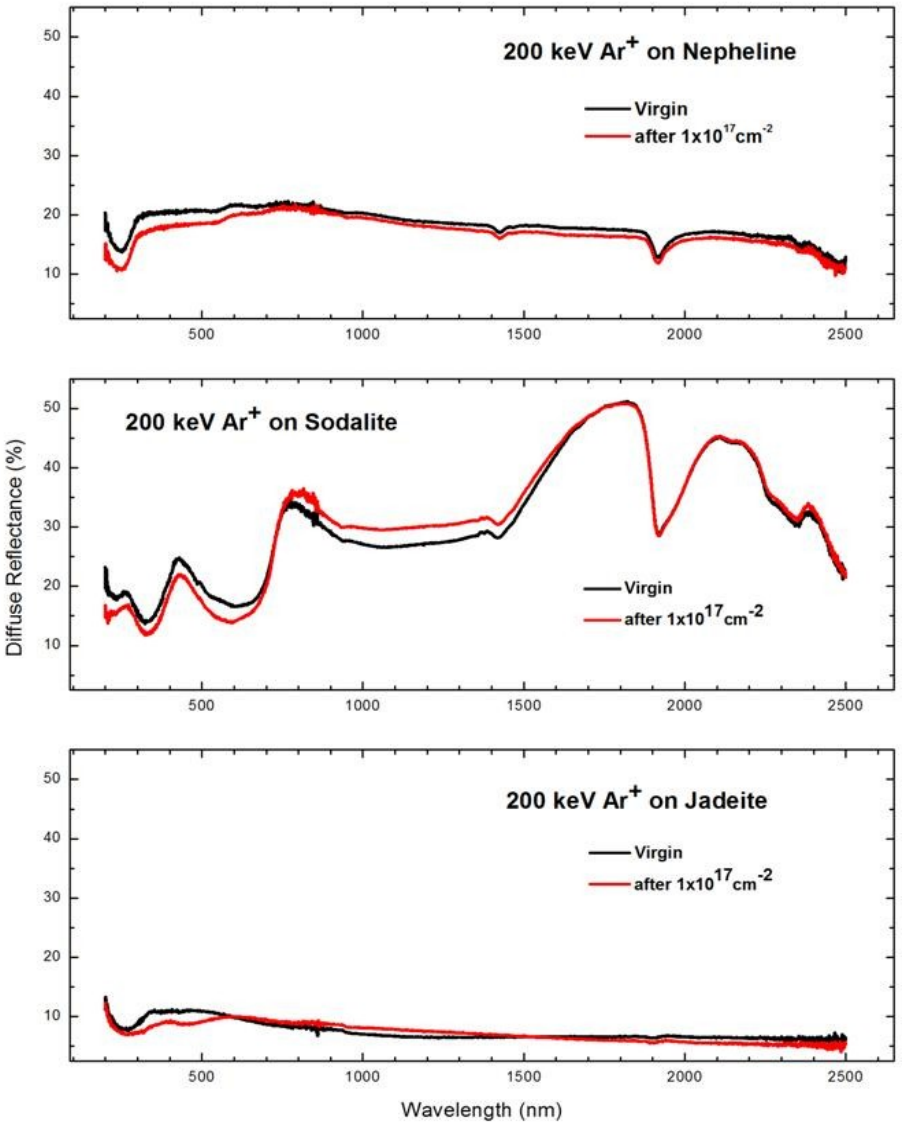


*Fig. 3.16–UV-Vis-NIR diffuse reflectance spectra of three silicate rocks. The comparison between unirradiated and irradiated samples is shown.*

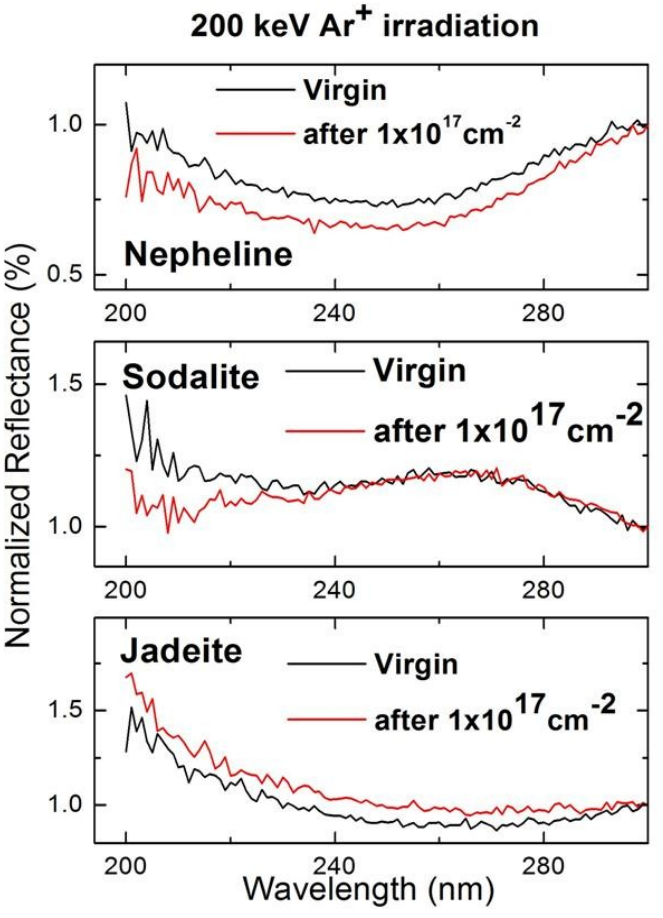


*Fig. 3.17–Normalized (at 300 nm) reflectance spectra of the three silicate rocks. The comparison between unirradiated and irradiated samples is shown.*

The zooming made in Fig. 3.17 has an important significance for Mercury's surface. In fact, in the spectral region below 300 nm, the observed spectrum is mainly due to the reflected solar light and the contribution of the emission from the "hot" Mercury is negligible.

In the next chapter the UV-Vis-NIR spectra of Mercury will be presented and compared with those of Mercury analog materials acquired in our laboratory.

# CHAPTER 4

# OBSERVATIONS AND COMPARISON WITH LABORATORY SPECTRA

The most important step for our work is to understand if the rocks used as samples can be an analogous of those present on Mercury surface. This analysis is obtained by means of a qualitative and quantitative comparison between the observed and laboratory spectra, and an opportune extrapolation to the astrophysical context and time scales. A possible compatibility has been discussed.

## 4.1 Mercury spectra

MESSENGER spacecraft has acquired a large sample of color images of different areas on Mercury surface with its Mercury Dual Imaging System (MDIS) Wide–Angle Camera, and broadly distributed higher-resolution spectra with the spectrometer MASCS.
Spectral slope, relative reflectance and morphology distinguish 3 major terrain types (Denevi et al., 2009):

*Smooth plains, Intermediate terrain (IT), Low reflectance material (LRM).*

- Smooth plains, covering about 40% of the surface and globally distributed, are probably of volcanic origin or also impact melt or basin ejecta origin and can be as thick as 5 km; they have a lower density of impact craters an fill low-lying areas such as impact craters and basins. Their reflectance and spectral slope vary from unit to unit and are distinguished in:
- High Reflectance Red Plains (HRP), have reflectance up to 20% above the global mean, relatively steep spectral slopes, sharp color and morphologic boundaries with surrounding terrains.
- Intermediate Plains (IP), have reflectance similar to the global mean and sharp morphologic boundaries with surrounding terrain.
- Low Reflectance Blue Plains (LBP), have reflectance 15% below the global mean and spectral properties intermediate to IP and LRM.

A decrease in spectral slope of ~3% is also observed from HRP to LBP.

Intermediate terrain (IT) evidences higher crater density than smooth plains and generally corresponds to regions mapped as heavily cratered terrain and intercrater plains from Mariner 10 images. Its reflectance and color properties are similar to the global mean.

Low reflectance material (LRM) covers at least 15% of the surface as thin superficial deposit and is exhibited as some form of ejecta by at least 65 craters and basins greater than 20 km in diameter. This implies depths of origin of the LRM from several kilometers to as much as 25 km, obtained through impact excavation, and subsequent distribution across the surface as ejecta veneer. It has been shown a heterogeneous distribution of its source material throughout the crust, reflectance as low as 30% below the global mean and spectral slope ~ 5% lower than HRP. Its spectral properties show little change whether they are freshly exposed in crater ray deposits or have been long exposed to the space weathering. LRM occurs as broad regions with diffuse margin as well as concentrated "centers" comprised of craters or basin ejecta and in some places LRM ejecta constitute a thin surface coating on HRP or IP, masking the color properties of the plain.

Earth based reflectance spectra confirmed by MESSENGER show no 1 μm absorption band, implying a low (<6% weight) FeO content of silicate minerals.

The global view of Mercury indicates that widespread resurfacing probably obscured early events in the planet's geological history.

A sketch for the different kinds of Mercury terrain showing a general low reflectivity, the reddening and a sort of "bump" around 800 nm is presented in Fig. 4.1.

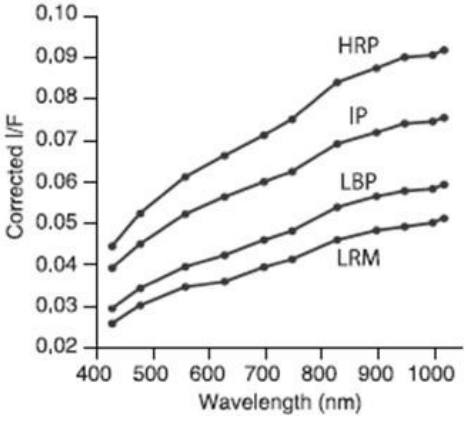


*Fig. 4.1 – (from Denevi et al., 2009)- MDIS spectra of the three type examples of smooth plains and the LRM (see text). I/F, radiance factor or reflectance, is observed radiance divided by the expected radiance from a normally solar-illuminated Lambertian surface.*

To better understand how the above mentioned terrain type are distributed, a geological map of Mercury is presented in Fig. 4.2.

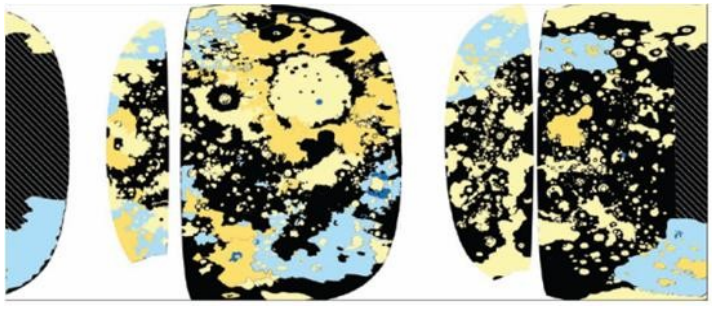

*Fig. 4.2 – (from Denevi et al., 2009)- A simple cylindrical view of Mercury (over ± 75° latitude, 0° to 360° E longitude) showing geological map of Mercury from MESSENGER and Mariner 10 mosaics. Light yellow, HRP and IP; dark yellow, LBP; light blue, regional LRM; dark blue, LRM center; black, other (fresh crater ejecta or IT); and white, no data. Crosshatches indicate areas not mapped because of high Sun illumination.*

Vernazza et al. (2010) obtained Mercury's NIR spectral measurements, from 0.9 to 2.4 μm, using the 3-m NASA Infrared Telescope Facility (IRTF) located on Mauna Kea (Hawaii), on February 28 and 29, March 22 and 23 and May 14 and 15, 2008.

Because spectra are remarkably similar, they suggested an overall compositional homogeneity (in contrast with Sprague et al., 2009; Warell et al., 2006) and confirmed the presence of the 1.1 μm feature that had been previously detected by Warell et al. (2006) and attributed to a Ca-rich clinopyroxene.

These findings are presented in Fig. 4.3.

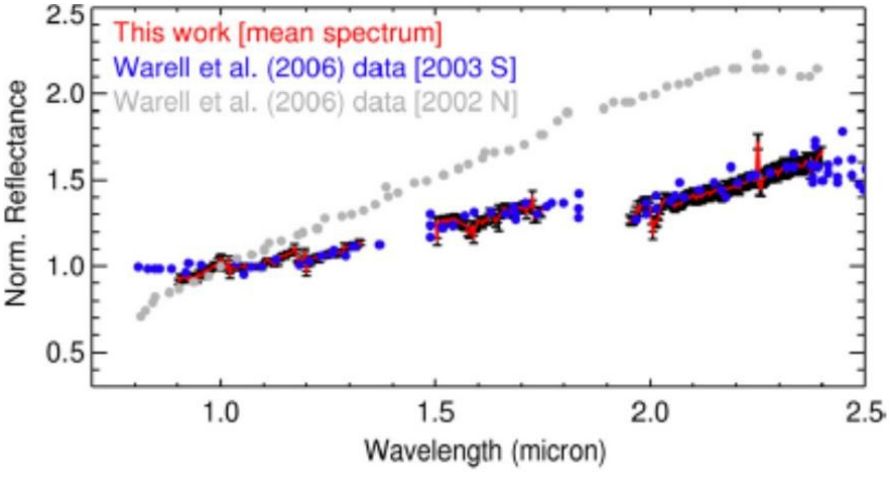


*Fig. 4.3 – (from Vernazza et al., 2010)- Ground based observations- Mean spectrum of a scan (140°-220°, longitude; ± 90, latitude) of the Mercury surface obtained by the 3-m NASA Infrared Telescope Facility (IRTF), Mauna Kea (Hawaii) on February 29, 2008 normalized to unity at 1 μm and compared with the Mercury spectra obtained by Warell et al., (2006).*

In Fig. 4.3 the authors highlight that the features around 2 μm are due to an incomplete removal of the atmospheric water vapor absorptions when dividing by the spectrum of a comparison star. The gaps around 1.4 μm and 1.9 μm are due to atmospheric water vapor absorptions that the division by the star spectrum could not correct.

Ernst et al. (2010) analyzed MDIS reflectance spectra of color units seen on Mercury, that are represented in Fig. 4.4.

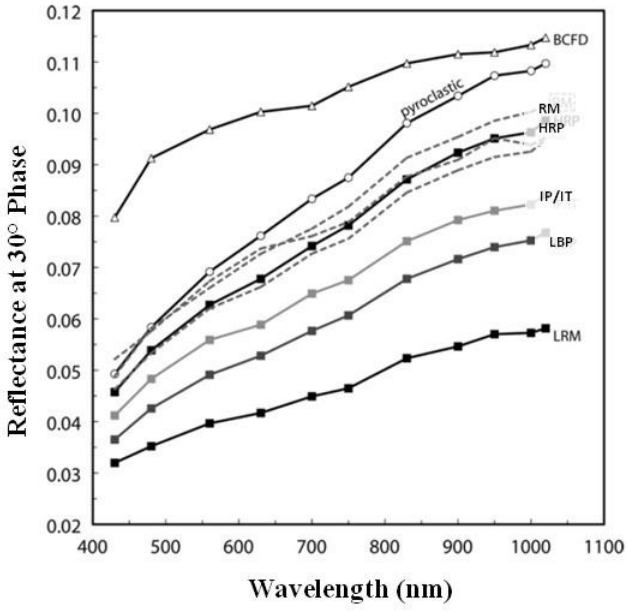


*Fig. 4.4 – (from Ernst et al., 2010)- MDIS reflectance spectra of color units seen on Mercury which have been corrected to 30°, 0°, 30° incidence, emission, and phase angle, respectively.*

The color units seen in Fig. 4.4, except for the bright crater-floor deposits (BCFDs), can be considered as parts of a compositional continuum, with LRM and RM (red material) representing the known spectral end-member. Also these spectra show a sort of "bump" around 800 nm.

Another very interesting study has been made by Blewett et. al. (2013) and is presented in Fig. 4.5.

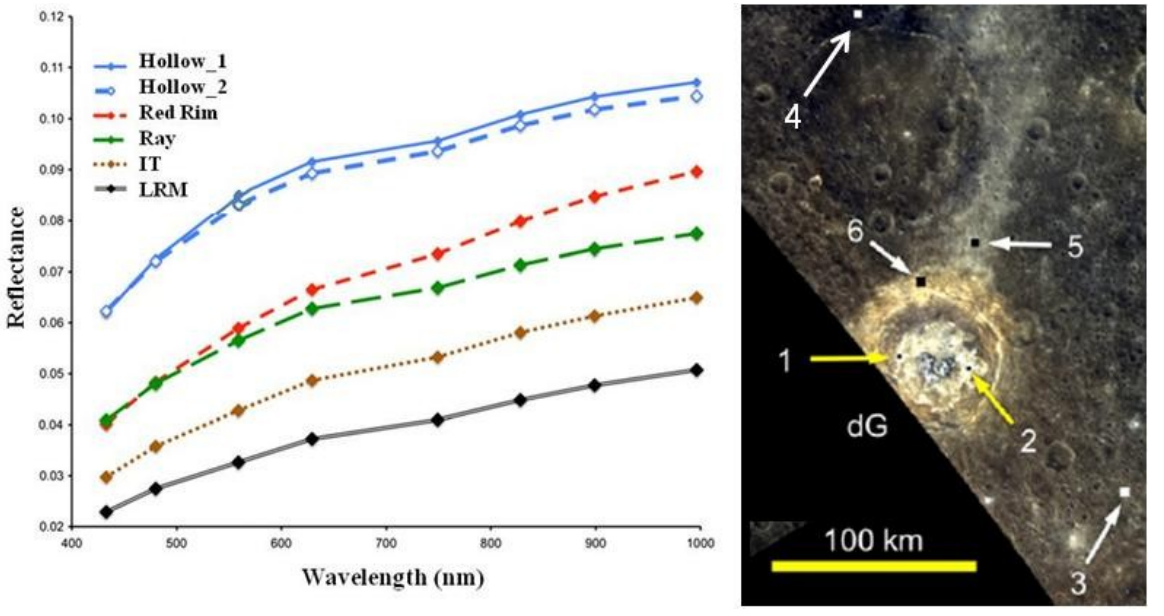


*Fig. 4.5 – (from Blewett et al., 2013) (Left panel): Reflectance MDIS eight-color spectra for surfaces in and around de Graft (dG) crater. Locations from which the spectra were extracted are shown in the right panel: 1 – hollows location 1. 2 – hollows location 2. 3 – intermediate terrain (IT). 4 – low-reflectance material (LRM). 5 – ray. 6 – red rim.*

In Fig. 4.5 the reflectance data of the above indicated terrain types in Mercury, can be associated with the locations from which the spectra have been extracted. Mercury's hollows are unusual features that apparently have no counterpart in silicate material on other Solar System bodies. Global mapping of hollows shows that they occur in dark materials for which reflectance is lower than the planetary average (LRM or LBP) and have not been found in high reflectance smooth plains. Their (relatively) high reflectance and characteristic blue color could be a consequence of the destruction of the darkening agent, of compositional differences related to altered minerals or vapor deposits, or of a physical state (grain size, texture, porosity, and/or scattering properties) that differs from that of impact-generated regolith elsewhere on the planet (Blewett et al., 2013).

Once again the spectra present a red slope and do not evidence any absorption feature. The small dip in the spectra at 749 nm can be caused by residual calibration errors or issues with the photometric normalization.

Blewett et al. (2013) also compared the above indicated spectra with other spectra of terrestrial and lunar soil, as shown in Fig. 4.6.

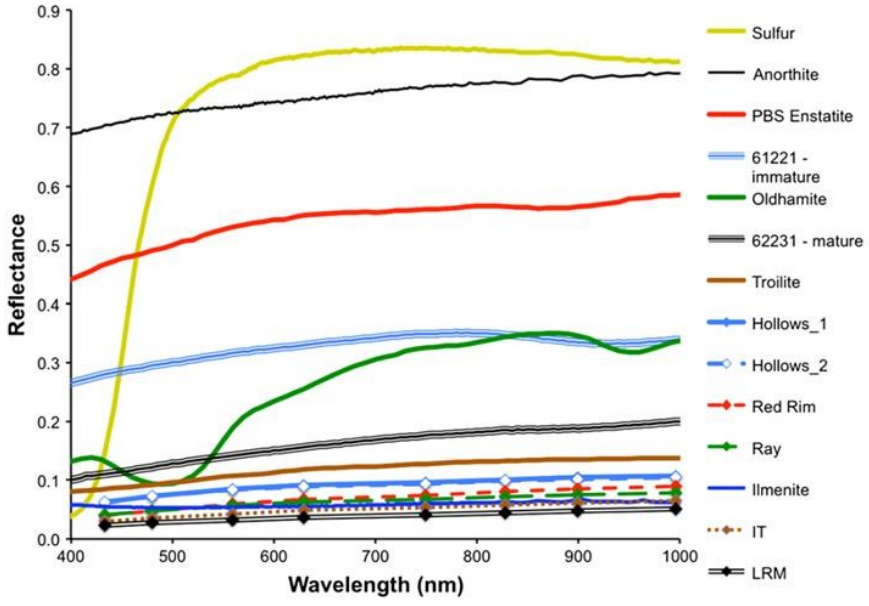


*Fig. 4.6 – (from Blewett et al., 2013)- Laboratory reflectance spectra for Mercury analog minerals and two lunar soils, together with the Mercury spectra from Figure 4.5 (left panel).*

These authors found that troilite (FeS) and ilmenite ($Fe_2TiO_3$) can have appropriate characteristics to be associated to Mercury surface, being relatively dark and red, also if the upper limit of about 4% Fe and 0.8 wt % Ti in Mercury surface places a strong constraint on the average amount of these minerals.

Oldhamite (CaS) has two absorption features, at 500 and 950 nm, and is too bright to be used as Mercury analog material.

Nevertheless there is experimental evidence that heating the samples to Mercury daytime temperatures causes a decrease of the band intensity and of the spectral slope (Helbert et al., 2012).

A final significant consideration has to be made about bright radar signals coming from Mercury poles.

According to Boynton et al. (2007), ground-based observations of Mercury discovered regions of highly coherent backscattered radar signals from deposits in the floors of impact craters near Mercury's north and south poles (see Fig. 4.7). These were similar to the radar

backscatter signature from water ice at the Martian south pole and on the Galilean satellites of Jupiter.

Because also the floors of craters at the highest latitudes on Mercury are in permanent shadow, water ice is a good candidate for polar deposit material. Ice could be in ejecta, released during volcanic emissions and quickly covered by regolith gardening at polar regions, or it could have been delivered by the impacts of comets or volatile-rich asteroids, or formed by surface chemical interactions driven by solar wind proton implantation on the surface, followed by poleward migration. Thermal models and Monte Carlo models of volatile distribution and storage in permanently shadowed regions have also shown that water ice could be stable for several million years following deposition. A recent comet impact delivering water vapor to Mercury could satisfy the lifetime requirement.

Sprague et al. (1995) argued that sulfur may be the backscattering material on grounds that it is not as volatile as $H_2O$ ice and that it should be abundant in infalling and vaporizing micrometeoroids and may be sputtered from minerals such as *sphalerite* ((Zn,Fe)S) in the surface regolith. XRS spectrometer has observed up to 4 wt. % sulfur on Mercury's surface (Nittler et al., 2011).

Starukhina (2001) argued that cold, low-iron and low-Ti silicates could also produce the observed radar characteristics.

In Fig. 4.7 the images of the above mentioned radar signals found in the North and South poles are presented.

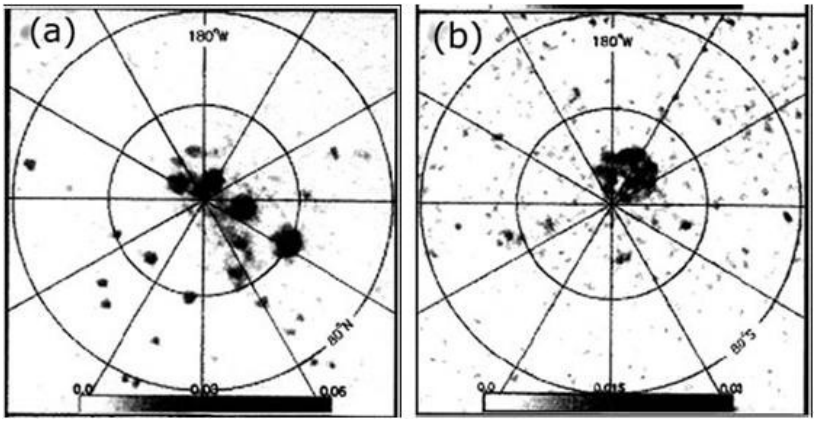


*Fig. 4.7– (from Boynton et al., 2007)- Regions of high coherent radar backscatter and strong depolarization (dark areas in images) from the (a) North and (b) South polar regions of Mercury.*

Vilas et al. (2012) examined albedo and color differences observed in the MDIS images in different terrain types and ages and confirmed earlier findings that there are no major absorption features in most reflectance spectra of Mercury surface. Nevertheless, they identified subtle absorption features of varying spectral width and placement in reflectance spectra of high-albedo material, correlated with what appear to be younger features presumably not yet fully affected by space weathering. These generally divide into two categories: a feature centered near ~600 nm similar to the absorption features observed in laboratory spectra of sulfides (Helbert et al., 2012) and a feature centered at a longer wavelength (~900 nm).

In Figure 4.8 the reflectance data of a Mercury crater are expressed as I/F, where I is light reflected from Mercury surface and F is incident sunlight. It seems clear the presence of two absorption features around 600 and 900 nm.

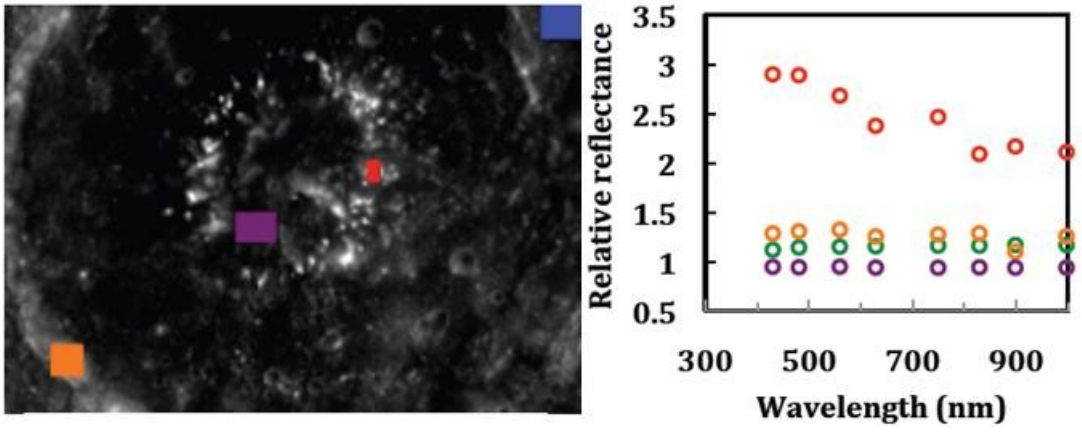


*Fig. 4.8– (from Vilas et al., 2012)- Ratios of I/F photometry at Atget crater (100 km diameter) on Mercury (left panel). Points in the right panel are ratios of I/F photometry for four areas of varying albedo (keyed by color to the left panel, except for green points located off the image area displayed) to the dark blue area, all from the same color suite. The Atget material lacks absorption features except for the bright peak-ring material (red), which shows a potential feature centered near 600 nm.*

Summarizing, MDIS images and UV-Vis-NIR spectra from MASCS (see Figures 1.9 and 1.10) show that Mercury's major color units all share red-sloped reflectance spectra. Color variations among units are products of changes in the steepness of the spectral slope (430 to 1020 nm): steeper slope is termed relatively *red*, shallower slope is termed relatively *blue*

(Denevi et al., 2009). Furthermore all surface materials on Mercury display relatively low albedo and featureless spectra (no obvious absorption bands) (Ernst et al., 2010), except what was observed by Vilas et al. (2012) at the Atget crater, and a sort of "bump" around 800 nm (likely due to uncertainties in the calibration).

In the next section the importance of sulfides for Mercury surface and their spectral characteristics will be examined in detail.

# 4.2 Sulfides

MESSENGER observations at Mercury confirmed that bright and spectrally blue deposits within large craters are marked by irregular depressions (hollows) associated with impact crater floors, central peaks, and wall terraces (Helbert et al., 2012).

The question about the nature of the deposits in which the hollows form is still subject of actual investigation.

Blewett et al. (2011) and Vaughan et al. (2012) proposed sulfides as a possible candidate.

Spectral reflectance measurements of sulfides, in the wavelength ranges spanned by MDIS and MASCS, are limited to only a few samples (for example *oldhamite*- (Ca, Mg)S- in Burbine et al. 2002), and in the literature there are no measurements of sulfides that have been exposed to Mercury's high dayside temperatures.

Helbert et al. (2012) presented spectral reflectance measurements at visible and near-infrared wavelengths of fresh and heated synthetic samples of manganese sulfide (MnS), calcium sulfide (CaS), and magnesium sulfide (MgS), as well as elemental sulfur (S). They inferred that sulfides display a diagnostic feature at about 0.6 μm, and found this result consistent with the few available spectra in the literature (Burbine et al. 2002).

Starting from a consideration in industrial steel production, Helbert et al. (2012) observed how MgS and CaS are formed once Mg- or Ca-bearing materials are introduced into the molten ore and bind with the sulfur in the ore. Being MgS and CaS less dense than the molten steel, they float and are removed from the top. Following this model the authors proposed a mechanisms for the formation of the hollows in Mercury's surface.

When the ascending high-Mg lava encounters a sulfur-rich deposit in the subsurface, Mg and Ca would react with the sulfur, forming sulfides. The slag deposit is then partially

removed by space weathering and thermal desorption and the compounds destroyed by photo- or ion-dissociation, as can be seen in Fig. 4.9.

Reflectance spectra of elemental sulfur, MgS, and MnS under ambient conditions are shown in Fig. 4.10.

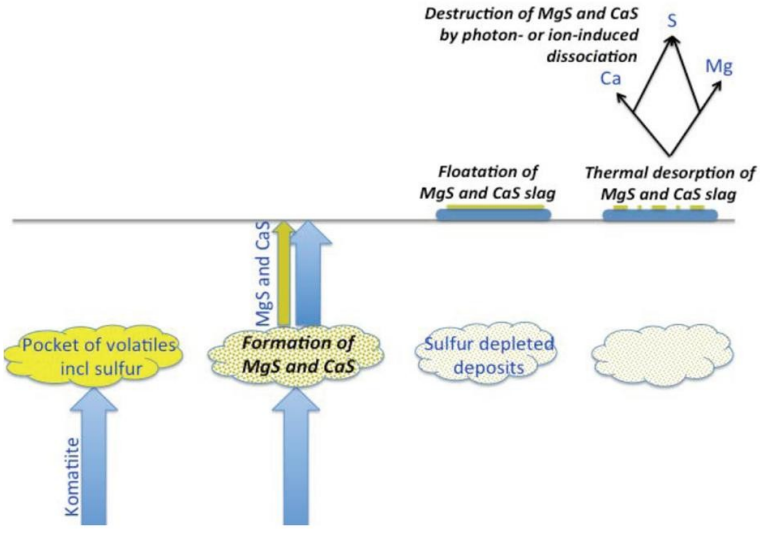


*Fig. 4.9– (from Helbert et al., 2012)- Schematic of the slag scenario with komatiite as an example of a Mg-rich lava.*

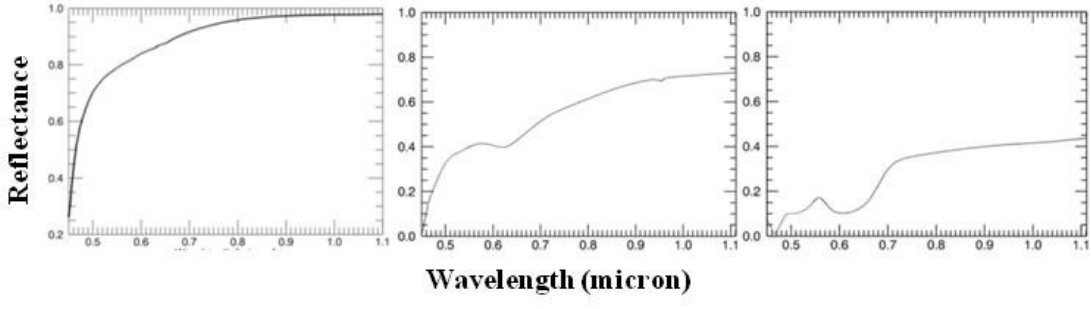


*Fig. 4.10– (from Helbert et al., 2012)- Left: Biconical reflectance spectrum of sulfur (0-25 μm grain size). The spectrum was obtained at a biconical geometry with incidence and emission angles of 15°. Middle: Reflectance spectrum of MgS (0-25 μm grain size) obtained under the same configuration as the sulfur. Right: Reflectance spectrum of MnS (0-25 μm grain size) obtained in the same configuration as the sulfur.*

It can be highlighted that the sulfur is much brighter under the same geometry. This difference might support the idea that decomposition of sulfides could lead to a temporary increase of surface brightness.

Geophysical studies evidenced how $H_2S$ and $SO_2$ dominates the volcanic sulfur budget in the gas phase (Clarisse et al., 2011; Mc Gee et al., 2001). Volatiles, as sulfides, emitted from nonerupting magma bodies encounter superimposed hydrothermal envelopes. If there is substantial mixing of magmatic and hydrothermal fluids ($4SO_2+4H_2O \rightarrow 3H_2SO_4+H_2S$), S species condense generating convecting acid-sulfate-chloride fluids with extreme low pH, which dissolve silicate components of the volcanic edifice, increasing porosity and permeability, and precipitate *sulfates* (salts of sulfuric acid ($H_2SO_4$) as anhydrite ($CaSO_4$), alunite ($KAl_3(SO_4)_2(OH)_6$), gypsum ($CaSO_4 \cdot 2H_2O$), *sulfides* (anions of sulfur in their lowest oxidation state ($S^{2-}$), like pyrite ($FeS_2$), pyrrhotite ($Fe_{(1-x)}S$(x = 0 to 0.2)) and native S in the voids created (Oppenheimer, 1996).

On the other hand chemical models of solar nebula chemistry show the influence of progressive water depletion from the inner nebula, being solar nebula the gaseous cloud from which the Sun and planets formed by condensation. Under canonical solar nebula conditions, $H_2S$ is the dominant S-bearing species in the gas phase and *troilite* (FeS) is the primary reservoir for S after condensation. As water vapor diffuses out to its condensation front, SiS becomes the most abundant S-bearing gas and MgS and CaS compete with FeS as the main sulfide reservoir (Pasek et al., 2005).

On the basis of the above mentioned results it is plausible that the presence of sulfides on Mercury is due to sulfur species condensation occurred during its several episodes of volcanism .

In this thesis an experiment on a presumable sulfides-rich volcanic sample has been performed. The sample was a fresh erupted etnean sample (09/02/2012) and soon after collected in the Crater of South East (CSE, which is also the sample name) and analyzed. No feature around 600 nm (attributable to sulfides absorption in Helbert et al., 2012) was found (as can be seen in Fig. 3.6). We explain this result with the high volatility of the sulfur that in addition was not abundant in this specimen. CSE sample was also irradiated with 200 keV $H^+$ and, although some differences in the reflectance values are obtained in the IR spectral region (as shown in Fig. 3.13), the reflectance values do not undergo a significant change.

# 4.3 Comparison between observational and laboratory spectra

As known from the literature, and as it has been shown in section 4.1, Mercury's reflectivity is quite low and, furthermore, observations have been mostly acquired in the spectral region between 400 and 1000 nm.

For this reason we decided to select and compare, with Mercury's spectra, our laboratory spectra which exhibit the lowest reflectivity, that are those with the smallest original grain size.

The chosen laboratory spectra are presented in Fig. 4.11.

In this figure it is also plotted the CSE (<1 mm) spectrum, because this sample constitutes the youngest rock specimen collected and could give complementary information.

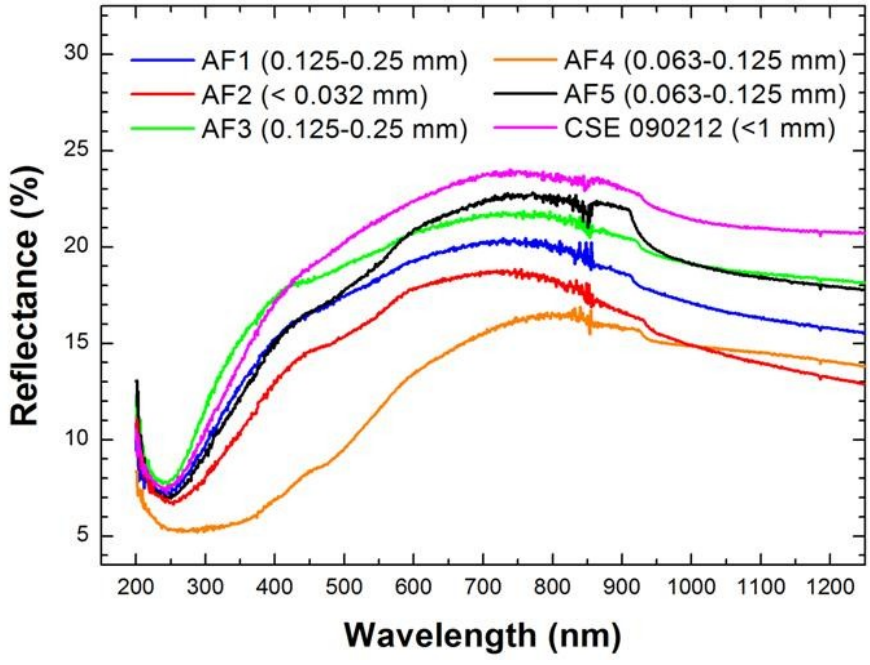


*Fig. 4.11 – A selection of etnean sample spectra (zoomed in the 200-1300 spectral region).*

In particular, a comparison among observational MESSENGER data (from Blewett et al., 2013) and our laboratory spectra, in the above mentioned spectral region, is presented in Fig. 4.12.

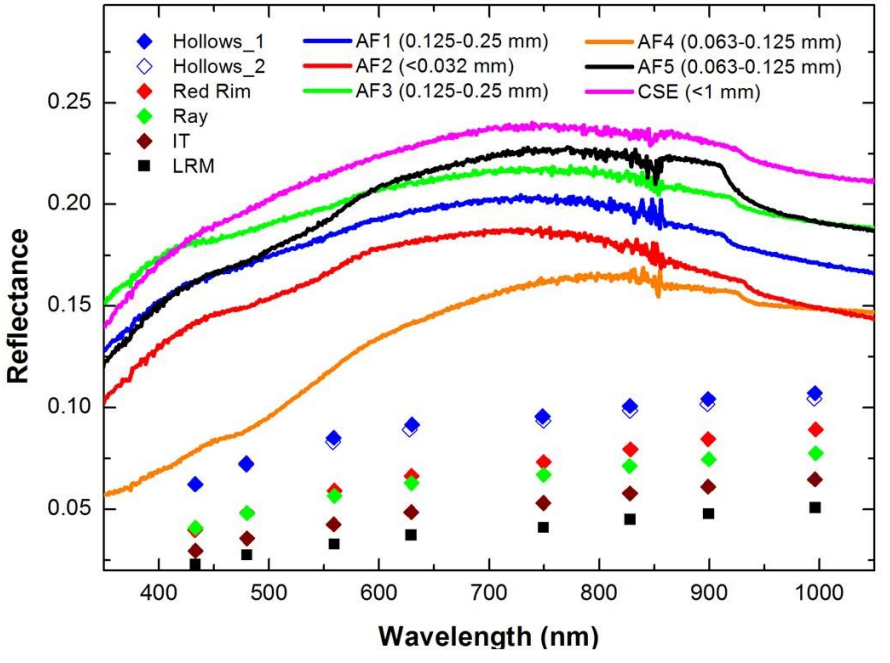


*Fig. 4.12 – A comparison among MESSENGER data, presented in Blewett et al. (2013), and the spectra of our smallest etnean samples acquired in laboratory in the 350-1050 nm spectral region.*

It can be clearly observed in Fig. 4.12 that the reflectance of our laboratory samples is nearly three/four times higher than that of the observed surfaces. Furthermore, at wavelength higher than 750 nm the reflectance of our samples tends to decrease, while those of Mercury surface exhibit a general reddening, also if it undergoes to a small dip at 749 nm, likely due to residual calibration errors or issues with the photometric normalization (Blewett et al., 2013).

The reflectance of AF4 is the nearest to those observed, especially in the UV-Vis spectral region.

We have also compared the observed spectra with those obtained, for the AF1 sample, after ion bombardment.

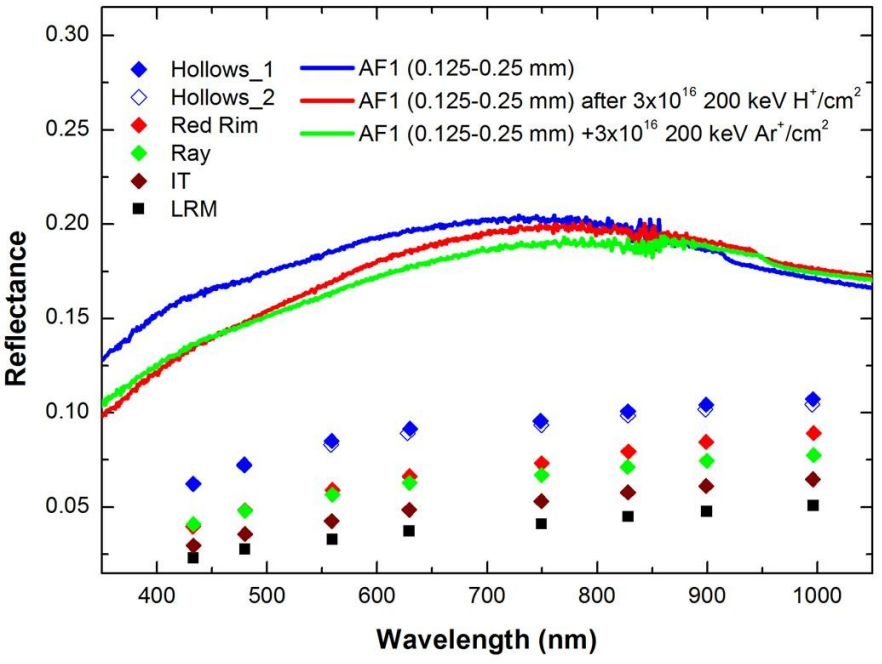


*Fig. 4.13 – A comparison among MESSENGER data presented in Blewett et al. (2013) and the spectra of AF1 laboratory sample before and after irradiation with $3\times10^{16}$ 200 keV $H^+/cm^2+3\times10^{16}$ 200 keV $Ar^+/cm^2$.*

Figure 4.13 shows that irradiation decreases the reflectance of the irradiated sample, especially in the UV-Vis spectral region, but the differences are not so significant to reproduce what is observed.

A comparison among the observational data from Blewett et al. (2013) and the silicate sample's spectra described in Chapter 2, is reported in Fig. 4.14.

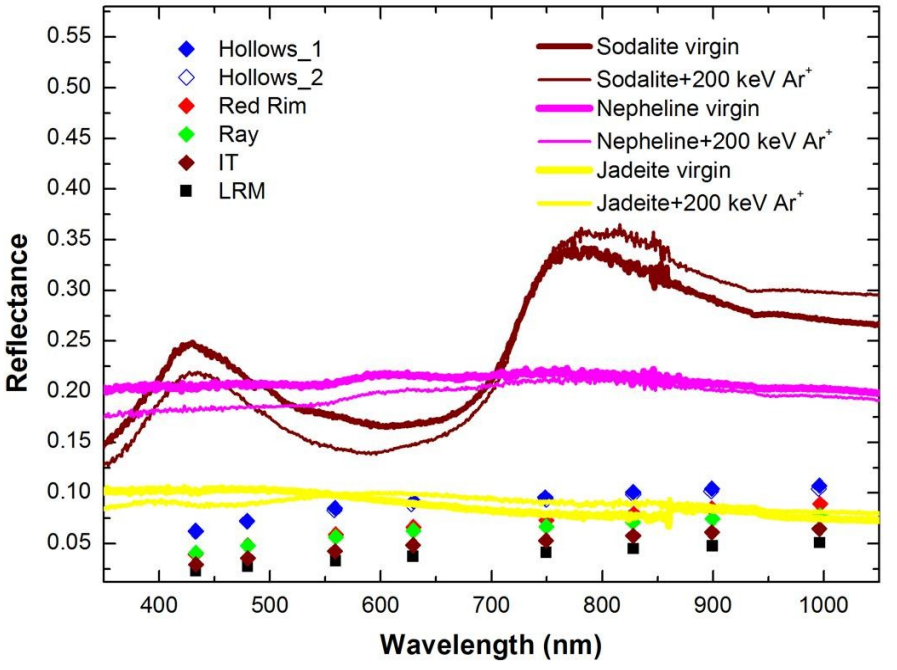


*Fig. 4.14 – A comparison among the MESSENGER data presented in Blewett et al. (2013) and the spectra of the silicate laboratory samples before and after irradiation with $1\times10^{17}$ 200 keV $Ar^{+}/cm^{2}$.*

From Fig. 4.14 we can note that also in this case, irradiation causes a small decrease of the reflectance values in the UV-Vis spectral region.

A special emphasis has to be given to the spectrum of jadeite, whose reflectivity (before and after irradiation) overlaps that of different zones on Mercury surface in the Vis-NIR spectral region, even if the slope present some differences.

To better understand the differences/similarity between mercurian and laboratory samples we calculated the slopes of some of the two sets of spectra. We chose two specific spectral ranges (430-630 nm and 630-750 nm) because they better describe the slope variations.

The chosen spectra are shown in Fig 4.15.

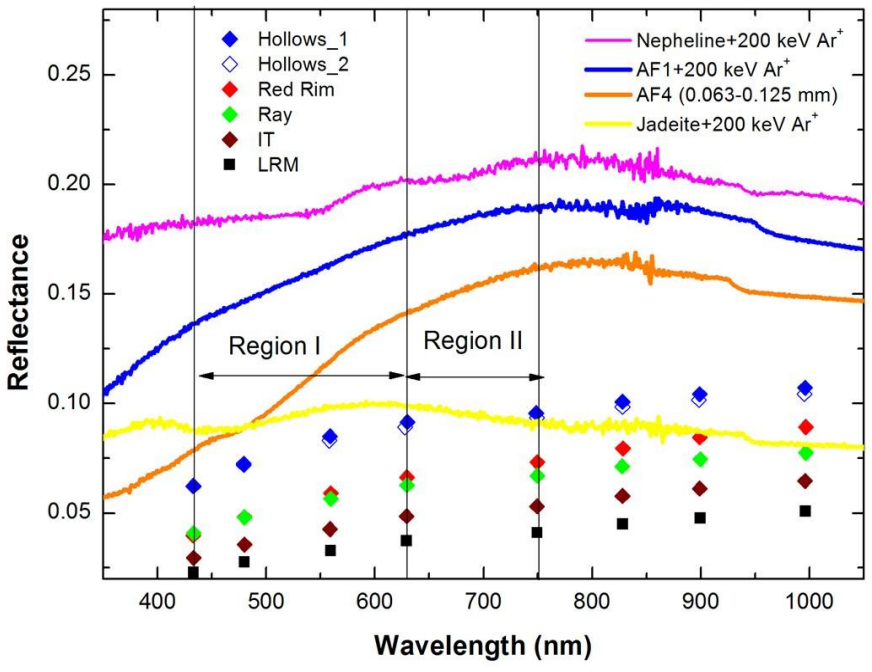


*Fig. 4.15 – A comparison among the MESSENGER data presented in Blewett et al. (2013), the spectra of the silicate laboratory samples (after irradiation with $1x10^{17}$ 200 keV $Ar^{+}/cm^{2}$), the AF sample with the lowest reflectivity (AF4) and the AF sample irradiated with $3x10^{16}$ 200 keV $H^{+}/cm^{2}$+$3x10^{16}$ 200 keV $Ar^{+}/cm^{2}$ (AF1). The spectral regions in which the slopes have been calculated are evidenced by two vertical lines.*

Slopes are calculated by the ratio of the difference between the reflectance in the aforementioned ranges, and the wavelength range itself, as shown in the equations 4.1 and 4.2. The results are presented in Tables 4.1, 4.2, 4.3 and sketched in Figures 4.16, 4.17 and 4.18.

$$Slope\ I = \frac{Refl\,(630) - Refl\,(430)}{200} \qquad (Eq\ 4.1)$$

$$Slope\ II = \frac{Refl\,(750) - Refl\,(630)}{120} \qquad (Eq\ 4.2)$$

*Table 4.1– Slope calculations for the reflectance spectra of the different Mercury locations explored by MESSENGER, as described in Blewett et al. (2013).*

| | *Slopes ($nm^{-1}$)* | | | | | |
|---|---|---|---|---|---|---|
| *Spectral range (nm)* | *Hollows 1* | *Hollows 2* | *IT* | *LRM* | *Ray* | *Red Rim* |
| *430-630* | *1.47E-4* | *1.35E-4* | *9.51E-5* | *7.16E-5* | *1.109E-4* | *1.33E-4* |
| *630-750* | *3.36E-5* | *3.59E-5* | *3.71E-5* | *3.12E-5* | *3.47E-5* | *5.8E-5* |

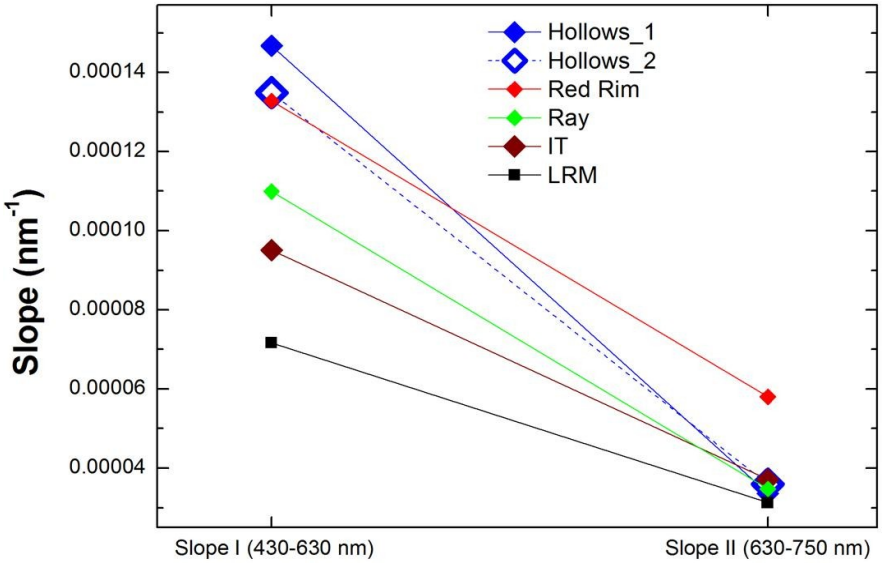


*Fig. 4.16 – A sketch of the calculated slopes indicated in Table 4.1. The size of the symbols has only a graphic purpose.*

Table 4.1 and Fig. 4.16 evidence that slopes are always higher in region I with respect to region II. In particular, in region I, the slope increases when the reflectivity of the surfaces increases (see Fig. 4.5 and the comparisons shown in Figures 4.12 and the following) while, in region II, all of the slopes but that of Red rim are similar. Furthermore all of the slopes in region II are nearly one order of magnitude lower than those in region I.

In Table 4.2 the slopes calculated for our AF1 specimen are reported. Slopes of other AF samples spectra with small grain size are also included.

*Table 4.2– Slope calculations for the reflectance spectra of some AF laboratory samples. The AF1 sample is irradiated with $3\times10^{16}$ 200 keV $H^+/cm^2$ and then with $3\times10^{16}$ 200 keV $Ar^+/cm^2$.*

| | *Slopes ($nm^{-1}$)* | | | | | | |
|---|---|---|---|---|---|---|---|
| *Spectral range (nm)* | *AF1 (0.125-0.25 mm)* | *AF1 + 200 keV $H^+$* | *AF1 +200 keV $Ar^+$* | *AF1 (0.032-0.063 mm)* | *AF3 (0.125-0.25 mm)* | *AF4 (0.063-0.125 mm)* | *CSE 090212 (<1 mm)* |
| *430-630* | *1.80E-4* | *2.63E-4* | *2.14E-4* | *2.65E-4* | *1.44E-4* | *3.23E-4* | *2.20E-4* |
| *630-750* | *5.48E-5* | *1E-4* | *9.28E-5* | *6.27E-5* | *5.77E-5* | *1.73E-4* | *9.40E-5* |

As already seen for the observations, also the slopes of our samples present higher values in region I with respect to region II, and comparing the slopes of AF1 (0.125-0.25 mm) with AF1 (0.032-0.063 mm) unirradiated samples it is seen that the sample with the smallest size has the highest slope both in region I and in region II. It is also observed that it is not valid, in general, the slope trend followed by the observational ones that increases with increasing the reflectivity. Furthermore, after the first irradiation, the AF1 slope increases (in both regions I and II) and then decreases with the second one, maintaining always higher values than that of the unirradiated sample.

Finally all the slopes calculated for our AF samples have, on average, values greater than those of the Mercury surface presented in Table 4.1.

A comparison among the most significant AF slopes and those of the six different Mercury locations is presented in Fig. 4.17.

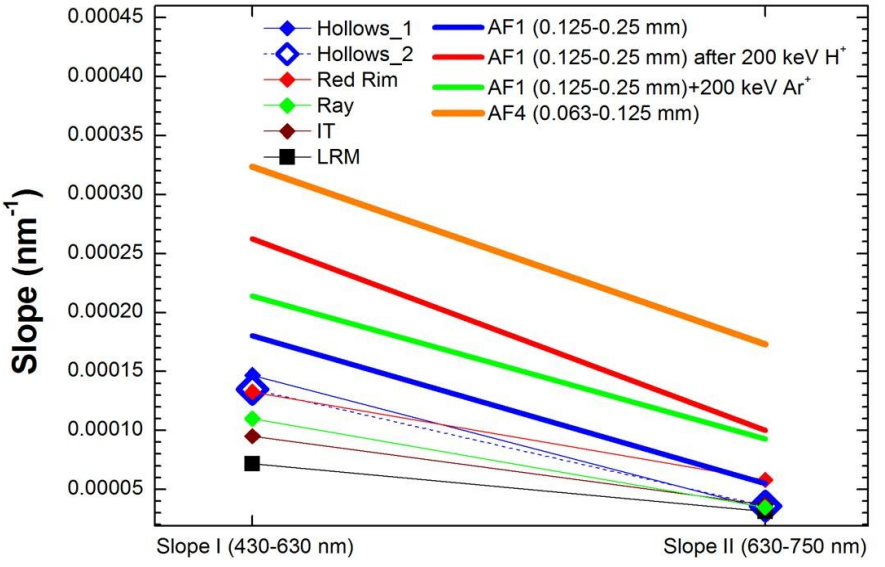


*Fig. 4.17 – A representative comparison among the calculated slopes of Mercury surfaces indicated in Table 4.1, and those of our samples indicated in Table 4.2. The size of the symbols has only a graphic purpose.*

The slopes of the silicate samples (described in Chapter 2, §2.3.2) are reported in Table 4.3.

*Table 4.3– Slope calculations for the reflectance spectra of the silicate laboratory samples. The slopes for unirradiated and irradiated with $1\times10^{17}$ 200 keV $Ar^+/cm^2$ samples are presented.*

| | *Slopes ($nm^{-1}$)* | | | | | |
|---|---|---|---|---|---|---|
| *Spectral range (nm)* | *Sodalite* | | *Nepheline* | | *Jadeite* | |
| | *Not irr.* | *+200 keV $Ar^+$* | *Not irr.* | *+200 keV $Ar^+$* | *Not irr.* | *+200 keV $Ar^+$* |
| *430-630* | *-4.05E-4* | *-3.43E-4* | *4.96E-5* | *1.02E-4* | *-6.78E-5* | *5.90E-5* |
| *630-750* | *0.001* | *0.001* | *3.44E-5* | *7.72E-5* | *-8.98275E-5* | *-6.78E-5* |

Also in this cases slope values in region I are higher with respect to those in region II, and this is valid also for the irradiated samples (except for sodalite sample). Slope values of irradiated samples are, however, higher with respect to the unirradiated ones.

Slopes of the samples with the lowest reflectivity are again the lowest in regions I and II and after irradiation, except for that of sodalite in region I.

Compared with observational ones in Table 4.1, the slopes of these silicate samples are mostly lower, except for sodalite in region II.

This comparison is better clarified in Fig. 4.18, in which AF4 slopes are excluded (because of their distance with the observations) and AF1 slopes are included.

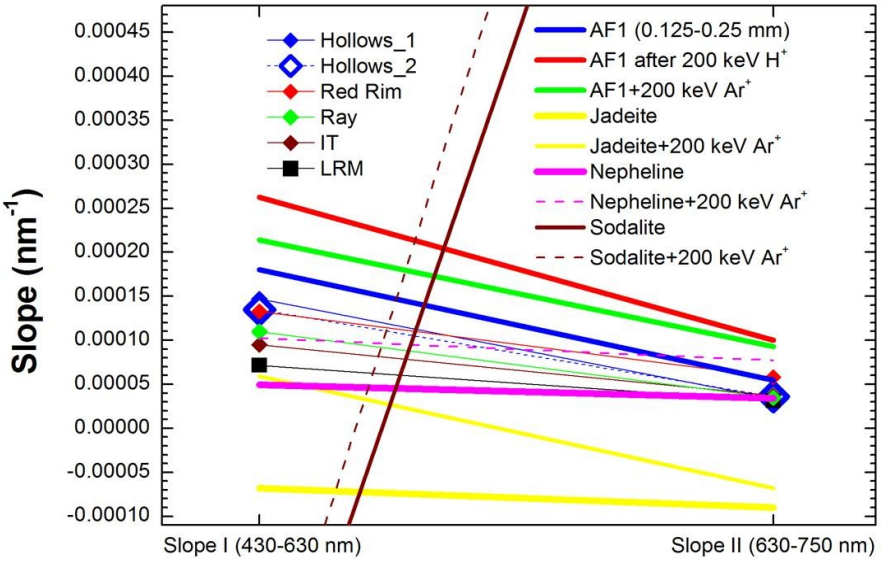


*Fig. 4.18 – A representative comparison among the calculated slopes of Mercury surfaces indicated in Table 4.1, and those of our samples indicated in Tables 4.2 and 4.3. The size of the symbols has only a graphic purpose.*

Fig. 4.18 evidences clearly that the trend of sodalite slope is completely different from that of the others.

# 4.4 Discussion

The observations so far acquired by the two missions addressed to Mercury (Mariner 10 and MESSENGER) have given (and are still giving) an enormous amount of data, together with

a fundamental contribution to the advance of the research for this little, not well known, planet.

BepiColombo mission will add new complementary information and new experiments are then requested, also for testing its instruments.

In this work several silicate samples have been studied with the aim to be characterized and used as Mercury analog materials in preparation to ELENA (Emitted Low-Energy Neutral Atoms) experiments, one of the instruments which will fly on board BepiColombo.

The choice of our candidate Mercury analog materials has been based on the existing data in the literature, deriving from observations and modeling. Laboratory spectra, acquired before and after irradiation, allow us to observe the changes in the spectral reflectance of materials, mimic the surfaces of airless solar system bodies bombarded by different ions. For this reason laboratory spectra have been compared with the observational ones, looking for any possible analogy.

According to the results obtained in this work it can be deduced that our samples, in the Vis-NIR spectral region, are mostly brighter than Mercury locations so far investigated. In particular, comparing the reflectance of our samples with that of the laboratory samples presented in Blewett et al. (2013) and shown in Fig. 4.6, the great part of our data is positioned in a lower-values region that is intermediate between the reflectance of mature (i.e. more space weathered) lunar soil and that of the immature one (in order of increasing reflectivity), and that is nearly two times the reflectivity of the highest observational value of Mercury.

Nevertheless our silicate sample jadeite exhibits a reflectivity that presents values as low as Hollows1 in the Vis region and as low as Red rim and Rays in the NIR. These values could be compared, except for the slope, to that of the troilite sample (FeS) presented in Blewett et al. (2013) work, as opaque-phase material.

In the UV spectral region the reflectance of all our samples presents values ranging from about 0.05-0.2, as shown in Fig. 4.11 and in Fig. 3.16, and a significant decrease after irradiation.

The 200-300 nm is a spectral range particularly relevant to Mercury because the spectrum we observe is mainly due to the reflection of the solar radiation, and the contribution of the emission from the “hot” Mercury is negligible.

In addition slopes calculated in region I (430-630 nm) and in region II (630-750 nm) for laboratory and observational data are all comparable. Specifically it is observed that AF samples have, on average, values greater than those of Mercury, while silicate samples present slope values that are mostly lower.

Concerning irradiation it is important to note that the ion energy and fluences have to be scaled in order to estimate the correspondent exposure time scale at Mercury.

The fluences used in laboratory ($3\times10^{16}$ and $1\times10^{17}$ ions $cm^{-2}$) correspond to an exposure of the surface of Mercury to the solar wind of $10^3$-$10^5$ years (Baratta et al., 2011).

The results here presented point out that space weathering of the Mercury surface could produce relevant spectral variations of the surface reflectance. These effects should be considered when modeling the surface mineral composition from the spectral reflectivity.

Concluding, we can say that the samples utilized, although they do not match the observed spectra, are however among the best candidates studied so far as Mercury's spectra analogues. A wider spectral study of candidate Mercury analog materials is necessary, before and after irradiation and at different temperatures.

Specimen of etnean soils can however be considered as a template of magma on the surface of Mercury because they present featureless spectra in the investigated spectral region.

Nepheline, jadeite and sodalite, which contains Na and K, can be considered as template to investigate the origin of Na and K in the exosphere of Mercury.

# BIBLIOGRAPHY


- Blewett, D.T., Vaughan, W. M., Xiao, Z., et al. 2013, Journal of Geophysical Research Planets, Vol 118, 1013.
- Blewett D. T., Chabot, N. L., Denevi, B. W. et al. 2011, Science, 333, 1856-1859.
- Baratta, G., Kanuchova, Z., Palumbo, M. E., Sangiorgio, I., Strazzulla, G. 2011 EPSC-DPS, Vol. 6, Preview.
- Boynton, W. V., Sprague, A., L., Solomon, S. C., et al. 2007, Space Sci Rev 131, 85.
- Brunetto, R. & Strazzulla, G. 2005, Icarus, 179, 265.
- Buemi, A., Cimino, G. and Strazzulla, G. 1998, Journal of Geophysical Research, Vol. 103 No. E6, page 13667.
- Burbine, T. H., et al. 2002 MPS, 37, 1233.
- Burger, M. H., Killen, R. M., Vervack, Jr. R. J. et al. 2010, EPSC, Vol. 5, 373.
- Carli, C., Sgavetti, M., Pompilio, L. and Trua, T. Lunar and planetary Science XXXIX (2008), N.1564.
- Clarisse, L., Coheur, P. F., Chefdeville, S. et al. 2011, Geophysical Research Letters, Vol. 38, L10804.
- Clark, R. N. 1979, Icarus 40, 94.
- Denevi, B. W., Robinson, M. S. ,Solomon, S. C., Science 2009. 324, 613.
- D'Amore, M., Helbert, J., Maturilli, A. et al. 42° LPSC (2011), N. 1381.
- Domingue, D. L., Murchie, S. L., 41° LPSC (2010), N.2455.
- Dukes C. A., Chang, W., Famà et al- Icarus 2011: 212, 463.
- Ernst, C. M., Murchie, S. L., a, Barnouin, O. S., et al. 2010, Icarus 209, 210.

- Fogel, R. A. 2005, LPS, N. 2395.
- Greenhagen, B. T. and Paige D. A. Lunar and Planetary Science XXXVII (2006), N. 2406.
- Helbert, J., Moroz, L. V., Maturilli, A. et al. 2007, Advances in Space Research, Vol. 40, Issue 2, Page 272.
- Helbert J., Maturilli, A., D'Amore, M. et al., 43rd Lunar and Planetary Science Conference (2012), N. 1381.
- Holsclaw, G.M., McClintock, W. E., Domingue, D.L. et al. 2010, Icarus 209, 179-194.
- Lucey, P. G., and Riner, M. A. 2011, Icarus 212, 451.
- Malavergne, V., Brunet, F., Righter, K. et al., 43rd Lunar and Planetary Science Conference (2012), N. 1860.
- Mc Clintock, W. E., Izenberg, N. R., Holsclaw, G. M. et al. 2008., Science, 321, 62.
- McGee K., A., Doukas, M. P. and Gerlach, T. M. 2001, Geophysical Research Letters, Vol. 28, No. 23, page 4479.
- Milillo, A., Wurz, P., Orsini, S. et al. 2005, Space Science Reviews, 117, 397.
- Moroz, L. V., Maturilli, A., Helbert, J. et al. 2007 Lunar and Planetary Science XXXVIII, N. 1741.
- Nittler L. R., Starr, R. D., Weider, S. Z., et al. 2011, Science 333, 1847.
- Oppenheimer, C. 1996 Geophysical Research Letters, Vol. 23, No. 16, page 2057.
- Orlando, T. M., Sprague, A. L., Grieves, G. A. et al., 41st LPSC (2010), N. 2246.
- Orsini, S., Livi, S., Torkar, K. et al. 2010, Planetary and Space Science, 58, 166.
- Pasek, M., A., Milsom, J., A., Ciesla, F. J.; et al. 2005, Icarus, Vol. 175, Issue 1, 1.
- Scollo, S., Baratta, G. A., Palumbo, M. E., Corradini, S., Leto, G and G. Strazzulla 2013, JOURNAL OF GEOPHYSICAL RESEARCH: ATMOSPHERES, VOL. 118, in press.
- Sprague, A.L,. Hunten, D.M,. Lodders, K 1995, Icarus 118, 211.
- Sprague, A. L., Donaldson Hanna, K. L., Kozlowsky, R. W. H. et al. 2009, Planet. Space Sci., 57, 364.
- Sprague, A. L., Vervack, R. J. , Killen, R. M. et al. 2010, DPS meeting, 42, Bulletin of the American Astronomical Society, Vol. 42, p.985.
- Starukhina, L.V., 2001, J. Geophys. Res. 106, 14701.

- Strazzulla, G., Baratta, G. A., & Palumbo, M. E. 2001, Spectrochimica Acta, Part A, 57, 825.
- Strazzulla, G., Dotto, E., Binzel, R. et al. 2005, Icarus 174, 31.
- Vaughan W. M., Helbert, J., Blewett, D. T. et al., 43rd LPSC (2012), N. 1187.
- Vernazza, P., DeMeo, F., Nedelcu, D. A: et al., 2010, Icarus, 209,125.
- Vervack R. J., Jr., et al (2010) Science, 329, 672.
- Vilas, F., Sprague, A. L., Izenberg, N. R. et al., LPS XXXIX (2008), N. 1212.
- Vilas, F., Domingue, D. L., Sprague, A. L. et al., 43rd LPSC (2012), N.1330.
- Warell, J. 2003, Icarus, 161, Issue 2, page 199.
- Warell, J., Sprague, A. L., Emery, J. P. et al. 2006, Icarus, Vol.180, Issue 2, page 281.
- Wurz, P., Whitby, J.A., Rohner, U. et al. 2010, Planetary and Space Science, 58, Issue 12, 1599-1616.
- Yamada, M., Sasaki, S., Fujiwara, A. et al. 1999, Lunar and Planetary Science XXX, 1566.
- http://messenger.jhuapl.edu/orbit_insertion/WorkingAtMercury.html
- http://sci.esa.int/science-e/www/area/index.cfm?fareaid=30
- http://www.ifsi-roma.inaf.it/serena/index.php?categoryid=1
- http://www.rssd.esa.int/index.php?project=BEPICOLOMBO&page=index
- http://www.nasa.gov/mission_pages/messenger/main/index.html
- Extract of BepiColombo section ESA's Report to the 37th COSPAR meeting, Montreal, Canada, July 2008.
- SRIM 2003, www.srim.org

# ACKNOWLEDGEMENTS

La tesi fin qui presentata non si può ancora considerare conclusa senza citare quanti, in vario modo, hanno contribuito insieme a me, alla sua realizzazione.

Proverò, con brevi righe, ad esprimere tutta la mia sincera gratitudine.

A Francesca Zuccarello, la Professoressa e mia Tutor, va il primo ringraziamento. Alla sua cordialità e comprensione devo la possibilità di attuare e completare questo lavoro.

Ad Umberto Lombardo, presente Coordinatore dei primi due anni, un grazie per la simpatia e per gli stimoli forniti attraverso l'organizzazione di frequenti seminari di (anche troppo!) alto livello.

Al prof. Romano, per aver coordinato quest'ultimo anno con dedizione ed affabilità.

A tutto il Gruppo del *Laboratorio di Astrofisica Sperimentale*, all'interno del quale ho avuto l'onore di lavorare (anche solo come *grano di polvere*), e che mi ha sostenuto fino alla fine, rivolgo la più genuina riconoscenza.

Elisabetta, mia Supervisor, occupa un posto privilegiato. È grazie all'entusiasmo trasmesso e all'accoglienza mostrata (sin dai tempi della tesi di laurea) che ho intrapreso questo percorso di studio e ricerca. Il preciso ed attento insegnamento, l'infaticabile e cordiale disponibilità (in accordo spesso con i miei tempi, notoriamente *lunghi*..), la pazienza, insieme alle preziose e puntuali correzioni hanno favorito la mia crescita scientifica e personale. Le usuali ed amichevoli conversazioni ed i consigli hanno poi reso più piacevole l'impegnativo lavoro quotidiano.

A Giuseppe, il "mago". Alla gentilezza nelle ricchissime (e ripetute!) spiegazioni, alla rapidità nel rimediare ai *danni* da me causati, all'accuratezza e dedizione

insegnate attraverso l'esecuzione ed interpretazione delle svariate prove di laboratorio. Grazie di cuore.

A Gianni, alla enorme esperienza e statura scientifica, generosamente spese a favore di questa ricerca. A lui, un sentito riconoscimento. Agli importanti sproni ed all'esempio fornito attraverso la *PET* (Passione-Entusiasmo-Tenacia) *Therapy*, somministrata anche via e-mail durante le innumerevoli trasferte in tutto il mondo.

A Franco, per il supporto tecnico a me dato in laboratorio, sin dal mio ingresso, e per il basilare contributo che la sua competenza e devozione ha, da sempre dato (e dà ancora!) al LASp.

Ai nuovi collaboratori tecnici, Vincenzo Greco, per la discrezione e cortesia, e Saro Di Benedetto, per il tocco di allegria.

A John Brucato (INAF-Osservatorio Astrofisico di Arcetri) e a Rosanna Corsaro (INGV, Catania) per aver fornito materiali e campioni utili a questa ricerca.

A Zuzana, grazie per la sua amicizia e per la preparazione, spesso messa a mia disposizione con generosità.

A Farah, per i momenti spensierati trascorsi e per il supporto nella lingua inglese.

A tutti i ragazzi con i quali ho condiviso la stanza, insieme a qualche pranzo e, soprattutto, quotidiane esperienze, fatiche, risate e crescita lavorativa ed umana. Grazie a Claudia per l'affidabile amicizia; a Sergio (dirimpettaio indisciplinato!) per il buonumore e la sincerità; a Cosimo (mio *nipote*) per la maturità frammista a sicula *liscìa*; ad Agata per le innumerevoli e pronte consulenze e per i gradevoli incontri; ad Adriano per la gentilezza ed abilità (in tutto!); a Ricardo per i frequenti "soccorsi informatici" e per il raro garbo.

E ancora ad Elisa B. ed Elisa D. S., a Gaetano, Matteo, Antonio, Maddalena, Orazio, Giuseppe, per i momenti di relax e confronto.

Grazie ai fraterni amici, ai *Signori zii*, e ai parenti che, con delicatezza ed affetto, mi stanno vicini.

Grazie a chi, con la sua solida presenza, ineguagliabile bontà e generosità mi dà forza ogni giorno e "paga le conseguenze" del mio impegno.

A Silvio e Caterina, premurosi genitori, amorevoli ed instancabili nonni, fondamentali aiuti nella stesura di questa tesi; ai miei fratelli nella carne (e a quelli acquisiti) che mi camminano sempre accanto; ad "Angelina", mamma e nonna cara, esempio di forza e smisurato dono di sé, sostegno vitale in questo lavoro; a Nicola, mio caro papà, che continua ad insegnarmi l'ottimismo, la "leggerezza" e ad

incitarmi ad essere *veloce* (!); a Giovanni, inestimabile dono, ragione di vita e motivazione finale di questo lavoro;

a Salvo, mio amato, robusto compagno di viaggio, insostituibile aiuto, quotidiana fonte di gioia e crescita.

E al Datore di tutti i doni, Colui che pota e insieme dona largamente.

Ivana Sangiorgio